

Understanding white matter pathology through correlating  
longitudinal and quantitative MRI metrics weekly in the cuprizone  
mouse model of demyelination

by

Vanessa Leanne Palmer

A Thesis submitted to the Faculty of Graduate Studies of  
The University of Manitoba  
in partial fulfillment of the requirements of the degree of

MASTER OF SCIENCE

Department of Biomedical Engineering

University of Manitoba

Winnipeg

Copyright © 2016 by Vanessa Leanne Palmer

# Abstract

Demyelinating diseases, such as multiple sclerosis (MS), degrade the myelin sheath that surrounds and protects the axons in our central nervous system. Myelin sheaths aid in the transmission of information along the axons, which transfer signals throughout the brain and spinal cord. When this sheath is disrupted, signal transfer becomes less efficient leading to some of the most disabling symptoms of MS. Magnetic resonance imaging (MRI) plays an important role in the diagnosis, management and treatment of MS because of its ability to detect lesions prior to clinical symptoms. Even with its importance, MRI has its limitations including the lack of correlation between conventional MRI results and tissue pathology which restricts clinicians from improving their understanding between MRI findings and patient disability. Inflammation, axonal damage, increased cellularity and demyelination, rarely occur in isolation in MS. Individual MRI methods are sensitive to a variety of pathologies and are generally not specific to an individual pathology. This thesis aims to improve the understanding of how microstructural tissue changes caused by a variety of pathologies influence MRI metrics by developing and applying methods in a longitudinal study using the cuprizone mouse model of MS. Several *in vivo* and *ex vivo* MRI methods were developed, compared and correlated with tissue measurements taken from electron microscopy images of control and cuprizone fed mice. MRI methods included  $T_1$  and  $T_2$  relaxometry, diffusion tensor imaging (DTI), and quantitative magnetization transfer imaging (qMTI). Correlations with tissue measurements were made at the early stages of the disease course, specifically at

weeks 2 and 3 of the 6 week cuprizone induced disease course. Through tissue analysis, a significant difference in myelinated axon fraction between groups was found at week 3 of the study. Strong Spearman correlations between tissue measurements and MRI metrics included mean diffusivity ( $\langle D \rangle$ ) vs. myelinated axon fraction ( $\rho=-0.84$ ), *ex vivo*  $T_2$  vs. myelinated axon fraction ( $\rho=-0.68$ ), and normalized  $T_2$ -weighted signal ( $T_2w$ ) vs. myelinated axon fraction ( $\rho=-0.80$ ). Multiparametric MRI studies show promise in bridging the gap between damage detected in clinical images and clinical status associated with MS.

# Acknowledgments

I would first like to thank my supervisor and friend, Dr. Melanie Martin, for her support and guidance during this great learning experience. I would also like to thank my committee members: Dr. Francis Lin, Dr. Idris Elbakri, Dr. Cyrus Shafai, and Dr. Miyoung Suh for the support and challenging questions during committee meetings and my thesis defense that pushed me to work through problems on the spot. Dr. Richard Buist, the MRI system manager, provided detailed knowledge and great instruction on using the MRI system. I thank him for all his help.

In the first weeks of data collection I didnt know how much of a headache image registration and analysis would be. I would like to express my sincerest gratitude to Sheryl Herrera who spent hours registering and analysing the first weeks of images for me so that I could submit an abstract for ISMRM in Milan, Italy as well as for all her time spent creating instructions on these methods for me and the rest of the lab members. I would also like to thank Dr. Jonathan Thiessen for always proving feedback and answering all of my analysis questions.

I would like to acknowledge the scholarship support from the Canadian Institutes of Health Research as well as the project support from Natural Science and Engineering Research Council, Canadian Foundation for Innovation, Research Manitoba, the University of Winnipeg, the University of Manitoba, and the Manitoba Research and Infrastructure

Fund.

I met my boyfriend, Kyle, just before I started my masters studies. Since the first day of classes he never failed to provide strength, humour, empathy and love that helped me get through each day.

Last but not least, thank you to my wonderful family. My parents have always been my biggest fans in both sports and more importantly, my education. I thank them for showing me and instilling the importance of education and hard work. I cant express how much their motivation and love means to me and how it has helped me to reach my goals. I hope I can continue to make you proud.

# Table of Contents

<b>Title</b>	<b>i</b>
<b>Abstract</b>	<b>ii</b>
<b>Acknowledgments</b>	<b>iv</b>
<b>Contents</b>	<b>vi</b>
<b>List of Figures</b>	<b>xi</b>
<b>List of Tables</b>	<b>xii</b>
<b>1 Introduction</b>	<b>1</b>
1.1 MRI and White Matter Changes . . . . .	2
1.2 The Cuprizone Mouse Model of Multiple Sclerosis . . . . .	4
<b>2 Theory</b>	<b>6</b>
2.1 Nuclear Magnetic Spin Systems . . . . .	6
2.1.1 Magnetic Dipole Moments in a Magnetic Field . . . . .	6
2.1.2 The RF Pulse and Resonance . . . . .	10
2.1.3 FIDs and Relaxation . . . . .	13
2.2 Magnetic Resonance Imaging (MRI) . . . . .	16

2.2.1	Signal Localization . . . . .	16
2.2.2	The Spin Echo . . . . .	21
2.3	Magnetic Resonance Imaging Methods . . . . .	22
2.3.1	T <sub>2</sub> -weighted Imaging . . . . .	23
2.3.2	Relaxometry . . . . .	24
2.3.3	Diffusion Tensor Imaging (DTI) . . . . .	25
2.3.4	Quantitative Magnetization Transfer Imaging (qMTI) . . . . .	31
<b>3</b>	<b>Methods</b>	<b>38</b>
3.1	Mouse Model . . . . .	38
3.2	<i>In vivo</i> MRI . . . . .	39
3.3	<i>Ex vivo</i> MRI . . . . .	43
3.4	Preprocessing and Image Analysis . . . . .	44
3.5	Electron Microscopy (EM) . . . . .	46
3.6	Statistical Analysis . . . . .	48
<b>4</b>	<b>Results</b>	<b>50</b>
4.1	Cuprizone Diet . . . . .	50
4.2	<i>In vivo</i> MRI . . . . .	51
4.3	<i>In vivo</i> normalized T <sub>2</sub> -weighted signal and MTR correlations . . . . .	56
4.4	<i>Ex vivo</i> MRI . . . . .	58
4.4.1	Relaxometry . . . . .	58
4.4.2	DTI . . . . .	62
4.4.3	qMTI . . . . .	70
4.5	MRI Correlations . . . . .	77
4.6	Electron Microscopy . . . . .	79
4.7	MRI and EM Correlations . . . . .	87
<b>5</b>	<b>Discussion</b>	<b>91</b>

5.1	Electron Microscopy . . . . .	92
5.2	<i>In vivo</i> MRI and EM . . . . .	93
5.2.1	Normalized T <sub>2</sub> -weighted Signal and MTR Correlations . . . . .	95
5.3	<i>Ex vivo</i> MRI and EM . . . . .	96
5.3.1	Relaxometry . . . . .	96
5.3.2	DTI . . . . .	98
5.3.3	qMTI . . . . .	100
5.4	MRI Metric Correlations . . . . .	103
<b>6</b>	<b>Conclusion and Future Studies</b>	<b>105</b>
<b>A</b>	<b>List of Acronyms</b>	<b>109</b>
<b>B</b>	<b>Additional Figures</b>	<b>113</b>
	<b>Bibliography</b>	<b>122</b>

# List of Figures

1.1	MRI maps from the same mouse . . . . .	3
2.1	Energy levels for $^1\text{H}$ . . . . .	8
2.2	Macroscopic collection of proton magnetic dipole moments and the net magnetization vector . . . . .	9
2.3	Energy absorption from the $\mathbf{B}_1(t)$ field . . . . .	11
2.4	The net magnetization vector after an excitation pulse . . . . .	13
2.5	FID and the envelope of the magnetization vector . . . . .	14
2.6	Recovery of the longitudinal magnetization, $M_z$ , after a $\pi/2$ pulse . . . . .	15
2.7	Slice select gradient . . . . .	18
2.8	Spatial encoding of the proton signal . . . . .	20
2.9	A 2D FT of $k$ -space into image space . . . . .	21
2.10	The spin echo pulse sequence . . . . .	23
2.11	The CPMG pulse sequence . . . . .	24
2.12	The PGSE sequence . . . . .	26
2.13	Diffusion ellipsoids . . . . .	29
2.14	Liquid and bound pool absorption lines . . . . .	32
2.15	Two pool model of magnetization transfer . . . . .	33
2.16	The gradient echo pulse sequence . . . . .	34
3.1	Cuprizone Mouse Chow . . . . .	39

3.2	MRI System . . . . .	41
3.3	Slice selection in the mouse brain . . . . .	42
3.4	<i>Ex vivo</i> ROIs . . . . .	46
3.5	Slice dissection for . . . . .	47
3.6	Corpus callosum dissection . . . . .	48
4.1	Weekly average mouse weights . . . . .	51
4.2	Weekly normalized $T_2w$ values in the CC and EC . . . . .	52
4.3	Weekly MTR values in the CC and EC . . . . .	53
4.4	Weekly $T_2w$ signal intensity images and MTR maps for a cuprizone mouse . . . . .	55
4.5	$T_1$ vs week in the corpus callosum . . . . .	60
4.6	$T_2$ vs week in the corpus callosum . . . . .	61
4.7	Representative Relaxometry metric maps . . . . .	63
4.8	Weekly mean diffusivity in the corpus callosum . . . . .	64
4.9	Weekly radial diffusivity in the corpus callosum . . . . .	65
4.10	Weekly axial diffusivity in the corpus callosum . . . . .	67
4.11	Weekly fractional anisotropy in the corpus callosum . . . . .	68
4.12	Representative DTI metric maps . . . . .	69
4.13	Weekly magnetization transfer rate values in the corpus callosum . . . . .	70
4.14	Weekly transverse relaxation time of the liquid pool in the corpus callosum . . . . .	71
4.15	Weekly transverse relaxation time of the bound pool in the corpus callosum . . . . .	72
4.16	Weekly longitudinal relaxation rate of the liquid pool values in the corpus callosum . . . . .	73
4.17	Weekly bound pool fraction in the corpus callosum . . . . .	74
4.18	Representative qMTI metric maps . . . . .	75
4.19	5000x EM image of a control mouse corpus callosum at week 2 . . . . .	81
4.20	5000x EM image of a control mouse corpus callosum at week 3 . . . . .	82
4.21	5000x EM image of a cuprizone fed mouse corpus callosum at week 2 . . . . .	83

4.22	5000x EM image of a cuprizone fed mouse corpus callosum at week 3 . . . . .	84
4.23	Excess swelling of glial cell processes in control corpus callosum . . . . .	85
4.24	15 000x EM image of a cuprizone fed mouse corpus callosum . . . . .	86
4.25	Scatter plots for the MRI and EM correlations in the corpus callosum . . . . .	90
B.1	Individual normalized $T_2w$ mouse measurements . . . . .	114
B.2	Individual MTR mouse measurements . . . . .	115
B.3	Individual $T_1$ mouse measurements . . . . .	116
B.4	Individual $T_2$ mouse measurements . . . . .	116
B.5	Individual $\langle D \rangle$ mouse measurements . . . . .	117
B.6	Individual $\lambda_{\perp}$ mouse measurements . . . . .	117
B.7	Individual $\lambda_{\parallel}$ mouse measurements . . . . .	118
B.8	Individual FA mouse measurements . . . . .	118
B.9	Individual $R$ mouse measurements . . . . .	119
B.10	Individual $T_2^A$ mouse measurements . . . . .	119
B.11	Individual $T_2^B$ mouse measurements . . . . .	120
B.12	Individual $RA$ mouse measurements . . . . .	120
B.13	Individual $f$ mouse measurements . . . . .	121

# List of Tables

3.1	Study Setup . . . . .	40
4.1	Weekly <i>in vivo</i> normalized T <sub>2w</sub> , MTR and <i>ex vivo</i> relaxometry metrics in the corpus callosum . . . . .	54
4.2	Normalized T <sub>2w</sub> and MTR weekly voxel based Spearman correlation coefficients	57
4.3	Normalized T <sub>2w</sub> and MTR combined week voxel-based and ROI-based Spearman correlation coefficients . . . . .	58
4.4	Weekly <i>ex vivo</i> DTI metrics in the corpus callosum . . . . .	66
4.5	Weekly <i>ex vivo</i> qMTI metrics in the corpus callosum . . . . .	76
4.6	Comparison of voxel-based Spearman correlation coefficients between the control and cuprizone fed mice . . . . .	78
4.7	Comparison of MRI metric voxel-based and ROI-based Spearman correlation coefficients in combined data set corpus callosum . . . . .	79
4.8	EM measurements and distributions . . . . .	80
4.9	Correlation of MRI metrics and EM metrics in the corpus callosum . . . . .	89

# Chapter 1

## Introduction

Magnetic resonance imaging (MRI) plays an important role in the diagnosis and management of multiple sclerosis (MS) because of its ability to detect lesions prior to clinical symptoms. MRI allows us to improve our understanding of MS as well as non-invasively monitor the effects of drug therapies on individual patients. Even with its importance, MRI has limitations including the lack of correlation between conventional MRI results and tissue pathology in central nervous system disorders like MS. New MRI methods are being developed to overcome these limitations which restrict clinicians from improving the correlation between MRI findings and clinical disability. While quantitative MRI methods such as diffusion tensor imaging (DTI), magnetization transfer imaging (MTI), and multicomponent  $T_2$  (mcT2) analysis show promise in understanding changes in white matter structure and integrity associated with MS, more work is needed to understand the correlations between these MRI metrics and pathological changes. These individual methods are not sensitive to individual pathological changes, rather they are sensitive to a variety of pathologies making interpretation of individual results difficult. Inflammation, axonal damage, increased cellularity, and demyelination are processes that rarely occur in isolation in MS, further complicating interpretation of MRI results.

This thesis aims to improve the understanding of how microstructural tissue changes influence MRI metrics by developing and applying methods to the cuprizone mouse model of MS. This can improve the specificity of MRI and bridge the gap between white matter damage detected in clinical images and clinical status associated with MS.

## 1.1 MRI and White Matter Changes

MRI relies on the manipulation of the magnet moments of hydrogen nuclei using strong magnetic fields and radio-frequency (RF) electromagnetic radiation to create signals and images sensitive to different tissue structure and content. The abundance of mobile water in tissue (and the hydrogen nuclei within) is the source of MRI's predominantly soft tissue signal. The signal can be manipulated using a variety of pulse sequences which can use RF and magnetic field gradient pulses. The choice of pulse sequence sensitizes the signal, and hence the image contrast, in different ways to the proton density, longitudinal relaxation times ( $T_1$ ), and transverse relaxation times ( $T_2$ ) of the magnetization and/or the diffusion of the molecules containing the hydrogen nuclei.

The MR images shown in Figure 1.1 are of the same slice and were taken from a healthy control mouse brain on a 7T Bruker Avance III system. These images demonstrate how different MRI methods are sensitive to different features in the white matter, providing a variety of information about the tissue structure and content.

$T_1$  (see subsection 2.1.3) in tissue is sensitive to water mobility and content as well as the lattice structure the hydrogen nuclei are attached to and surrounded by.  $T_1$  times are longer in grey matter compared to white matter and are increased in white matter by demyelination, inflammation, gliosis, edema and axonal loss (1; 2).  $T_2$  (see subsection 2.1.3) in healthy white matter is attributed to water in the intra- and extra-cellular compartments

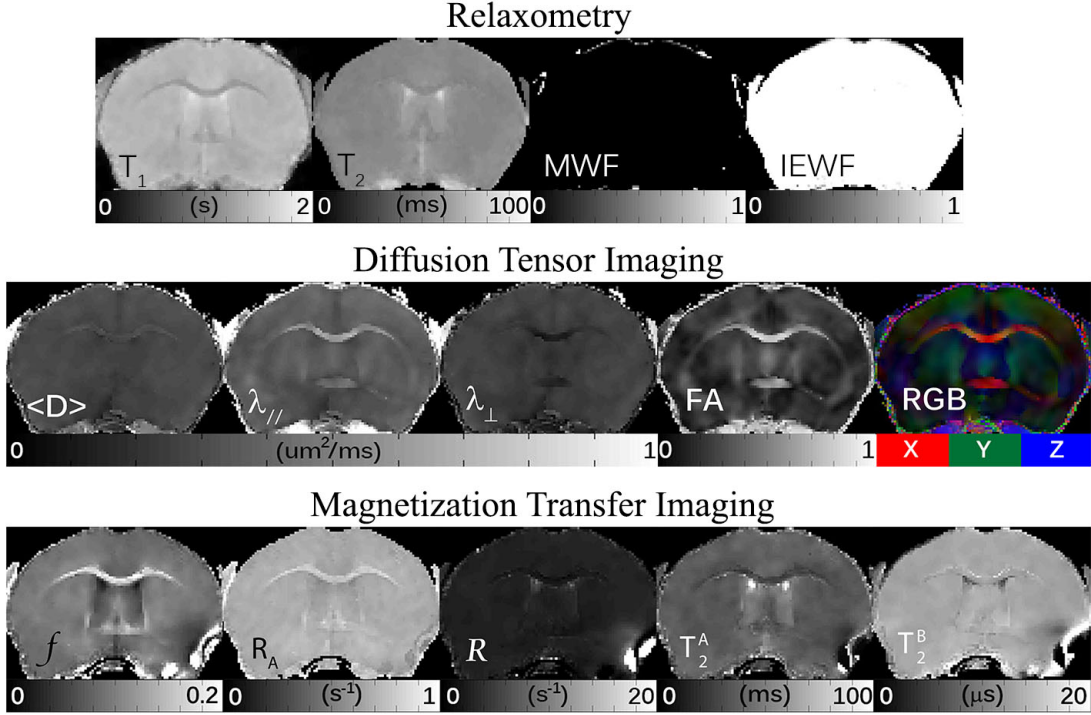


Figure 1.1: *Ex vivo* MRI maps from the same slice of a healthy control mouse brain. The corpus callosum displays varying contrast in each MRI metric map. Relaxometry metrics include longitudinal relaxation times ( $T_1$ ), transverse relaxation times ( $T_2$ ), myelin water fraction (MWF), and intra- and extra- cellular water fraction (IEWF). Diffusion tensor imaging metrics include mean diffusivity ( $\langle D \rangle$ ), axial ( $\lambda_{\parallel}$ ) and radial ( $\lambda_{\perp}$ ) diffusivity, fractional anisotropy (FA), and directionally encoded red-green-blue (RGB) maps. Magnetization transfer imaging metrics include the bound pool fraction ( $f$ ), longitudinal relaxation rates of the liquid pool ( $R_A$ ), the magnetization transfer rate between the bound and liquid pools ( $R$ ), the transverse relaxation time of the liquid pool ( $T_2^A$ ), and the transverse relaxation time of the bound pool ( $T_2^B$ ).

and is generally shorter in healthy white matter. When demyelination occurs, or in areas with increased extracellular water, the  $T_2$  value increases.

DTI metrics shown in Figure 1.1 (see subsection 2.3.3) are sensitive to tissue structure and orientation of the axonal tracts in the white matter. Mean diffusivity,  $\langle D \rangle$ , gives information on the average diffusivity occurring in a voxel while axial diffusivity,  $\lambda_{\parallel}$ , and radial diffusivity,  $\lambda_{\perp}$ , give information on the amount of diffusion running parallel and perpendicular to the white matter tracts. In healthy white matter,  $\lambda_{\perp}$  is smaller than  $\lambda_{\parallel}$ . Fractional anisotropy reveals how directional diffusion in a voxel is and is high in healthy white matter

tracts due to its directionally coherent structure.

Quantitative magnetization transfer imaging (qMTI) shown in Figure 1.1 (see subsection 2.3.4) indirectly reveals information on the hydrogen nuclei contained in myelin (bound pool). The bound pool fraction,  $f$ , represents the relative size of the bound pool compared to overall collection of hydrogen nuclei and has been shown to decrease with myelin loss, axonal loss, gliosis or increased cellularity (2).  $R_A$  and  $T_2^A$  are the rate of longitudinal relaxation and transverse relaxation time in the liquid pool, respectively, while  $T_2^B$  is related to the transverse relaxation time of the bound pool.  $R$  represents the rate of magnetization transfer between the bound pool and liquid pool.

Metrics from mcT<sub>2</sub> analysis such as myelin water fraction (MWF) and the short T<sub>2</sub>-component are also able to give insight on the distribution and content of water contained in myelin.

## 1.2 The Cuprizone Mouse Model of Multiple Sclerosis

Animal models are useful in the correlation of MRI with disease pathology due to their ease of disease induction, short disease course, controlled conditions and the choice they offer of pathologies and mechanisms that accompany each model. Animal imaging studies have proven to contribute valuable knowledge of the pathophysiology of MS, all with the goal of translating results to human studies. A variety of MS models exist providing different pathological routes and features that are complementary in increasing our understanding of MS pathophysiology.

The cuprizone model is a common model for investigating de- and re-myelination in

rodents and offers highly reproducible demyelination in the corpus callosum of the mouse brain. Cuprizone is a copper chelator that when added to a rodent diet for 6 weeks, causes cell death of oligodendrocytes and subsequently, near complete demyelination. In the first 3 weeks of feeding, proliferation and activation of microglia and astrocytes is observed (beginning the increase in tissue cellularity) in response to the attack on the oligodendrocytes. Substantial demyelination is apparent at week 3.5 of feeding and activated microglia begin to clear myelin debris. Local and migrated oligodendrocyte precursor cells (OPCs) begin proliferation as demyelination increases between weeks 3-5. Near complete demyelination of the once myelinated axons occurs at weeks 5-6 and OPCs begin to differentiate into mature oligodendrocytes which begin remyelinating bare axons. Axon remyelination is observed at week 6 despite continued cuprizone feeding (3).

A previous study (2) using the cuprizone mouse model proposed that a multiparametric approach, where measurements from more than one quantitative MRI metric are compared and correlated with each other as well as with tissue pathology, may be a solution to the varying influence that tissue pathology has on individual MRI metrics. The study found that different *in vivo* MRI metrics follow different time courses from one another, supporting the idea that while each metric is affected by white matter pathology changes, each occurs in different proportions. They then hypothesized that normalized T<sub>2</sub>-weighted signal intensity changes co-varied more strongly with vasogenic edema as well as with tissue cellularity and that MTR co-varied more strongly with demyelination. Furthermore, the study found that  $f$  was the strongest indicator of myelin content while longitudinal relaxation rates (T<sub>1</sub> and R<sub>A</sub>) and diffusion metrics ( $\lambda_{//}$ ,  $\lambda_{\perp}$ , and FA) showed promise in indicating changes in tissue structure. While these correlations were strong, they were made in the cuprizone mouse at only week 6 of feeding making it difficult to attribute changes in MRI metrics to changes in microstructural measurements. As a solution to this as well as to improve the power of these correlations, quantitative MRI and microstructural examination at chosen time points during the disease course was completed.

# Chapter 2

## Theory

To understand how MRI works, a look at the microscopic properties of the nuclei being imaged is necessary. MRI takes advantage of the resonance phenomenon that arises from the interaction of the nuclei in the tissue and the magnetic field applied.

### 2.1 Nuclear Magnetic Spin Systems

#### 2.1.1 Magnetic Dipole Moments in a Magnetic Field

Nuclei are composed of protons and neutrons that possess an intrinsic angular momentum called *spin*. All elementary particles have this fixed value intrinsic spin and its motion can be thought of as top spinning about its own axis. A charged particle (or a neutral one with an uneven charge distribution) with non-zero spin will create a magnetic dipole equivalent to a tiny bar magnet with north and south poles. The magnetic dipole moment,  $\mu$ , is a vector indicating the magnitude and direction of the magnetic dipole.

Hydrogen (composed of one proton), has a spin angular momentum  $I = \frac{1}{2}$ . From the laws of quantum mechanics, the spin angular momentum can take on values of the magnetic quantum number

$m = -I, -I + 1, \dots, I - 1, I$ . For  $^1\text{H}$ , the eigenstates are  $m = \pm\frac{1}{2}$ .

When placed in an external magnetic field,  $B_0$ , the proton magnetic moments will align parallel (high energy state) or anti-parallel (low energy state) with their individual magnitudes equal to

$$\mu = \gamma\hbar\sqrt{I(I+1)}. \quad (2.1)$$

Their  $z$ -components are equal to

$$\mu_z = \gamma\hbar m \quad (2.2)$$

while their  $x$ - and  $y$ -components are randomly oriented. The energy associated with a magnetic dipole moment in an external magnetic field,  $\mathbf{B}_0 = B_0\hat{z}$ , is

$$E = -\boldsymbol{\mu} \cdot \mathbf{B}_0 \quad (2.3)$$

making the E levels for  $^1\text{H}$ :

$$E_{\pm} = \pm \frac{\gamma\hbar B_0}{2} \quad (2.4)$$

The difference between the two energy levels is then (see Figure 2.1)

$$\Delta E = \gamma\hbar B_0 \quad (2.5)$$

where  $\gamma$  is a physical constant called the gyromagnetic ratio of the nucleus. For  $^1\text{H}$ ,  $\gamma/2\pi = 42.58 \text{ MHz/T}$ .

The probability of a proton being either spin state is determined by the Boltzmann

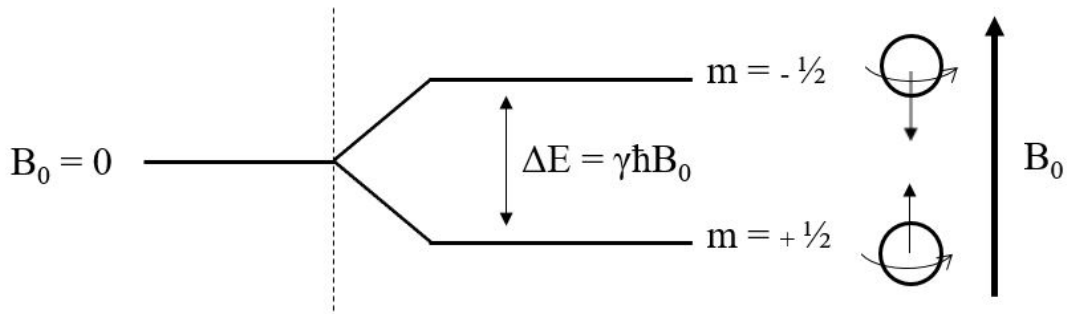


Figure 2.1: Energy levels for  $^1\text{H}$ .

distribution,

$$p_{\pm} = \frac{e^{\mp\gamma\hbar B_0/2kT}}{e^{-\gamma\hbar B_0/2kT} + e^{+\gamma\hbar B_0/2kT}} \quad (2.6)$$

where  $k$  is the Boltzmann constant ( $1.38 \times 10^{23}$  J/K) and  $T$  is the temperature (K). Through series expansion and first order approximation ( $\Delta E \ll kT$ ),

$$p_{\pm} \approx \frac{1}{2} \left( 1 + \frac{\gamma\hbar B_0}{2kT} \right). \quad (2.7)$$

The difference in the distribution of protons in the low and high energy states is,

$$p_+ - p_- = \frac{\gamma\hbar B_0}{2kT}. \quad (2.8)$$

These equations demonstrate the effects of increasing the  $B_0$  field. The energy difference is increased and consequently, so is the excess of protons in the low energy state.

At a field strength of 7.0 T, like the one used in the experiments described in this thesis,  $N_+ - N_-$  corresponds to a fractional population difference of  $24 \times 10^{-6}$ . For a million proton sample, there will be 24 more protons in the lower energy state than the high energy state. A typical MRI voxel volume contains  $10^{21}$  protons making the excess number of protons in the low energy state to be  $2.4 \times 10^{16}$ . This produces an observable magnetic

dipole moment.

The magnetic dipole moment of a single proton is extremely small and so it is useful to consider them as a macroscopic collection in a volume. The net magnetization vector,  $\mathbf{M}$ , is used:

$$\mathbf{M} = \sum_{n=1}^N \boldsymbol{\mu}_n \quad (2.9)$$

where  $N$  is the number of protons in the sample.

At equilibrium, a collection of protons will have a random orientation to each of its spins due to thermal random motion and thus no net magnetization will exist. The net magnetization vector is made of 2 components: a longitudinal ( $M_z$ ) and a transverse component ( $M_{xy}$ ). When placed in a magnetic field,  $B_0$ , the random orientation of the proton spins around the  $z$ -axis causes the transverse component to cancel and thus only longitudinal magnetization exists,  $\mathbf{M} = M_0 \hat{z}$ , dependent on the excess number of protons in the low energy state (see Figure 2.2).

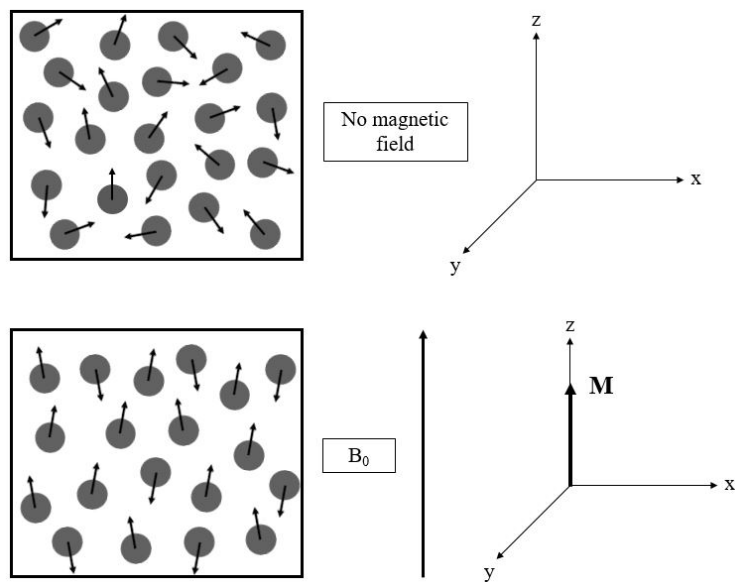


Figure 2.2: Macroscopic collection of proton magnetic dipole moments and their contribution to the net magnetization vector,  $\mathbf{M}$ . In the absence of an applied magnetic field,  $\mathbf{M} = 0$ . When  $B_0 \hat{z}$  applied,  $\mathbf{M} = M_0 \hat{z}$

### *Larmor Frequency*

The magnetic field exerts a torque  $\boldsymbol{\mu} \times \mathbf{B}$  on the protons rotating dipoles causing them to precess around that field at a characteristic rate called the *Larmor frequency*,  $\omega_0$ , where

$$\omega_0 = \gamma B_0 \tag{2.10}$$

and

$$f_0 = \omega_0/2\pi. \tag{2.11}$$

My experiments used a 7.0 T magnetic field which results in a Larmor frequency  $f_0 = 300$  MHz.

By convention, the  $B_0$  field is oriented parallel to the  $z$ -axis on a 3 dimensional Cartesian coordinate system. Two frames of reference are used to conceptualize the interaction of the protons with the magnetic fields: the laboratory frame and the rotating frame. The laboratory frame is a stationary reference frame from the observers point of view. In this frame, the protons individual magnetic moments precess around the  $z$ -axis as described previously. The rotating frame has the axis spinning at the precessional frequency of the protons such that they appear stationary when rotating at the same frequency.

## **2.1.2 The RF Pulse and Resonance**

Manipulating desired protons through the application of applied magnetic fields is the essence of magnetic resonance imaging. Protons in the low energy state are able to transition to the high energy state by absorbing energy equal to the energy separation between the states. By manipulation of Equation 2.5, Equation 2.10 and Equation 2.11, it can be shown that this energy separation is equal to  $hf_0$ . This energy is delivered in the form of radio-frequency electromagnetic radiation, called the  $\mathbf{B}_1(t)$  field, with a specific frequency equal to the pro-

tons precessional frequency (see Figure 2.3). In the classical approach to this process, the

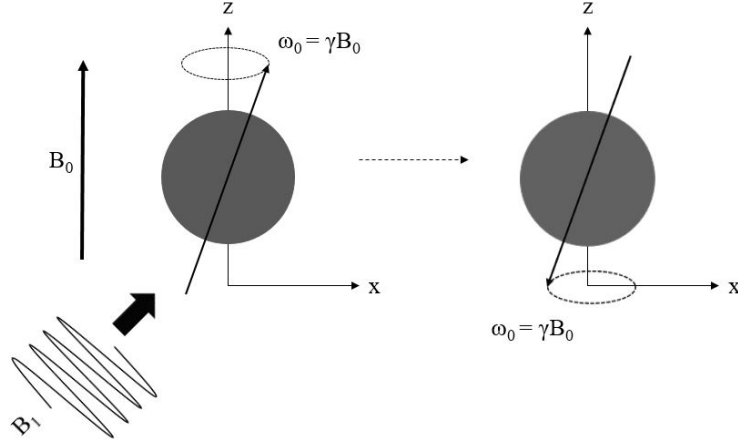


Figure 2.3: A proton with  $m = +\frac{1}{2}$  absorbing energy from the  $\mathbf{B}_1(t)$  field causing a transition to the  $m = -\frac{1}{2}$  energy level.

$\mathbf{B}_1(t)$  field is a sinusoidal wave applied orthogonally to the  $B_0$  field,

$$\mathbf{B}_1(t) = B_1^e[\cos(\omega_{rf}(t) + \phi)\hat{\mathbf{x}} - \sin(\omega_{rf}(t) + \phi)\hat{\mathbf{y}}] \quad (2.12)$$

where  $B_1^e(t)$  is the pulse envelope function,  $\omega_{rf}$  is the frequency of the applied pulse and  $\phi$  is the initial phase angle (4).

The sinc pulse is a common shape for the  $\mathbf{B}_1(t)$  envelope and is defined as,

$$B_1^e(t) = A \text{sinc}[\pi \Delta f(t - \tau_p/2)] \quad \text{for } 0 \leq t \leq \tau_p/2 \quad (2.13)$$

where  $\tau_p$  is the pulse time length and  $A$  is a constant determined by the flip angle. In the frequency domain, sinc pulses become rectangular pulses defines as

$$p(f) = \prod \frac{f - f_c}{\Delta f} e^{i2\pi(f-f_c)\tau_p/2} \quad (2.14)$$

where  $\Delta f$  is the frequency bandwidth centered on the Larmor frequency,  $f_c$ . This function

becomes particularly useful when selecting a slice of the volume with a range of specific frequencies (See subsection 2.2.1).

The number of protons that absorb this energy depends on the amplitude and duration of the  $\mathbf{B}_1(t)$  field, which allows the longitudinal magnetization to assume different values along the  $z$ -axis. In the rotating frame, the  $\mathbf{B}_1(t)$  field appears stationary relative to the precessing protons. The net magnetization vector experiences a torque from  $\mathbf{B}_1(t)$  which causes it to tip away from the  $z$ -axis into the transverse plane. The angle of this tip away from the  $z$ -axis, called the flip angle ( $\alpha$ ), is related to the strength of the  $\mathbf{B}_1(t)$  field and the time it is applied. In the lab frame, the magnetization vector still precesses around the  $z$ -axis as is it being tipped into transverse plane. It can be visualized as cone with a growing radius.

A  $\pi/2$  pulse flips the net magnetization vector from  $\mathbf{M} = M_0\hat{z}$  to  $\mathbf{M} = M_0\hat{x}\hat{y}$  by bringing the individual proton spins into phase with each other and transitioning approximately half them to the higher energy level. This is the maximum amount of transverse magnetization the net magnetization vector can obtain. A  $\pi$  pulse flips the net magnetization vector 180 degrees, sweeping out a half circle from  $\mathbf{M} = M_0\hat{z}$  to  $\mathbf{M} = -M_0\hat{z}$  in the rotating frame (see Figure 2.4).

The signal detected from the relaxation of the proton back to equilibrium is composed purely of the transverse component of the magnetization ( $S \propto M_{xy}$ ). The rotating transverse magnetization induces voltage changes in a receiver coil with a frequency equal to that of its rotation, specifically  $\omega_0 = \gamma B_0$ . After the  $\mathbf{B}_1(t)$  field has perturbed the magnetization vector and been turned off, the magnetization vector will relax back to equilibrium (as described in subsection 2.1.3). The volume can be excited by several RF pulses at fixed intervals and durations to manipulate the transverse magnetization component and make it depend on different tissue properties. This is discussed further in the following subsections.

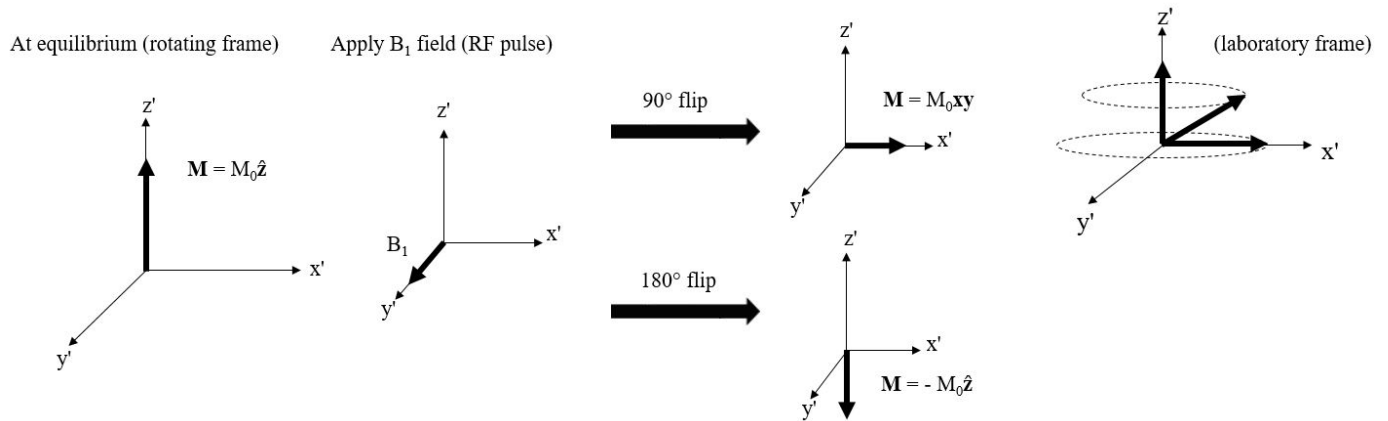


Figure 2.4: The net magnetization vector,  $\mathbf{M}$ , before and after applying a  $\mathbf{B}_1(t)$  pulse with a  $\pi/2$  flip angle (top) and  $\pi$  flip angle (bottom).

### 2.1.3 FIDs and Relaxation

#### *T<sub>2</sub> Relaxation*

The signal produced by the precessing transverse magnetic field in the receiver coil is termed the *free induction decay* (FID). It is so called due to the damped sinusoidal behavior of the rotating transverse component of the magnetization vector which decreases during its relaxation back to equilibrium. The decrease in the transverse magnetization is caused by the individual proton spins dephasing from small local magnetic inhomogeneities intrinsic to the sample of the structure. Some protons will experience a slightly stronger magnetic field while some will experience a slightly weaker magnetic field, causing them to precess at slightly different frequencies. As time passes, the spins tend towards a random distribution around the  $z$ -axis, causing no transverse magnetization to exist (see Figure 2.5). The decay of the FID envelope is governed by the  $T_2$  decay constant called the *spin-spin relaxation time*.  $T_2$  represents the time the FID signal takes to decrease by a factor of  $e$ , or 37 % of its maximum value. The transverse magnetization decay follows the equation,

$$M_{xy}(t) = M_0 e^{-t/T_2}. \quad (2.15)$$

Rotating frame  $x'y'$  plane

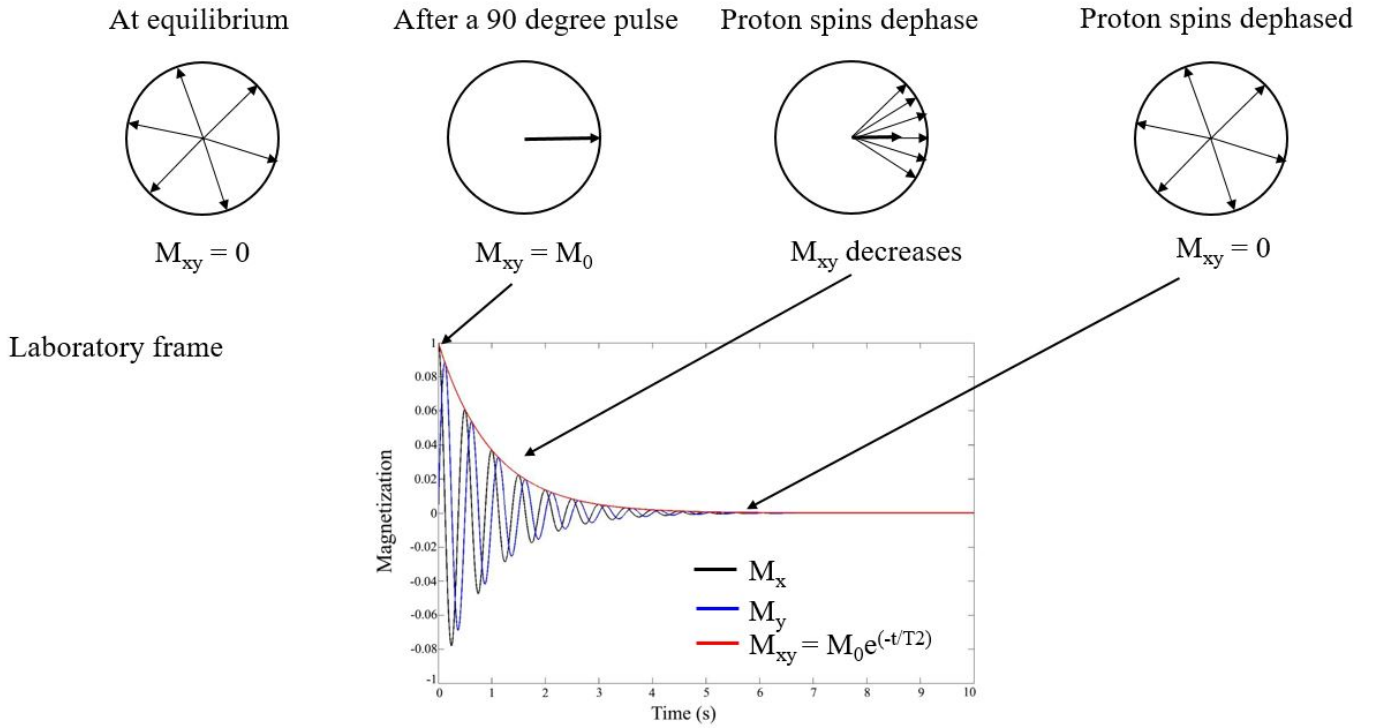


Figure 2.5: Individual proton spins in the  $x'y'$  plane and rotating frame with the corresponding FID created by the  $x$  and  $y$  components as well as the envelope of the magnetization vector.

Protons in different molecular environments will have different  $T_2$  times. Protons in cerebral spinal fluid (CSF) are rapidly moving causing the effects of magnetic field inhomogeneities to cancel. CSF will then have a long  $T_2$  time (5). Protons in larger non-moving structures, such as myelin, will have short  $T_2$  times due to stationary magnetic field inhomogeneities.

When magnetic field inhomogeneities include imperfections in  $B_0$ , spins dephase quicker and can be modeled as  $T_2$  shortening to  $T_2^*$ .

### $T_1$ Relaxation

$T_1$  relaxation is also called the *spin-lattice relaxation time* and governs the recovery of the longitudinal magnetization (Figure 2.6). Mathematically this recovery after a  $\pi/2$  excitation pulse is described by,

$$M_z(t) = M_z[1 - e^{-t/T_1}]. \quad (2.16)$$

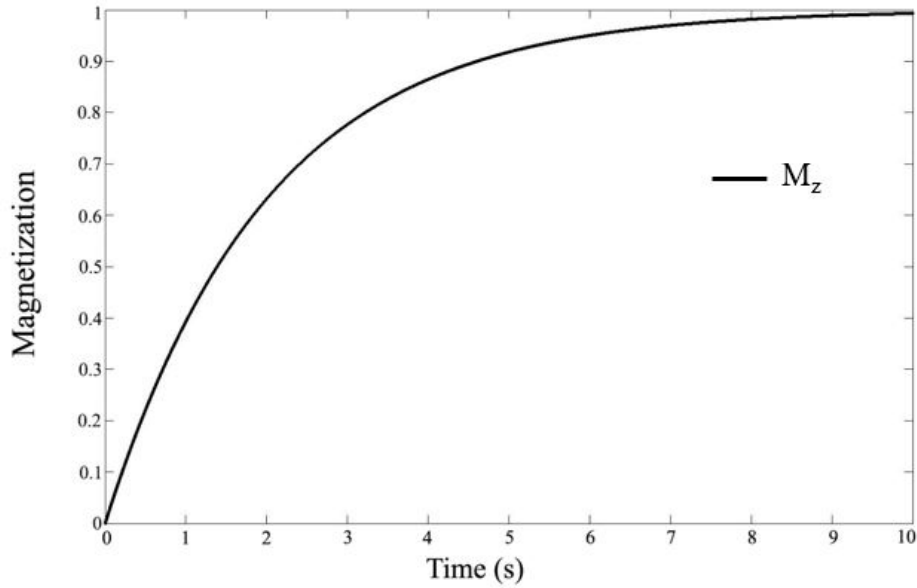


Figure 2.6: Recovery of the longitudinal magnetization,  $M_z$ , after a  $\pi/2$  pulse.

$T_1$  is the time it takes for the longitudinal relaxation to recover by a factor of  $(1 - e)$  or 63% of its original value after being displaced by a  $\mathbf{B}_1(t)$  field.  $T_1$  relies on the protons losing energy to the surrounding molecular lattice thus the structure of the lattice in part determines  $T_1$  relaxation. Furthermore, energy transfer is most efficient when the vibrational frequency range of the lattice contains that of the precessing protons. Molecules vibrate at different frequencies with varying ranges depending on their size and movement therefore  $T_1$  relaxation is dependent on the physical characteristics of the tissue (5). Specifically lipids, proteins, and fats have vibrational frequencies that allow them to undergo the most efficient

energy transfer with excited protons.

If the  $B_0$  field and consequently the Larmor frequency is increased, the vibrational frequency range of the molecular structure may not overlap with  $\omega_0$  causing increased  $T_1$  times.

## 2.2 Magnetic Resonance Imaging (MRI)

It has been discussed how a sample of protons can be manipulated through the application of magnetic fields to produce a signal that can be detected by a receiver coil. The proceeding section will discuss how the signals can be localized in order to probe desired slices of a sample and how the signal is reconstructed into an image.

### 2.2.1 Signal Localization

If a sample of protons is placed in a uniform external magnetic field and a perfect single  $\pi/2$  RF pulse is applied, protons throughout the entire sample will be excited and all precess with the frequency. In order to produce images containing only a portion (or slice) of the sample, only protons from that slice are required to be excited. This is accomplished by the use of RF excitations and magnetic field gradients, a process called spatial localization.

Recall the detected signal from a sample of protons has the same frequency as the protons producing the signal. In order to probe different sections of a sample, the precession frequency of the protons must vary from point to point. Magnetic gradients are used to vary the magnetic field over a sample in order to vary the precessional frequency of the protons in the sample. These gradients are used in addition to the main magnetic field and are only applied temporarily.

Gradients work by linearly varying magnetic field strength over a distance along one axis of the sample. Proton precession frequency varies corresponding to their position along the applied gradient. The localization in a 3D volume requires the use of 3 gradients: the slice select, frequency encode and phase encode gradients. The following will describe the format of a typical axial slice. Any other slice can be obtained by changing the direction of the axes. In the following explanation phase and frequency encoding are applied in the  $y$  and  $x$  directions respectively, and can also be switched.

### *Slice Select Gradient*

The slice select gradient in conjunction with a RF pulse selects a specified thin section of the tissue. The slice select gradient is applied across the entire sample which causes the protons to precess with different frequencies depending on their position while the RF pulse selectively excites protons by containing only the desired matching narrow band of frequencies (see Figure 2.7). The RF pulse is applied to the entire sample although protons outside of the specified frequency band precess at a different frequency and will not be excited. A temporary setback to this gradient method is that it causes dephasing of spins throughout the sample. The solution is a re-phasing gradient, equal to half the area of the original gradient and opposite in polarity, applied to rephase spins after the slice is selected. This is the first of 3 gradients used to localize the proton signal.

### *Phase Encode Gradient*

The phase encode gradient (PEG),  $G_y$ , is used to encode the position of the protons in each column within the selected slice. This is done by linearly varying the magnetic field within the slice along the  $y$ -axis. This is done before the frequency encode gradient applied. Phase encoding causes the phase difference between protons at different positions along the  $y$ -axis to be varied once the PEG is turned off. The protons spins will have a phase angle of

$$\phi(y) = -\gamma G_y y T_{G_y} \tag{2.17}$$

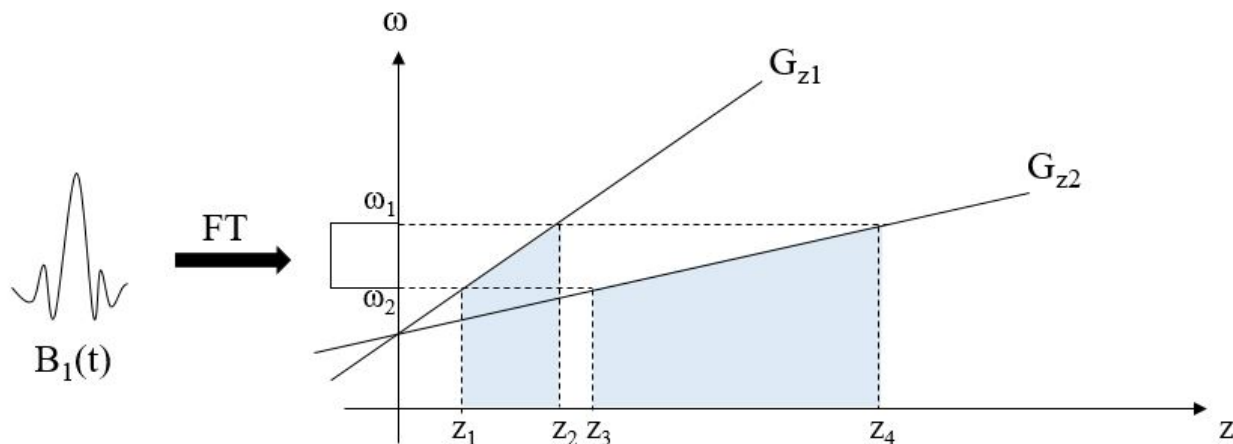


Figure 2.7: Application of a gradient in combination with a RF pulse to select a slice along the  $z$ -axis. The slice thickness depends on the gradient chosen,  $G_{z1}$  or  $G_{z2}$ , and the bandwidth of the  $B_1(t)$  pulse.

once the PEG is removed, where  $T_{G_y}$  is the period of time the PEG is applied. The phase shift experienced by the protons increases linearly to the maximum phase shift on one side of the gradient to the edge of the field of view (FOV) while the frequency decreases linearly to maximum negative phase shift towards the opposite end of the FOV. Thus the position of the protons along the  $y$ -axis is encoded by the amount of phase shift it inherits. Once the PEG is removed the protons phase shift remains although the precessional frequency reverts back to the Larmor frequency. This causes the selected slice to be further sectioned into rows, each with its own phase shift. The strength of the PEG, also known as the slope of the PEG, is varied for each repetition interval (e.g. from positive to negative polarity) to produce a positionally dependent phase shift at each position along the phase encode direction. The spatial position is decoded using the Fourier transform after all of the data has been collected.

### *Frequency Encode Gradient*

Once the slice has been selected, the slice select gradient is turned off. The protons in this selected slice have been excited and contain transverse magnetization. Once the gradient is

off, these protons once again all experience the same magnetic field ( $B_0$ ) and precess with the same frequency. The frequency encode gradient (FEG) is then used to encode the position of the protons within the sample by linearly varying the magnetic field within the slice along the  $x$ -axis. The Larmor frequency of a proton spin at a position  $x$  immersed in a  $B_0$  field, after excitation in combination with the FEG ( $G_x$ ) is

$$\omega(x) = \omega_0 + \gamma G_x x. \quad (2.18)$$

In this explanation, the slice is selected along the  $z$ -axis using the slice select gradient and the spins are then spatially encoded along the  $x$ - and  $y$ - axis. The FEG applied during the formation and decay of the proton signal. For a typical axial image, the FEG is applied along the  $x$ -axis and spins are frequency encoded depending upon their position along the FEG. Protons at the center of the gradient, in the middle of the FOV, experience no frequency shift. The frequency shift experienced by the protons increases linearly to  $+f_{max}$  on one side of the gradient to the edge of the FOV while the frequency decreases linearly to  $-f_{max}$  to the opposite end of the FOV. The protons experience the frequency shifts only when the gradient is on. This means the signal must be acquired while the FEG is on. This causes the selected slice to be further sectioned into rows, each with its own frequency shift. The signal from each row is then amplified, digitized and Fourier transformed to produce a data set containing the amplitude of the signal in each column versus its frequency (and therefore) position in the FOV.

### *k-space and Image Reconstruction*

When the frequency and phase shifts are combined, as they are during frequency encode gradient, each pixel in the selected slice will have its own unique phase shift and frequency shift. In a 256x256 image, the Fourier transform will reveal 256 component frequencies, each having 256 unknown phase components. In order to determine the 256 phase components

(the position along the  $y$ -axis) at each frequency (the position along the  $x$ -axis) the signal of each pixel must be measured 256 times, each time giving new phase information. This is why the PEG must be varied each repetition interval. Each row in data space contains signal obtained from the entire image at each repetition time,  $T_R$ .

MR data is initially stored in a 2D matrix of positive and negative spatial frequency values as complex numbers. In a typical axial image, data is encoded along the  $k_x$  axis by the frequency encode gradient and along the  $k_y$  axis by the incremented phase encode gradient (Figure 2.8). Each axis ranges from  $-f_{max}$  to  $+f_{max}$ . Prior to the application of the FEG, a gradient pulse called the readout dephaser, is applied for half the time of the FEG in order to encode the  $x$ -axis in  $k$ -space from  $-f_{max}$  to  $+f_{max}$  rather than 0 to  $2f_{max}$ .  $k$ -space is first Fourier transformed along each row of the  $k$ -space matrix, stored in an intermediate matrix and then Fourier transformed along each column of the intermediate matrix. This 2D Fourier transform converts the data in the  $k$ -space matrix into image space to produce a meaningful image (Figure 2.9).

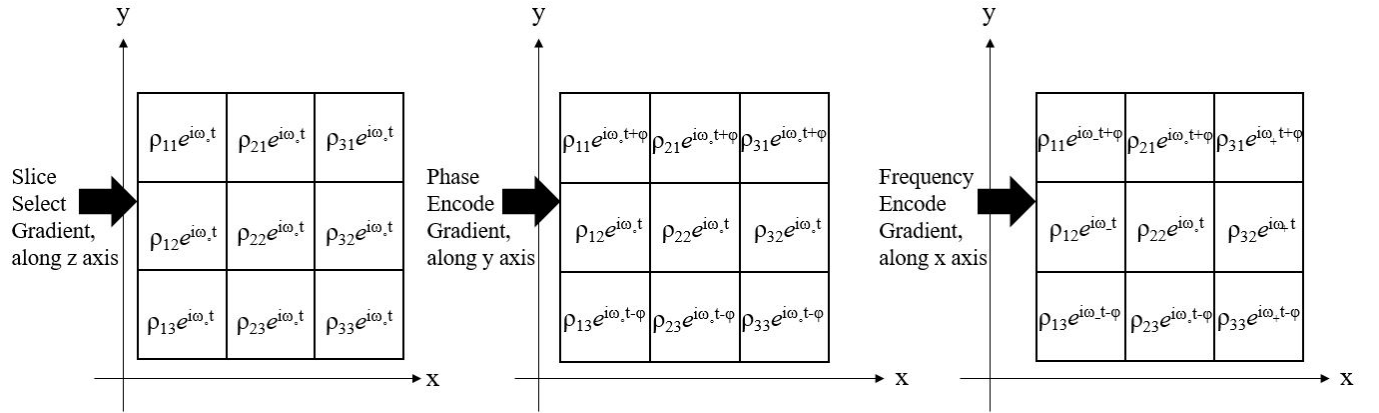


Figure 2.8: After the application of all 3 spatial localization gradients, each voxel becomes frequency and phase encoded. The range of frequencies created by  $G_x$  is  $\omega = \omega_-, \omega_0$ , and  $\omega_+$ . The range of phases created by  $G_y$  is  $\phi = \phi_-, 0$ , and  $\phi_+$ .

Signal with the highest amplitude is contained at the centre of  $k$ -space where the lowest spatial frequencies are located. Higher frequency data is contained at the outer parts of

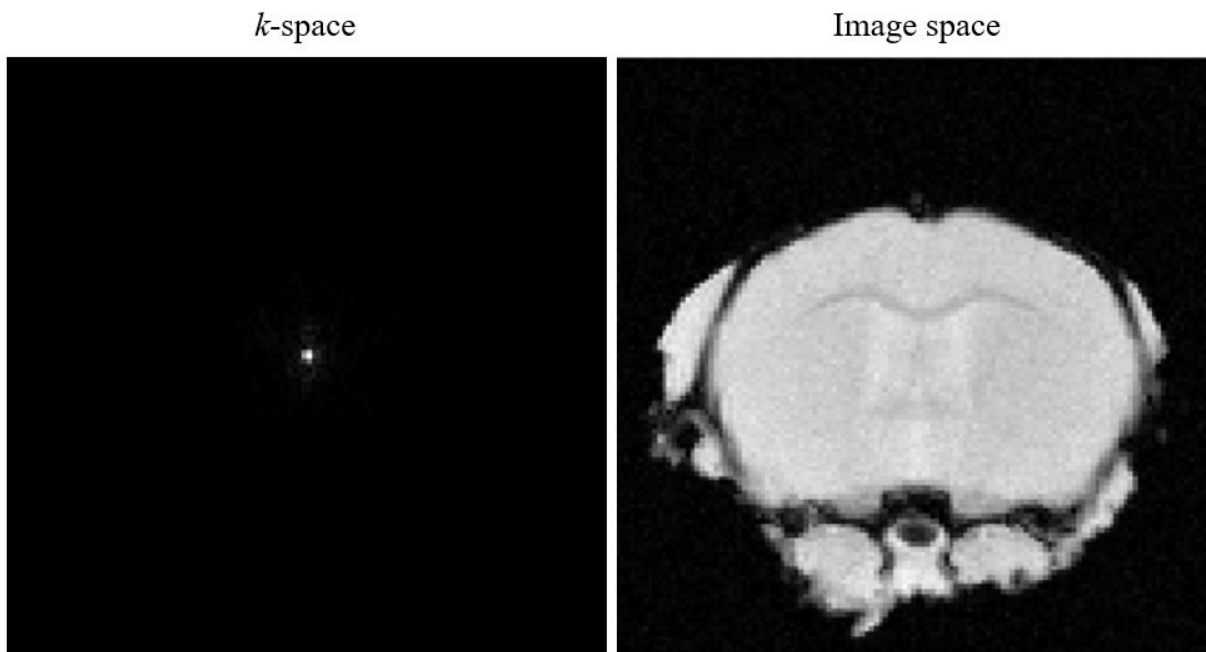


Figure 2.9: A 2D FT of  $k$ -space into image space.

the  $k$ -space matrix and have low signal amplitude. Fine detail of the image is stored in the higher spatial frequencies. A reconstructed image without high spatial frequency data loses resolution and fine detail and becomes fuzzy. Removing the bulk of signal that is stored at low spatial frequency gives an image lacking bulk signal contrast.  $k$ -space can be filled in various ways other than filling in each row incrementally. This is beyond the scope the thesis and the reader is referred to Bushberg (5) to explore other methods of data acquisition.

## 2.2.2 The Spin Echo

Tissue contrast can be varied to reveal different tissue features by manipulating the protons in the tissue in certain ways to have their signal more (or less) dependent on  $T_1$  relaxation,  $T_2$  relaxation, proton density or other properties like diffusion (subsection 2.3.3) or magnetization transfer (subsection 2.3.4). The manipulation of the protons is executed by varying the timing, order, polarity and repetition frequency of the RF pulses and magnetic field gra-

dients (distinct from signal localization gradients). The spin echo pulse sequence is one of the major pulse sequences in MR imaging. How the sequence works as well as a description of the parameters used in the sequence are described below.

A spin echo can be generated by 2 RF pulses separated by a period of time ( $T_E/2$ ) where  $T_E$  is the time of the echo signal. The first RF pulse, a  $\pi/2$  pulse applied say in the  $x$  direction, excites the protons creating maximum transverse magnetization that produces an FID, decaying with the time constant  $T_2^*$ . After a period of  $T_E/2$ , a second RF pulse, a  $\pi$  pulse applied in an orthogonal direction, say the  $y$  direction, inverts the individual spins. After inversion, the direction of motion of individual spins is reversed and they begin to converge. This is the beginning of the spin echo. The peak of the echo marks the  $T_E$  time and occurs at maximum convergence of the spins. The echo then decays with the  $T_2^*$  time constant as the spins dephase due to variations in their precession frequencies (see Figure 2.10) The amplitude of the spin echo is  $T_2$ -weighted (4):

$$S(T_E) = M_0 e^{-T_E/T_2}. \quad (2.19)$$

The signal is thus time dependent. The time between the 2 RF pulses can be adjusted to vary tissue contrast between tissues with different  $T_2$  times.

## 2.3 Magnetic Resonance Imaging Methods

There are many MRI pulse sequences that can be used obtain the desired signal weighting and so only MRI methods used in this thesis experiment are discussed.

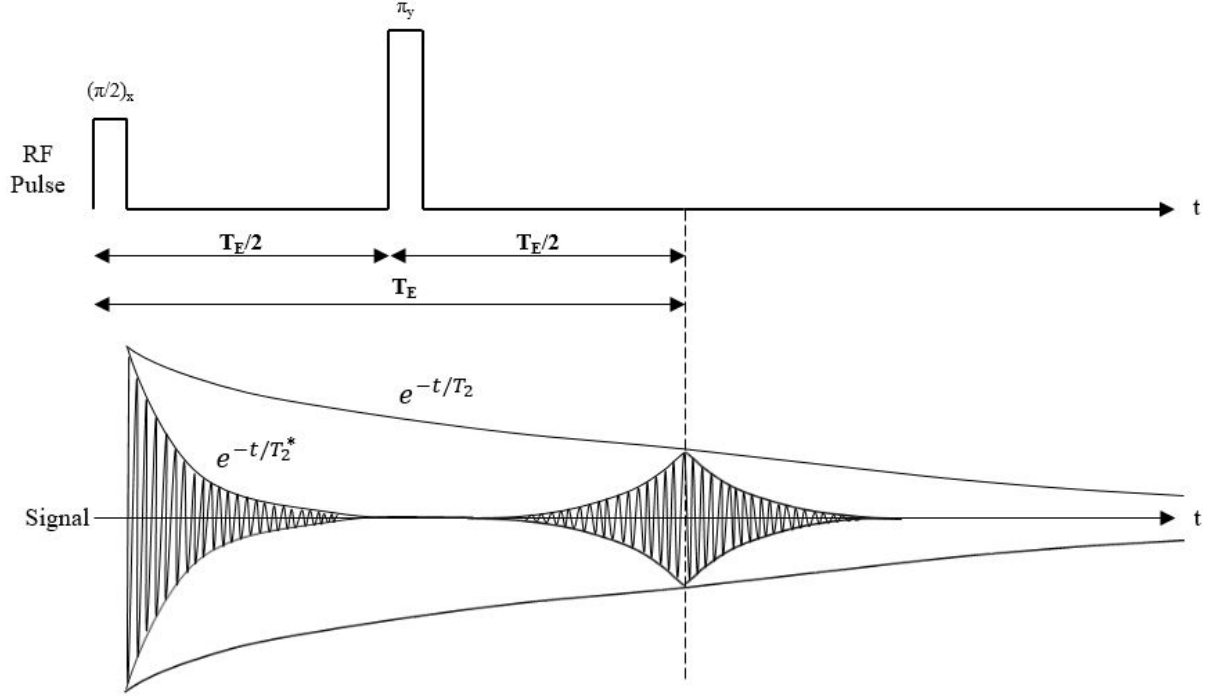


Figure 2.10: The spin echo pulse sequence. The detected signal at  $t = T_E$  is proportional to  $e^{-T_E/T_2}$ .

### 2.3.1 $T_2$ -weighted Imaging

The Carr-Purcell Meiboom-Gill (CPMG) pulse sequence (see Figure 2.11) is used in this experiment to calculate the *in vivo* and *ex vivo* single component  $T_2$  decay curve. The FID decay is governed by  $T_2^*$  decay while the envelope of the multiple echoes decays with  $T_2$ . Signals from the CPMG pulse sequence can be fit to the equation:

$$S(n\tau) = S_0 e^{-n\tau/T_2} + C \quad \text{for } n = 2, 4, 6, 8, \dots \quad (2.20)$$

with  $T_R$  held constant, and  $T_2$  can be estimated. By varying the phase encoding gradient strength for each  $\pi$  pulse, each echo produced is spatially encoded with a different phase encoding. Each echo then contains data for a different line of  $k$ -space. This method is known as Rapid Acquisition with Relaxation Enhancement (RARE). If  $n$  echoes are acquired per  $T_R$  then the sequence is said to have a RARE factor of  $n$  (where  $n$  is a power of 2) and

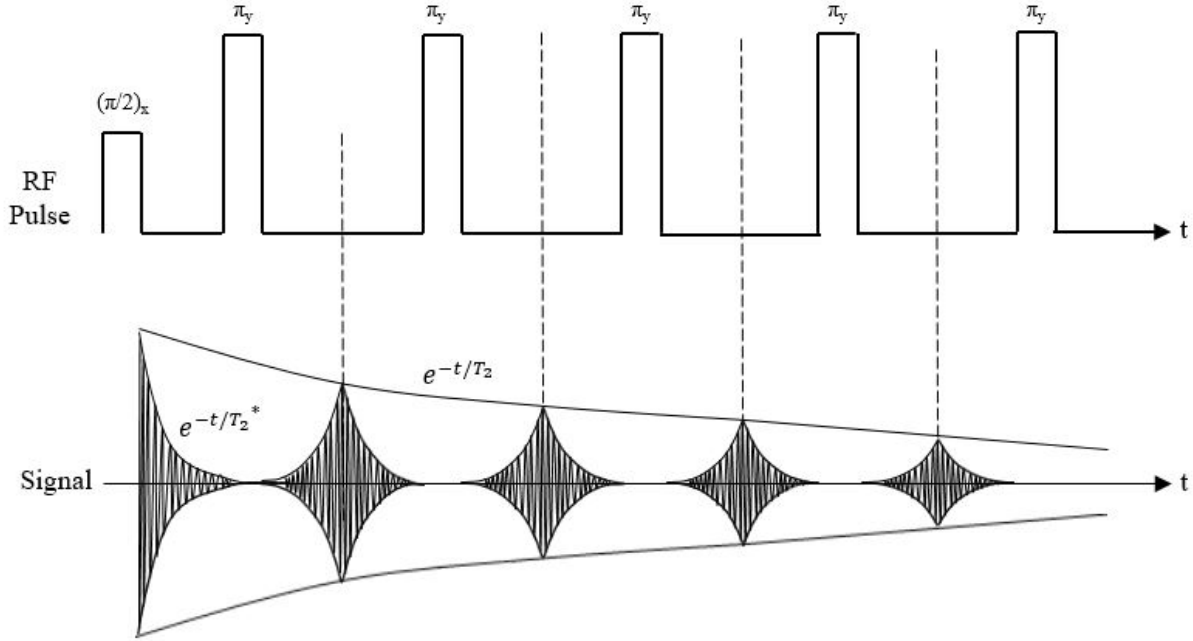


Figure 2.11: The CPMG pulse sequence.

image acquisition becomes  $n$  times faster.

### 2.3.2 Relaxometry

Relaxometry is referred to as the measurement of  $T_1$  and  $T_2$  relaxation times. A series of RARE acquisitions can be collected and the echo images can be used to calculate  $T_1$  and  $T_2$  values.  $T_1$  is calculated from echo images generated as described below, while  $T_2$  is calculated as described in subsection 2.3.1.

The amplitude of the spin echo signal at  $t = T_E$  in the spin echo sequence described above is (4):

$$S(T_E) \propto M_z^0 (1 - 2e^{-(T_R - T_E/2)/T_1} + e^{-T_R/T_1}) e^{-T_E/T_2}. \quad (2.21)$$

In practice,  $T_E \ll T_R$  and this equation simplifies to

$$S(T_E) \propto M_z^0(1 - e^{-T_R/T_1})e^{-T_E/T_2}. \quad (2.22)$$

$T_1$ -weighting can be selectively achieved by varying  $T_R$  and keeping  $T_E$  short and constant. The  $T_2$ -weighting factor can be ignored and Equation 2.22 can be written as

$$S(T_R) \propto M_z^0(1 - e^{-T_R/T_1}). \quad (2.23)$$

### 2.3.3 Diffusion Tensor Imaging (DTI)

MRI can also be used to measure the amount of motion, or diffusion, of the precessing protons by utilizing inherited phase shifts that arise from multiple gradient encodings. Measuring diffusion is useful due to its ability to give insight on tissue structure and organization, specifically of the white matter tracts that cannot be found through relaxometry.

#### Diffusion

Diffusion is the process of random molecular thermal motion, also known as Brownian motion. Unrestricted diffusion can be described by the equation  $\langle x \rangle^2 = 2D(t_2 - t_1)$  where  $\langle x \rangle^2$  is the mean-squared diffusion distance of the molecule along one direction,  $D$  is the diffusion coefficient ( $um^2/ms$ ) and  $(t_2 - t_1)$  is the diffusion time. In 3 dimensions, this equation becomes:  $\langle \mathbf{r} \rangle^2 = 6\mathbf{D}(t_2 - t_1)$ .

$\mathbf{D}$  is called the diffusion tensor and is a 3x3 matrix that describes molecular movement in 3 directions:

$$\mathbf{D} = \begin{pmatrix} D_{xx} & D_{xy} & D_{xz} \\ D_{yx} & D_{yy} & D_{yz} \\ D_{zx} & D_{zy} & D_{zz} \end{pmatrix} \quad (2.24)$$

## The PGSE Sequence

The pulse sequence used in this experiment to measure diffusion is called the pulsed gradient spin echo (PGSE) sequence and is pictured in Figure 2.12. This sequence is the familiar spin

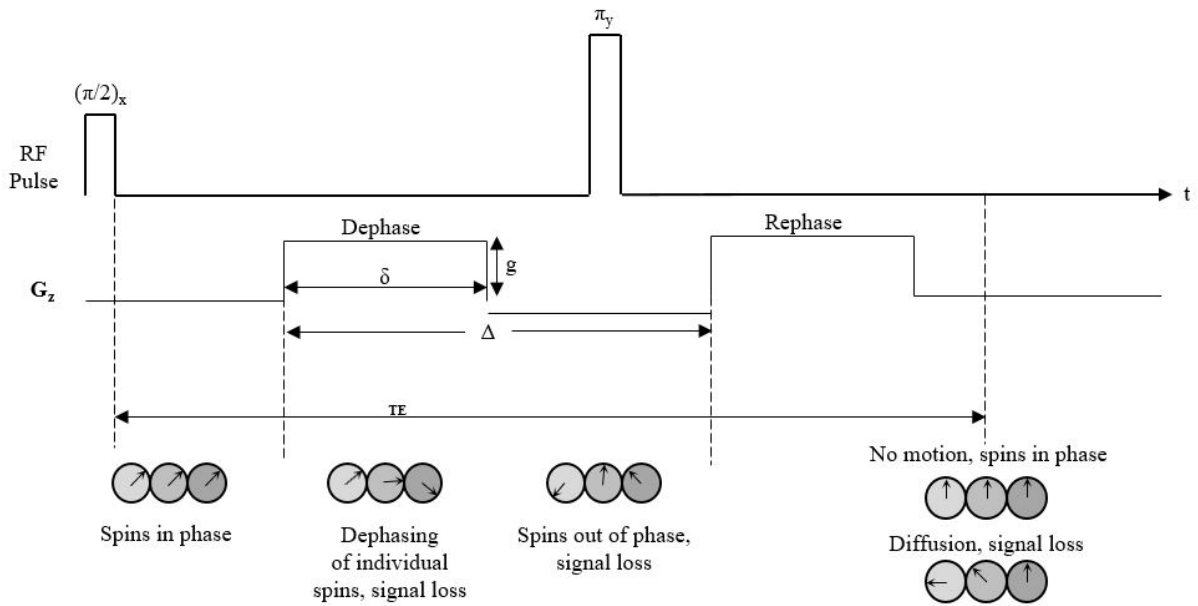


Figure 2.12: The PGSE sequence and its de- and rephasing gradient effects on proton spins.

echo sequence with 2 additional gradients applied before and after the  $\pi$  RF pulse used to magnetically label protons attached to moving molecules such as water (6). In the PGSE sequence, the diffusion weighted signal is

$$S(T_E) \propto M_0^z (1 - e^{-T_R/T_1}) e^{-T_E/T_2} e^{-b(T_E)D} \quad (2.25)$$

where  $b$  is known as the diffusion weighted factor. This factor includes all diffusion and imaging gradient effects (such as the duration and separation of the diffusion gradients,  $\delta$  and  $\Delta$ , respectively) and characterizes the diffusion signal attenuation. By holding all variables constant except for those introduced by diffusion, the signal can be written

$$S(t) = S_0 e^{-b(t)D} \quad (2.26)$$

which was Stejskals and Tanners solution to the modified Bloch-Torrey equation (7).

Now it can be seen that by varying  $b$  in a series of images, the diffusion coefficient  $D$  can be determined.

### **Apparent diffusion coefficient (ADC) and the Diffusion Tensor**

Manipulating Equation 2.26 results in a new equation that  $D$  is able to be determined from:

$$\ln S(b) = -bD + \ln S(b = 0) \quad (2.27)$$

and

$$D = \frac{|\ln S(b = 0) - \ln S(b)|}{b}. \quad (2.28)$$

Above,  $S(b)$  is the echo image obtained with a diffusion weighting factor  $b$  and  $S(b = 0)$  is the echo image obtained with no diffusion weighing.

The mean apparent diffusivity coefficient considering 3 directions in a voxel is then  $\langle D \rangle = (D_x + D_y + D_z)/3$ . The mean apparent diffusivity coefficient describes the magnitude of diffusion but gives no information of the directionality of diffusion.

In biological tissue, diffusion is hindered within cells by dense macromolecule packing and high cytoplasmic viscosity while extracellularly, diffusion is hindered by tortuosity effects

(6). Tortuosity is the concept that explains how water must travel obscure paths rather than in a straight path due to hindrance by fibers, macromolecules, organelles, and other obstacles (6). This hindrance causes the measured diffusion coefficient to be less than the free diffusion coefficient,  $D$ . Thus with MRI we measure an apparent diffusion coefficient, or ADC.

The structures within biological tissues could cause the apparent diffusion to be unequal in all directions, a property called anisotropy. For instance water diffusing in axons can diffuse more easily along the axon rather than across the axon. When diffusion is anisotropic, the diffusion tensor is used in place of the ADC. This experiment wanted to inquire into diffusion along 6 directions and thus 7 images with different  $b$  values (including a non-diffusion weighted image, the  $b=0$  image) were acquired.

$D$  can now be determined from the equation derived from Equation 2.25 (8):

$$\ln S(\mathbf{b}) - \ln(S(\mathbf{b} = 0)) = -(b_{xx}D_{xx} + 2b_{xy}D_{xy} + 2b_{xz}D_{xz} + b_{yy}D_{yy} + 2b_{yz}D_{yz} + b_{zz}D_{zz}). \quad (2.29)$$

Here,  $S(\mathbf{b})$  is the echo image obtained with a diffusion weighting factor and  $S(\mathbf{b}=0)$  is the echo image obtained with no diffusion weighing. The diffusion weighting factor is now a matrix,  $\mathbf{b}$ , and is calculated for the series of diffusion weighted images collected. Once again,  $\mathbf{D}$  is estimated by varying  $\mathbf{b}$  and examining the echo signal in each voxel.  $\mathbf{D}$  was estimated using a constrained non-linear least squares method that was previously used (2).

## Diffusion Tensor Metrics

The diffusion tensor is calculated in each voxel of a diffusion weighted image and contains a large amount of information about the movement of water in that voxel. Metrics that define the amount of diffusion as well as its directionality can be derived from the eigenvectors and

eigenvalues of the diffusion tensor matrix. These metric maps simplify the interpretation of image information. Directionally encoded color maps, known as red-green-blue (RGB) maps give 2 dimensional spatial information as well as the direction and magnitude of diffusing water in the image acquired. These metrics as well as the RGB maps are discussed below.

### Eigenvalues and Eigenvectors of $\mathbf{D}$ and the ellipsoid representation of $\mathbf{D}$

Diagonalization of  $\mathbf{D}$  yields eigenvectors ( $\mathbf{e}_1, \mathbf{e}_2, \mathbf{e}_3$ ) and their corresponding eigenvalues ( $\lambda_1, \lambda_2, \lambda_3$ ) that describe the diffusion directions as well as their magnitude of diffusion along these directions (9).  $\mathbf{D}$  then becomes,  $\mathbf{D} = [\lambda_1 \ 0 \ 0, \ 0 \ \lambda_2 \ 0, \ 0 \ 0 \ \lambda_3]$  and can be visualized as an ellipsoid (see Figure Figure 2.13a). The major axis has eigenvector  $\mathbf{e}_1$  with its radius equal to the square root of  $\lambda_1$  while the radii of the minor axes, along  $\mathbf{e}_2$  and  $\mathbf{e}_3$ , are the square root of  $\lambda_2$  and  $\lambda_3$ , respectively. The mean squared displacement,  $\langle r \rangle^2$ , of the molecule is measured which then introduces the square root to the radii of the axis of the ellipse,  $\lambda$ .

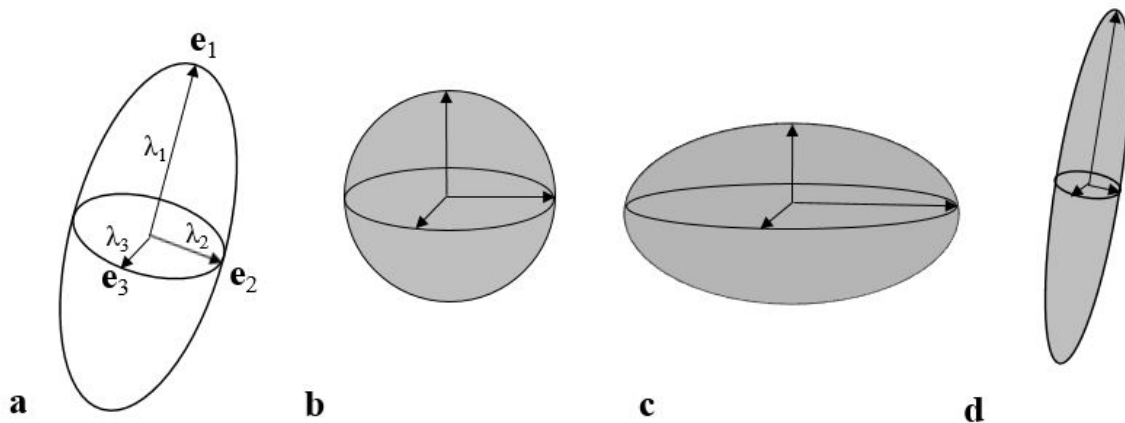


Figure 2.13: The diffusion ellipsoid (a), isotropic diffusion (b), planar anisotropic diffusion (c), linear anisotropic diffusion (d) ellipsoid representations.

### Mean Diffusivity

$$\langle D \rangle = \frac{\text{Trace}(\mathbf{D})}{3} = \frac{\lambda_1 + \lambda_2 + \lambda_3}{3} \quad (2.30)$$

Mean diffusivity defines the magnitude of diffusion in a voxel and generally increases with increased extracellular space and tissue water (2).

### Axial and Radial Diffusivity

$$\lambda_{\parallel} = \lambda_1 \quad \text{and} \quad \lambda_{\perp} = \frac{\lambda_2 + \lambda_3}{2} \quad (2.31)$$

Axial diffusivity,  $\lambda_{\parallel}$ , describes the amount of diffusion parallel to major axes of the ellipsoid, generally in the direction parallel to the white matter tract. Radial diffusivity,  $\lambda_{\perp}$ , defines the amount of diffusion running perpendicular to the major axis of the ellipsoid (along  $\mathbf{e}_1$  and  $\mathbf{e}_2$ ). Because water diffuses more easily parallel to and along a white matter tract than it does across one, it follows that  $\lambda_{\parallel}$  will be greater than  $\lambda_{\perp}$  in a healthy white matter bundle (2). Decreased  $\lambda_{\parallel}$  has been shown to be a reliable marker for axonal damage (10; 11; 12; 13) while increases in  $\lambda_{\perp}$  have been linked to demyelination distinct from axonal damage (12; 14; 15) in mouse models of white matter damage including ischemia, EAE and cuprizone.

### Fractional Anisotropy

$$FA = \sqrt{\frac{3}{2}} \sqrt{\frac{(\lambda_1 - \langle D \rangle)^2 + (\lambda_2 - \langle D \rangle)^2 + (\lambda_3 - \langle D \rangle)^2}{\lambda_1^2 + \lambda_2^2 + \lambda_3^2}} \quad (2.32)$$

Fractional anisotropy, FA, is the fraction of the total magnitude of the diffusion tensor that is anisotropic (16) and indicates if diffusion is favored more along 1 axes compared to the remaining 2. FA values range between 0, indicating diffusion is not favored in any direction (isotropic), and 1 indicating diffusion is favored in one of the measured directions (anisotropic).

Isotropic diffusion Figure 2.13b occurs when  $\lambda_1 \approx \lambda_2 \approx \lambda_3$  making the diffusion ellipsoid spherical in geometry. Planar anisotropic diffusion occurs when  $\lambda_1 \approx \lambda_2 \gg \lambda_3$  creating an oblate ellipsoid (Figure 2.13c) while linear anisotropic diffusion occurs from  $\lambda_1 \gg \lambda_2 \approx \lambda_3$  and creates a prolate ellipsoid (Figure 2.13d).

Changes in  $\langle D \rangle$ ,  $\lambda_{\parallel}$  and  $\lambda_{\perp}$  consequently cause changes in FA making its sensitivity a useful tool for studying pathological changes (17).

#### Directionally Encoded Color Maps

RGB maps are a useful tool in visualizing the direction of diffusion in an image. A colour component (R,G,B) is assigned to the  $(x, y, z)$  components of  $\mathbf{e}_1$  where  $x$  defines the left-right,  $y$  defines the front-back, and  $z$  defines the top-bottom directions. These values are multiplied by the FA value in that voxel to give a direction as well as the magnitude of diffusivity in that direction represented by the intensity of the color. Because water diffuses more easily down a white matter tract than across it, brighter voxels can indicate a path of connected white matter tracts.

$$R = |e_{1x}| FA \quad G = |e_{1y}| FA \quad B = |e_{1z}| FA \quad (2.33)$$

$\langle D \rangle$ ,  $\lambda_{\parallel}$  and  $\lambda_{\perp}$  and FA are all scalar metrics and rotationally invariant. This makes comparing these metrics between samples easier since each sample does not need to be positioned in the same orientation while collecting images.

### **2.3.4 Quantitative Magnetization Transfer Imaging (qMTI)**

Protons contained within macromolecules exist in a slightly different magnetic environment than protons in free water making their Larmor frequencies different. This means bound

pool protons (those contained in macromolecules like myelin) can be selectively excited by a narrowband RF pulse apart from free pool protons (Figure 2.14). The RF pulse used is called an off resonance pulse because its frequency is shifted away from the Larmor frequency of the bulk of protons (in the free pool). Magnetization transfer from the excited protons in the bound pool to protons in the free pool occurs creating partial saturation of the free pool. This saturation causes signal attenuation in the free pool after the on resonance RF pulse is applied when compared to the signal obtained with no off resonance RF pulse.

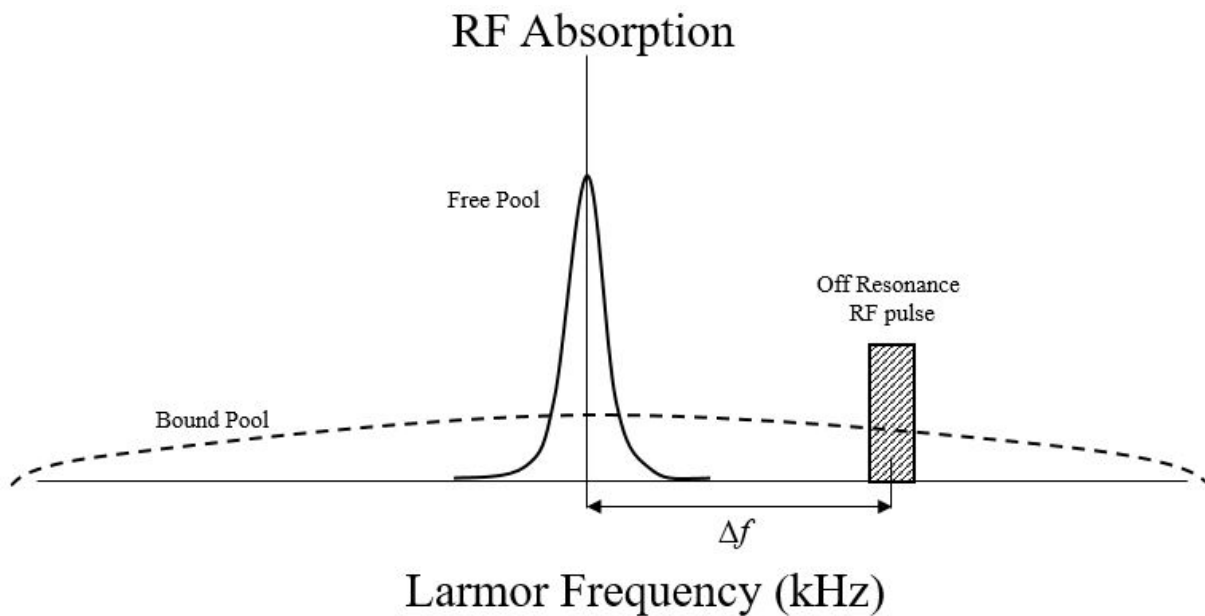


Figure 2.14: Magnetization transfer contrast is achieved using an off resonance RF pulse to saturate bound pool protons apart from free pool protons.

Bound pool protons have  $T_2$  relaxation times too short to allow for detection ( $T_2 \ll 1$  ms) using the spin echo technique described throughout this section. Free pool protons however, have long  $T_2$  relaxation times that do not completely decay before all of the necessary spatial encoding gradients are applied and signal acquisition is complete. Therefore using this off resonance RF pulse technique, protons in macromolecules (specifically myelin in this experiment) can be indirectly imaged.

## Two Pool Model of Magnetization Transfer

Figure 2.15 shows an interpretation of the two pool model of magnetization transfer. The free pool protons initially start with magnetization  $M_0^A$  and the bound pool protons start with magnetization  $M_0^B$ . The off resonance pulse selectively excites the bound pool creating an increased amount of transverse magnetization within this pool. The pools relax back to equilibrium with longitudinal relaxation rate  $R_A = 1/T_1^A$  and  $R_B = 1/T_1^B$ . While relaxation is occurring, the pools exchange magnetization. The amount of transfer is dependent on the magnetization transfer rate  $R$ . The exchange of magnetization leaves less longitudinal magnetization at equilibrium in the free pool available to be excited for the  $\pi/2$  on resonance RF pulse thus creating signal attenuation.

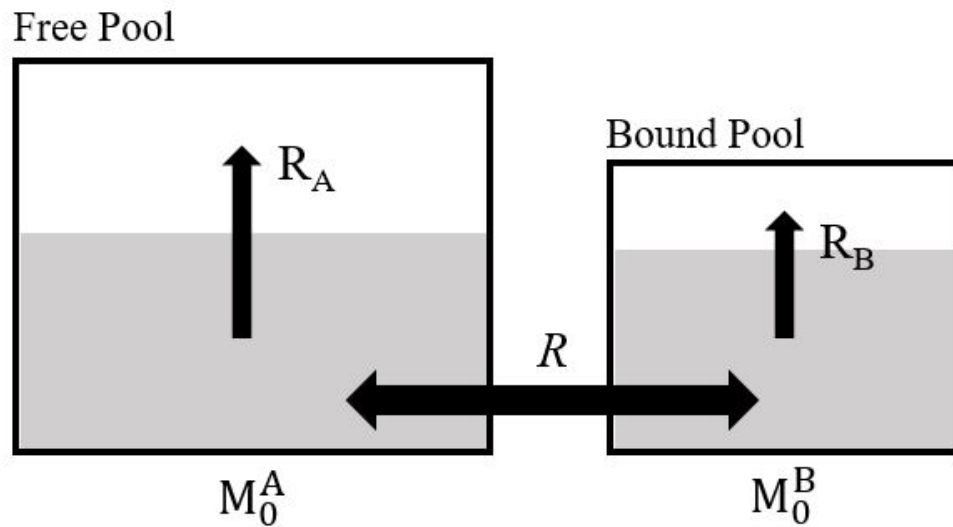


Figure 2.15: Two pool model of magnetization transfer. The free pool protons have magnetization  $M_0^A$  and the bound pool protons have magnetization  $M_0^B$ . Spins have either longitudinal (white) or saturated (grey) magnetization. After RF excitation of the bound pool, magnetization transfer occurs between pools with a rate  $R$ , while each pool relaxes longitudinally with rates  $R_A$  and  $R_B$ .

A proton density image is acquired using a spoiled gradient echo imaging sequence (see Figure 2.16). The spoiled gradient is applied along the slice direction during a gradient echo

imaging sequence to minimize residual transverse magnetization after signal acquisition such that only longitudinal magnetization exists at the time of the subsequent excitation pulse (2; 18). The gradient echo signal amplitude is dependent on  $T_1$  and  $T_2^*$  of the sample as well as the flip angle,  $T_E$  and  $T_R$ . A proton density image with fast acquisition is achieved by minimizing TR and reducing the flip angle to reduce  $T_1$ -weighting, all in combination with the spoiler gradients (2). This is known as the Fast Low Angle Shot (FLASH) method. Applying the off resonance RF pulse before the FLASH method gives an image with magne-

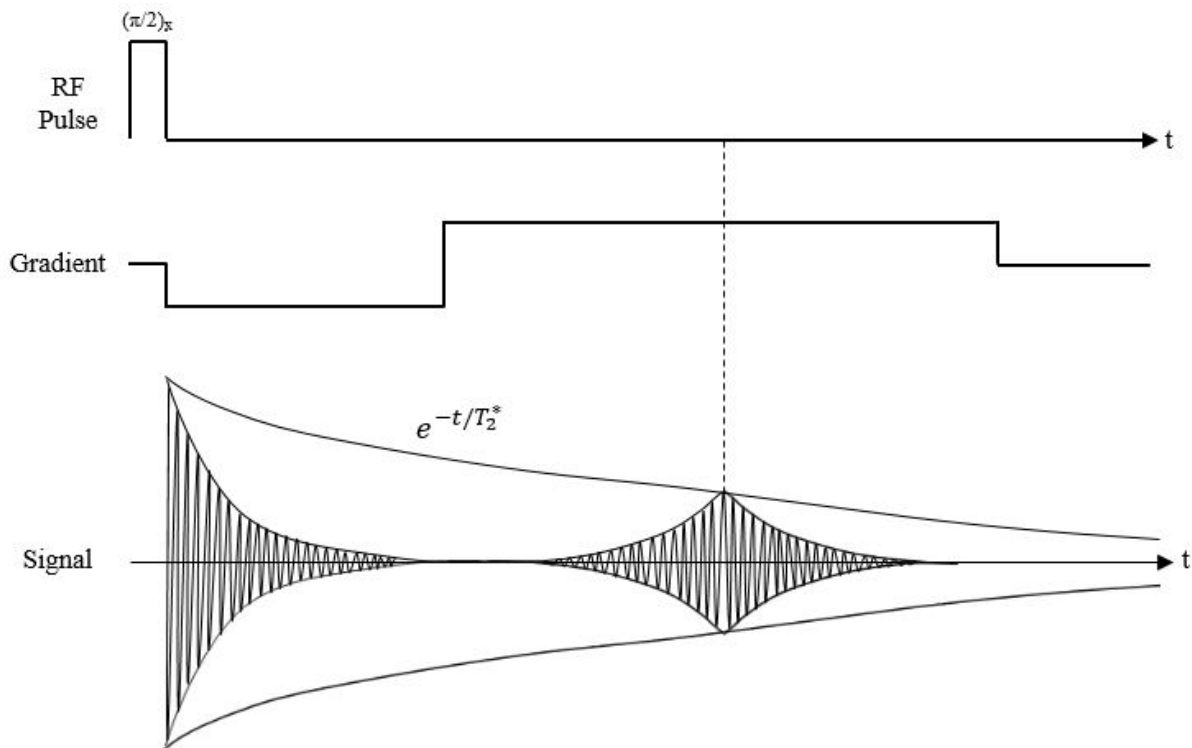


Figure 2.16: The gradient echo pulse sequence. Gradient dephasing and rephrasing creates the echo signal at  $t = T_E$ .

tization transfer contrast proportional to the magnetization transfer properties of the tissue and the imaging parameters (2). The off resonance RF pulse can be characterized by its offset frequency,  $\Delta f$  (in Hz) and the angular frequency it induces in the precession,  $\omega_1$  (rad/s).

The coupled two pool system described above can be represented by differential equa-

tions to produce an equation defining the relationship between the longitudinal magnetization directly after RF excitation in a MT sequence ( $M_z^A$ ) and the longitudinal magnetization directly after RF excitation with no off resonance pulse used ( $M_0^A$ ),

$$\frac{M_z^A}{M_0^A} = g \left( \frac{R_B \left[ \frac{RM_0^A f}{R_A(1-f)} \right] + R_{rfB} + R_B + RM_0^A}{\left[ \frac{RM_0^A f}{R_A(1-f)} \right] (R_B + R_{rfB}) + \left( 1 + \left[ \frac{\omega_1}{2\pi\Delta f} \right]^2 \left[ \frac{1}{R_A T_2^A} \right] \right) (R_B + R_{rfB} + RM_0^A)} \right). \quad (2.34)$$

Above,  $f$  is the bound pool fraction  $f = (M_0^B)/(M_0^A + M_0^B)$ ,  $g$  is a constant related to the gain settings,  $R_{rfA}$  is the absorption rate of the free pool and  $R_{rfB}$  is the absorption rate of the bound pool. This ratio,  $M_z^A/M_0^A$ , represents the normalized signal intensity and is equivalent to the magnetization transfer ratio  $M_{sat}/M_0$  discussed below. The derivation of Equation 2.34 can be found in (2).

The parameters  $R_B$ ,  $RM_0^A$ ,  $f/R_A(1-f)$ ,  $T_2^B$ ,  $1/R_A T_2^A$  and  $g$  can be estimated by collecting a series of images with varying values of  $\Delta f$  and  $\omega_1$  and fitting the signal to Equation 2.34. In this experiment, 1 proton density image was collected contributing  $M_0^A$  along with 18 MTC images with varying  $\Delta f$  and  $\omega_1$ . Equation 2.34 was used to estimate the 6 parameters listed.  $R_B$  was arbitrarily set to  $1 \text{ s}^{-1}$  by convention (2; 19).

## qMTI Metrics

### Longitudinal Relaxation Rates of the Free ( $R_A$ ) and Bound ( $R_B$ ) Pools

$$R = \frac{1}{T_1} \quad (2.35)$$

The relaxation rate depends on characteristics of the molecular environment as well as magnetic field strength. A decrease in lattice coherence or an increase in water mobility will cause the longitudinal relaxation rate to increase in biological tissues (2).

### Transverse Relaxation Times of the Liquid ( $T_2^A$ ) and Bound ( $T_2^B$ ) Pools

$T_2$  measured from magnetization transfer methods reflect the same relaxation mechanisms as  $T_2$  measured from relaxometry methods (2). Spins in the bound pool will dephase faster and have shorter  $T_2$  times than spins in the free pool because of their stationary magnetic field inhomogeneities.

### Magnetization Transfer Rate, $RM_0^A$ (or just $R$ )

The magnetization transfer rate, referred to in this thesis as just  $R$ , is the rate magnetization is transferred from the bound pool to the free pool after an off resonance RF pulse. It is dependent on the size of the pools as well as the surface chemistry of the macromolecule (2; 5).

### Magnetization Transfer Ratio (MTR)

$$MTR = M_0 - M_{sat}/M_0 \quad (2.36)$$

The amount of magnetization transfer detected depends on how fast magnetization is transferred from the bound pool to the free pool which is in competition with how fast the saturated spins are regaining their longitudinal magnetization. Higher  $R$  creates more magnetization transfer therefore causing more signal attenuation and a larger MTR value. Higher  $R_A$  means longitudinal magnetization will be more likely to recover and contribute to the detected signal therefore decreasing MTR values (20).

MTR maps are created using a proton density image ( $M_0$ ) and a single saturation image making acquisition times shorter than collecting a set of qMT images (minimum of 6 in this thesis experiment) which are required to estimate the desired parameters. Thus, MTR maps

provide good contrast between tissues in a short amount of time while qMTI metrics give more specific detail of the 2 pools and their interaction but require more time.

Bound Pool Fraction,  $f$

$$f = M_0^B / (M_0^A + M_0^B) \quad (2.37)$$

The bound pool fraction is a ratio of the macromolecular protons to the total protons (macromolecular and free water).  $f$  is expected to decrease as macromolecules are depleted as is the case in demyelination or with an increase in the free water component (as in edema) (21).

# Chapter 3

## Methods

### 3.1 Mouse Model

Thirty-six 8 week old female C57BL/6 mice (Genetic Models Centre, Winnipeg, Canada) were housed at the University of Manitobas Animal Care facility. Cuprizone (Sigma Aldrich) was mixed with mouse chow (Teklad Global 16% Protein Rodent Diet) to a final concentration of 0.3% (w/w) and pressed into pellets (see Figure 3.1). Mice were classified into two groups: control mice receiving regular mouse chow (n=18 CTL) and those receiving the same mouse chow but with cuprizone mixed in (n=18 CPZ). Cuprizone feeding began immediately after initial *in vivo* images were taken at week 0. The experimental protocol was approved by the University of Manitoba and University of Winnipeg Animal Care Committees who adhere to the guidelines and principles created by the Canadian Council on Animal Care. Table 3.1 gives a representation of the study set up.



Figure 3.1: Cuprizone was mixed with mouse chow to a final concentration of 0.3% (w/w) and pressed into pellets. Blue food coloring was added to the cuprizone chow to avoid confusion with the control normal mouse chow.

## 3.2 *In vivo* MRI

MRI was performed on a 7T 21 cm Bruker Avance III MRI System (pictured in Figure 3.2) with Paravision 5.0 (Bruker BioSpin). Both groups were imaged prior to the start of the cuprizone feeding (week 0) and every week thereafter for 6 weeks where maximum demyelination in the corpus callosum is reached. Six mice (n=3 CPZ, n=3 CTL) were imaged per day of week 0 for 6 days such that all 36 mice were imaged. Beginning week 1 after *in vivo* imaging, 3 CPZ mice and 3 CTL mice, one mouse per day, were euthanized to perform *ex vivo* analysis.

Mice were anesthetized using 5% isoflurane in O<sub>2</sub>/N<sub>2</sub>O and maintained at approximately

Table 3.1: Schematic representation of the study setup. The 'Live Mice' column represents the number of live mice in each group at the beginning of each week. This is the number of mice that underwent *in vivo* imaging that week. The 'Mice Sacrificed' column represents the number of mice from each group sacrificed that week. These mice underwent *ex vivo* imaging immediately after sacrifice. Cuprizone feeding began immediately after week 0 *in vivo* imaging.

Week	Live Mice		Mice Sacrificed	
	CTL	CPZ	CTL	CPZ
0	18	18	0	0
1	18	18	3	3
2	15	15	3	3
3	12	12	3	3
4	9	9	3	3
5	6	6	3	3
6	3	3	3	3

1.5% isoflurane in O<sub>2</sub>/N<sub>2</sub>O with a nose cone during imaging. A gas scavenging system was used to collect excess isoflurane. Respiration and external body temperature were monitored during imaging using a MR-compatible small animal monitoring system (SA Instruments, Stony Brook, NY, USA). External body temperature was maintained at 37°C with a heating circular bath pad.

A custom built 42 mm diameter, 300 MHz inductively coupled quadrature RF volume coil (NRC Institute for Bio-diagnostics, Winnipeg, MB, Canada) containing a tooth bar secured the head in place during imaging. The bed containing the monitoring systems, heating pad and coil were placed inside a Bruker BGA12-S actively shielded gradient system with integrated shim coils (Bruker BioSpin).

MRI setup was completed in the following order:

1. Initial pilot scan to ensure proper placement of the mouse.
2. RF coil tuning and matching to the mouse head.



Figure 3.2: The 7T 21 cm Bruker Avance III MRI System used to collect *in vivo* and *ex vivo* images.

3. Magnetic field inside the coil made homogenous by manually adjusting the 1st and 2nd order gradients (shimming). After automatic shimming, a  $B_0$  field map acquired and the shimming gradients re-calculated using Brukers MapShim function to improve shimming.
4. The Larmor frequency,  $\omega_0$ , found at peak signal strength.
5. Appropriate RF attenuation determined for creating  $\pi/2$  and  $\pi$  pulses.
6. Receiver gain adjusted dependent on pulse sequence used.
7. Axial, coronal, sagittal scout scans performed to consistently orient the desired coronal slice relative to the centre line of the brain.
8. Based on a high resolution  $T_2$ -weighted sagittal image (Figure 3.3) along the centre line of the brain, a coronal slice was centered on the anterior commissure and moved 0.5 mm anteriorly while intersecting the rostral region of the corpus callosum. A second slice was positioned perpendicular to the corpus callosum and intersected the region of corpus callosum that was contained in the first slice. The first slice was then deleted

and the second was the desired slice. This procedure allowed consistent slice placement from mouse to mouse, week to week and reduced partial volume averaging effects in the corpus callosum.

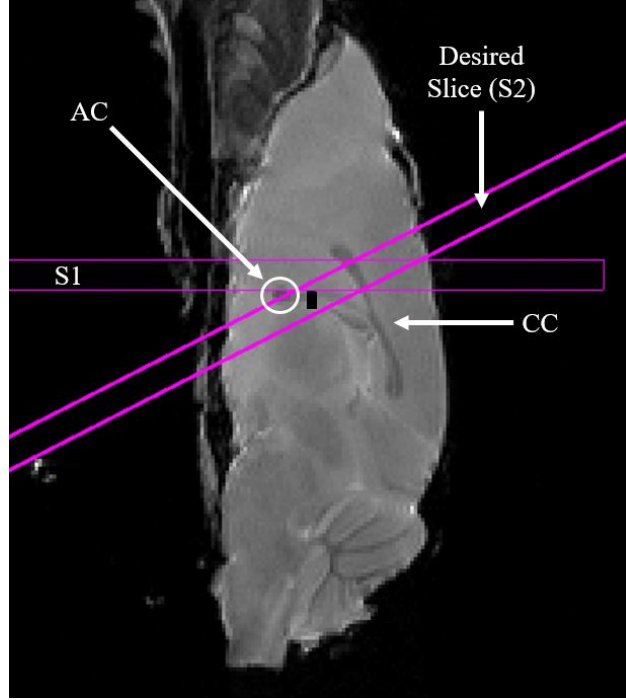


Figure 3.3: The high resolution  $T_2$ -weighted sagittal image used to select the desired coronal slice. A first coronal slice (S1) was centered on the anterior commissure (AC) and moved 0.5 mm anteriorly. A second slice (S2) was positioned perpendicular to the corpus callosum (CC) and intersected the region of corpus callosum that was contained in the first slice. The first slice was then deleted and the second was the desired slice.

$T_2$ -weighted images and MT images were acquired with the same coronal slice with  $98 \times 98 \times 750 \mu m^3$  resolution. Field of view (FOV)/matrix size was  $(2.5cm)^2/256 \times 256$  resulting in a  $98 \times 98 \times 750 \mu m^3$  voxel resolution.

*In vivo*  $T_2$ -weighted images were acquired using a Rapid Acquisition with Relaxation Enhancement (RARE) sequence (22) with fat suppression. The parameters of the sequence were effective echo time ( $T_{Eff}$ ) = 80 ms, a repetition time ( $T_R$ ) = 1640 ms, 12 averages, RARE factor = 8, echo spacing = 20 ms and a 10 minute acquisition time.

To create magnetization transfer ratio (MTR) maps, two *in vivo* Fast Low Angle Shot

(FLASH) (23) images were acquired: one with a magnetization transfer saturation pulse (Gaussian shaped, 10.25 ms long with a 10  $\mu$ T saturation amplitude and a frequency offset of 6 kHz) and one without (Proton Density (PD) image). The remaining parameters for these images were using a  $T_E = 6$  ms,  $T_R = 70$  ms, 48 averages, 10 degree flip angle and a 2x14 minute acquisition time.

### 3.3 *Ex vivo* MRI

Beginning week 1 after *in vivo* imaging, 6 mice (n = 3 CPZ, n= 3 CPZ) were euthanized, one mouse per day, to perform *ex vivo* analysis. This schedule allowed the analysis of the cuprizone damage progression in 3 treatment mice at each week. Under deep anesthetic, intracardial injections of 10 mL of cold 0.1 M phosphate buffered saline (PBS) followed by 0.5% glutaraldehyde and 2% paraformaldehyde (PFA) were performed to fix the brain. These were followed by another 10 mL of cold 0.1 M PBS injection to flush out the remaining fixative. The skull was removed from the body and the skin and tissue were removed from around the skull before storing in PBS prior to *ex vivo* imaging. Skulls were secured in place for imaging using a custom built acrylic brain holder filled with room temperature Fomblin Perfluoropolyethwe Y04 grade fluid (Solvay Solexis) to eliminate external proton signal and susceptibility artifacts (2). The magnet bore remained at a constant temperature of 18°C during overnight imaging. After imaging, skulls were dried of excess Fomblin and rinsed in PBS. Brains were removed from the skull and stored in a 2% glutaraldehyde and 2% PFA solution in a fridge for electron microscopy.

*Ex vivo* images acquired included  $T_2$ -weighted,  $T_1$  and  $T_2$  relaxometry, MTI and DTI. All images were acquired with the same coronal slice with 98x98x750  $\mu m^3$  resolution. Field of view (FOV)/matrix size was (1.25cm)<sup>2</sup>/128x128 resulting in a 98x98x750  $\mu m^3$  voxel resolution. One CTL mouse was acquired with 2 additional slices which were not used in the

analysis. High resolution *ex vivo*  $T_2$ -weighted images were acquired using the RARE sequence with fat suppression. The parameters of the sequence were

$T_{Eff} = 46$  ms,  $T_R = 1640$  ms, 4 averages, RARE factor = 4, echo spacing = 23 ms and a 7 minute acquisition time.

Combined  $T_1$  and  $T_2$  relaxometry data was acquired using a series of RARE acquisitions with  $T_{Eff} = 11, 33, 55, 77, 99$  ms,  $T_R = 5, 3, 1.5, 0.8, 0.4, 0.2$ s, RARE factor = 2, 8 averages and an acquisition time of 71 minutes. The CTL mouse images acquired with 3 slices used  $T_R = 5, 3, 1.5, 0.8, 0.4, 0.356$ s due to slight difference in image protocol. Additional multicomponent  $T_2$  relaxometry maps were acquired using a Multi-Slice Multi-Echo (MSME) sequence with 32 slice selective pi pulses and a 10 ms echo spacing ( $T_E = 10, 20, 30, 320$  ms,  $T_R = 2500$  ms, 24 averages and a 96 minute acquisition time).

MT images were collected using the same FLASH sequence as *in vivo* with 18 MT saturation pulse images acquired with RF amplitudes of 5, 10, and  $20\mu$ T and frequency offsets at each power of 1, 2, 4, 6, 10, and 30 kHz (64 averages and an acquisition time of 19x9.6 min) and 1 with no saturation pulse (PD image).

DT images were collected with a Pulsed Gradient Spin Echo sequence (PGSE) (24) using a 7 direction tetra-orthogonal gradient-encoding scheme and b-value= $1000$  s/mm<sup>2</sup> ( $\delta = 6$  ms,  $\Delta = 14$  ms), 6 averages  $T_E = 26$  ms,  $T_R = 5000$  ms, and a 5 hour acquisition time.

### 3.4 Preprocessing and Image Analysis

In order to fit a series of images to the equations found in chapter 2, to define consistent regions of interest (ROIs) across images of the same mouse and to compare different MR

metric values on a voxel-by-voxel basis, image registration was required.

*In vivo* T<sub>2</sub>-weighted images and MT images with no saturation pulse (PD) were aligned to MT saturation images using an affine transformation matrix determined by minimizing the 2D correlation coefficient and/or mutual information of the two images, with manual adjustments if needed, using a custom built MATLAB GUI (2). T<sub>2</sub>-weighted images were normalized to the mean CSF signal in the third ventricle. MTR images were calculated by finding the difference between the PD and MT saturation image and dividing by the PD on a pixel by pixel basis.

*Ex vivo* PD, MT saturation, and T<sub>1</sub>/T<sub>2</sub> relaxometry images were aligned to the low b-value diffusion weighted image using the same method and GUI as the *in vivo* images. Diffusion weighted images required that the b-matrices of each image were rotated to reflect the rotations from image registration to maintain accurate orientation information (2; 25).

MRI metric maps from each imaging method were calculated using custom MATLAB scripts. Images were first filtered using an adapted anisotropic diffusion filter (26; 27) as done previously (2).

After images were registered and filtered, MATLAB scripts were developed to calculate metric maps from each MRI method and were calculated using equations found in chapter 2. ROIs were defined for each mouse on *in vivo* normalized T<sub>2</sub>-weighted signal intensity images and applied to the remaining *in vivo* images while *ex vivo* ROIs were defined on the diffusion derived RGB maps and then applied to the remaining *ex vivo* images. These ROIs included the corpus callosum, the left and right external capsule, the left and right cerebral cortex, and the whole brain as shown in Figure 3.4.

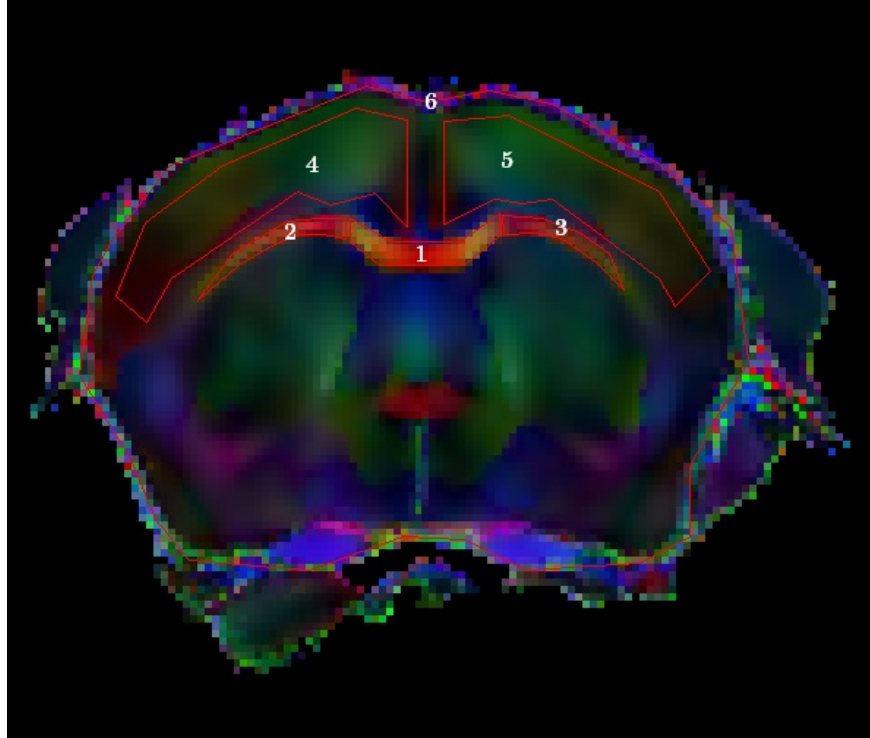


Figure 3.4: *Ex vivo* ROIs included the corpus callosum (1), the left (2) and right (3) external capsule, the left (4) and right (5) cerebral cortex and the whole brain (6).

### 3.5 Electron Microscopy (EM)

Brain tissue was fixed in 2% glutaraldehyde and 2% PFA solution for a minimum of 7 months. Five mice at week 2 of the study (n=2 CTL, n=3 CPZ) and 6 mice at week 3 of the study (n=3 CTL, n=3 CPZ) were selected for EM. *In vivo* normalized T<sub>2</sub>-weighted signal intensity values in the corpus callosum of cuprizone fed mice were found to experience the first and largest statistically significant increase between weeks 2 and 3 of feeding the cuprizone chow (further explained in section 4.2). Based on this, brains from these weeks were chosen for EM. An approximately 1 mm thick slice was removed corresponding to the coronal slice imaged through MRI (see Figure 3.5). The corpus callosum was carefully cut from this slice using a dissecting microscope as shown in Figure 3.6. Rectangular cubes of corpus callosum were further fixed in phosphate buffered 4% glutaraldehyde followed by 1% osmium tetroxide overnight, dehydrated in alcohol then acetone, and embedded in Epon

resin. Semithin sections ( $1\ \mu\text{m}$ ) were stained with toluidine blue. Ultrathin sections ( $90\ \text{nm}$ ) from the corpus callosum were contrasted with uranyl acetate and lead citrate then viewed and photographed with a JEOL 1010 transmission electron microscope equipped with digital camera. An experienced neuropathologist took representative photomicrographs. EM images at 2000, 5000, and 15 000x magnification were taken.



Figure 3.5: The first cut made in the dissection of the same slice of the mouse brain imaged using MRI. To find the position of the slice in the actual brain tissue, a mouse brain (out of the skull) and a sagittal MR image that was taken during the current study (similar to that in Figure 3.3) were used to determine the image scale. On the MR image, the distance of the left side of the slice from the edge of the olfactory bulb was measured. Using this distance and the scale of the MR image, the distance the first (slightly angled) cut from the left side of the actual brain (side with the olfactory bulb) was determined to be 2mm. The 1mm slice was then taken from the tissue remaining on the right side.

EM metrics were found by placing a  $2 \times 2\ \mu\text{m}$  grid over 2 of the 5000x magnification EM images from each of the mice. Tissue at each intersection (208 points per image, 416 points per mouse) was classified into 1 of 4 groups: myelinated axons, myelin sheath, non-myelinated cells (including unmyelinated and demyelinated material, glial cells and processes,



Figure 3.6: Once the slice was removed from the whole brain, the corpus callosum was dissected out of the slice and was sent for EM imaging. The remaining slice, with a hole where the corpus callosum once was, is pictured above.

and apoptotic cells), and extracellular space. The fraction of each was calculated per mouse. Axon diameters and myelin sheath thickness were measured on two 15,000x magnification EM images. The g-ratio, myelinated axons per  $100 \mu\text{m}^2$ , and myelin/axon diameter ratio was calculated using these values as was done previously (2; 19).

### 3.6 Statistical Analysis

Independent sample t tests were performed at each week between groups for normalized  $T_2$ -weighted signal intensities, MTR values, and *ex vivo* imaging metrics in the CC and EC. One-way ANOVA with Tukey's *post hoc* test was also used to find significant week to week

differences within groups for all *in vivo* and *ex vivo* metrics in the CC and EC.

A Mixed Models procedure was performed on *in vivo* normalized T<sub>2</sub>-weighted signal intensities and MTR values with week serving as the within-subject effect and group as the between subject effect (treated as a continuous variable). The Mixed Model procedure allows the within-subject factor to be treated as continuous and handles missing data more desirably than two-way repeated measures ANOVA (28).

Spearman rank correlation coefficients and Pearson correlation coefficients were calculated between *in vivo* metrics and between all *ex vivo* metrics using mean ROI values and individual voxel values in the CC and EC of control mice, cuprizone mice and the combined control and cuprizone datasets. Metric values from control mice from week 1 (n=1) and week 4 (n=1) were excluded from the correlation due to ROIs having a different number of pixels from defining them on different images.

Independent sample t tests were performed on cellular features found through EM examination between groups at weeks 2 and 3 and within groups comparing week 2 to week 3. Spearman correlation coefficients were also performed between MRI metric mean ROI values and cellular features.

# Chapter 4

## Results

### 4.1 Cuprizone Diet

The 0.3% (w/w) cuprizone diet did not cause the mice to display any signs of pain or distress nor did it cause death. As shown in Figure 4.1, the cuprizone fed mice weighed significantly less beginning week 1 and throughout the remainder of feeding when compared to control mice. The largest difference in weight between groups occurred at week 6 where control mice weighed an average  $24 \pm 2$  g compared to cuprizone fed mice weighing an average of  $20 \pm 1$  g. Cuprizone fed mice lost a maximum of 5.4% after the second week of feeding. The majority of mice then began gradual weight gain, while the remaining began gradual weight gain the following week.

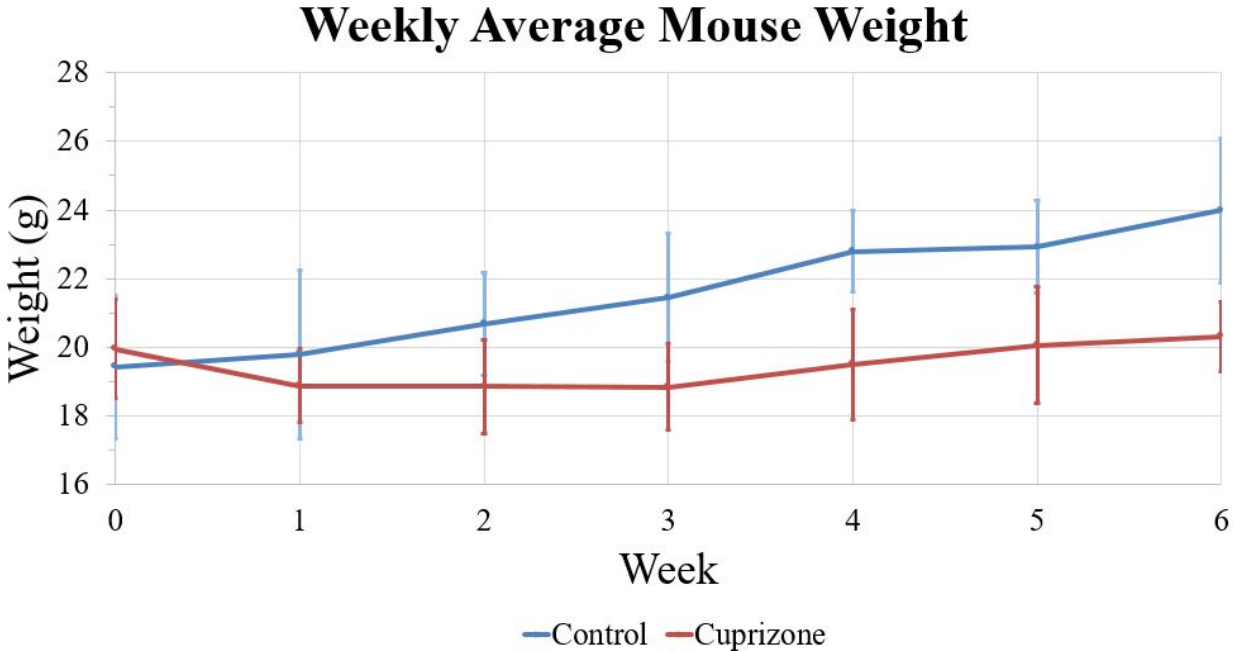


Figure 4.1: Weekly average mouse weight for control (blue) and cuprizone-fed (red) mice. Values are reported as mean  $\pm$  standard deviation. [Week 0: n=18 per group, Week 1: n=18 per group, Week 2: n=15 per group, Week 3: n= 12 per group, Week 4: n= 9 per group, Week 5: n= 6 per group, Week 6: n= 3 per group].

## 4.2 *In vivo* MRI

Visual inspection of Figure 4.2 and Figure 4.3 indicate that both methods are sensitive to changes caused by the cuprizone treatment and that these MR metrics follow different time lines. Normalized  $T_2$ -weighted images detected changes as early as week 2 while MTR maps detected changes at week 4. The normalized  $T_2$ -weighted signal increased before plateauing at week 3 in the corpus callosum whereas MTR values experienced decreases before plateauing at week 4. Normalized  $T_2$ -weighted signal intensity was significantly different between controls and cuprizone mice starting at week 1 in both the corpus callosum and external capsule whereas the MTR values between control and cuprizone fed mice in the corpus callosum were significantly different at week 2, not significantly different at week 3 and became substantially significantly different beginning week 4.

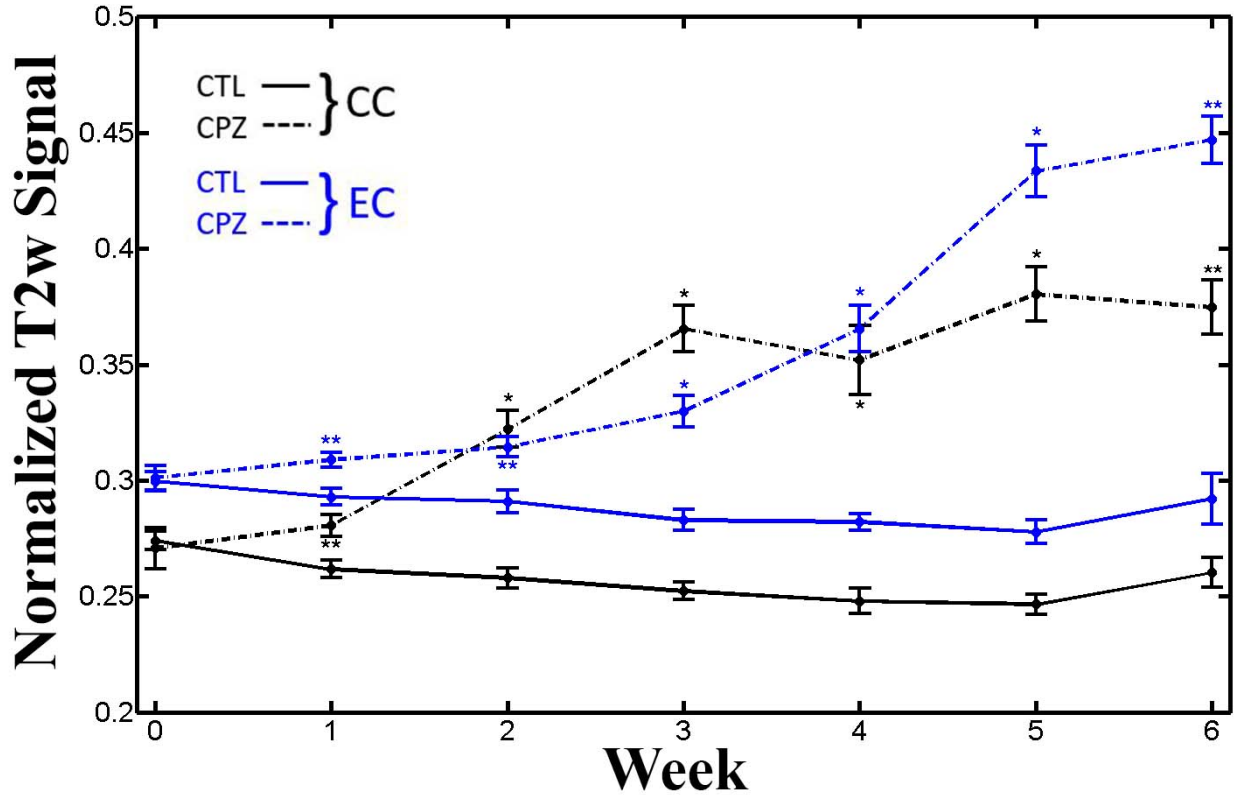


Figure 4.2: Weekly normalized  $T_2$ -weighted ( $T_2w$ ) signal intensity changes (mean  $\pm$  SEM) in the corpus callosum (CC, black) and external capsule (EC, blue) in cuprizone fed (dotted) and control (solid) mice. [Week 0:  $n=16(\text{CTL})/11(\text{CPZ})$ , Week 1:  $n=17(\text{CTL})/18(\text{CPZ})$ , Week 2:  $n=12(\text{CTL})/15(\text{CPZ})$ , Week 3:  $n=11(\text{CTL})/11(\text{CPZ})$ , Week 4:  $n=9(\text{CTL})/9(\text{CPZ})$ , Week 5:  $n=6(\text{CTL})/6(\text{CPZ})$ , Week 6:  $n=3(\text{CTL})/3(\text{CPZ})$ ]. Data from weeks excluded due to high noise. (\*) denote significant differences between groups at that week with  $*p < 0.05$ ,  $**p < 0.01$ ,  $***p < 0.0001$ . All data shown for the corpus callosum in Figure B.1.

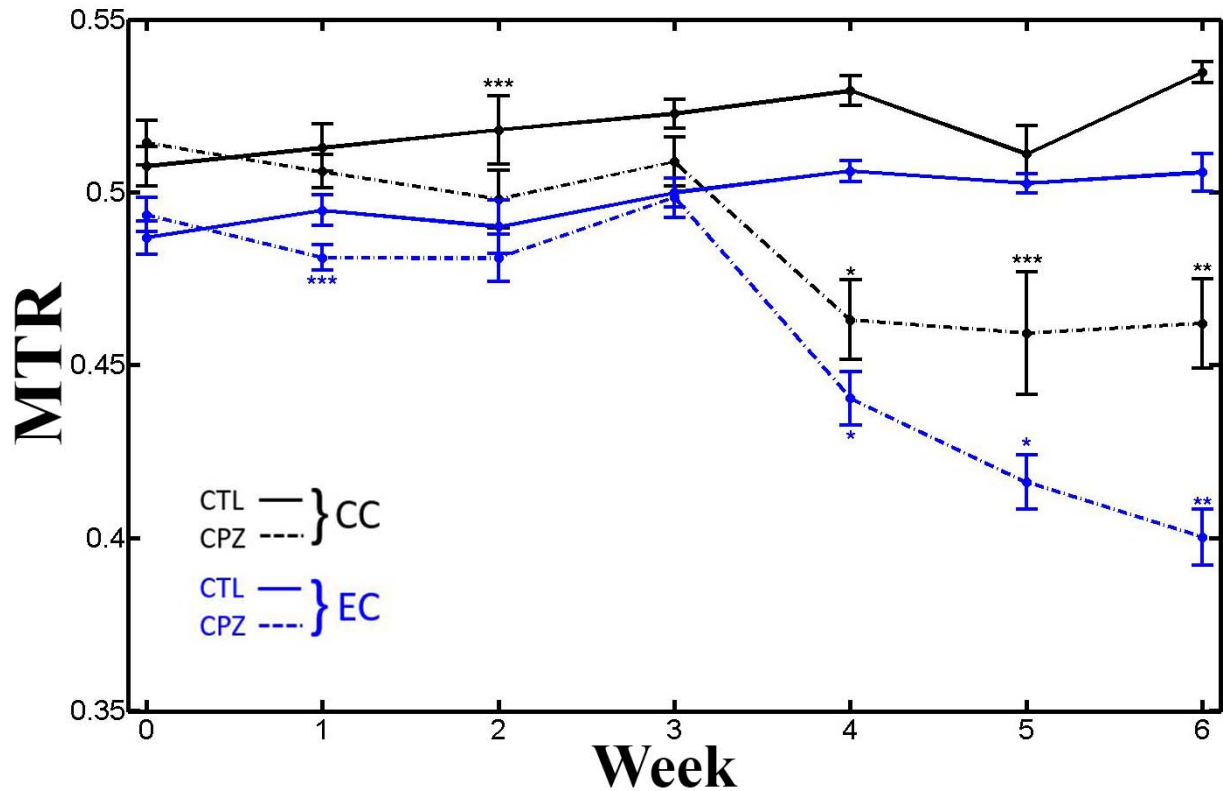


Figure 4.3: Weekly MTR changes (mean  $\pm$  SEM) in the corpus callosum (CC,black) and external capsule (EC,blue) in cuprizone fed (dotted) and control (solid) mice. [Week 0: n=16(CTL)/11(CPZ), Week 1: n=17(CTL)/18(CPZ), Week 2: n=12(CTL)/15(CPZ), Week 3: n=11(CTL)/11(CPZ), Week 4: n=9(CTL)/9(CPZ), Week 5: n=6(CTL)/6(CPZ), Week 6: n=3(CTL)/3(CPZ)]. Data from weeks excluded due to high noise. (\*) denote significant differences between groups at that week with  $*p < 0.05$ ,  $**p < 0.01$ ,  $***p < 0.0001$ . All data shown for the corpus callosum in Figure B.2.

Table 4.1: Weekly *in vivo* normalized  $T_2$  weighted signal ( $T_{2w}$ ) and MTR and *ex vivo* relaxometry MRI metrics in the corpus callosum of control (CTL) and cuprizone (CPZ) mice. Values are reported as mean (SEM). *In vivo* values have measurements as follows: [n=16 CTL, n=11 CPZ] at week 0, [n=17 CTL, n=18 CPZ] at week 1, [n=12 CTL, n=15 CPZ] at week 2, [n=11 per group] at week 3, [n=9 per group] at week 4, [n=6 per group] at week 5, [n=3 per group] at week 6. *Ex vivo* measurements contain n = 3 per group at each week (except for week 4 where n=2 CTL). \* denotes significant differences between groups. \* $p < 0.05$ , \*\* $p < 0.01$ , \*\*\* $p < 0.0001$ .

Week	Mouse	Method			
		<i>In vivo</i>		<i>ex vivo</i> Relaxometry	
		$T_{2w}$	MTR	$T_1$ (s)	$T_2$ (ms)
0	CTL	0.274 (0.004)	0.508 (0.006)	-	-
	CPZ	0.271 (0.009)	0.514 (0.007)	-	-
1	CTL	0.262 (0.003)	0.514 (0.007)	1.43 (0.01)	52 (2)
	CPZ	0.281* (0.005)	0.506 (0.005)	1.38* (0.01)	46 (1)
2	CTL	0.257 (0.005)	0.527 (0.004)	1.43 (0.02)	52 (1)
	CPZ	0.322*** (0.008)	0.498** (0.008)	1.40 (0.01)	50.7 (0.4)
3	CTL	0.252 (0.004)	0.523 (0.004)	1.41 (0.02)	49 (1)
	CPZ	0.37*** (0.01)	0.509 (0.007)	1.46 (0.02)	55 (2)
4	CTL	0.247 (0.005)	0.531 (0.004)	1.41 (0.03)	49 (1)
	CPZ	0.35*** (0.02)	0.47*** (0.01)	1.43 (0.02)	50.6 (0.4)
5	CTL	0.247 (0.004)	0.511 (0.008)	1.39 (0.01)	50 (1)
	CPZ	0.38*** (0.01)	0.46* (0.02)	1.51 (0.02)*	54 (1)
6	CTL	0.260 (0.006)	0.535 (0.003)	1.36 (0.05)	53 (2)
	CPZ	0.37*** (0.01)	0.46** (0.02)	1.514 (0.002)*	53 (3)

Normalized  $T_2$ -weighted signal images (Figure 4.4) show signal increase in the corpus callosum of the cuprizone fed mice beginning as early as week 2 of feeding. Signal increase in the external capsule appears to lag signal increase in the corpus callosum although complete signal inversion compared to the surrounding tissue is apparent at week 6 of the study in external capsule where it is not in the corpus callosum. Numerical normalized  $T_2$ -weighted signal intensity values and MTR values can be found in Table 4.1.

Weekly changes (mean  $\pm$  SEM) in the normalized  $T_2$ -weighted signal in the corpus

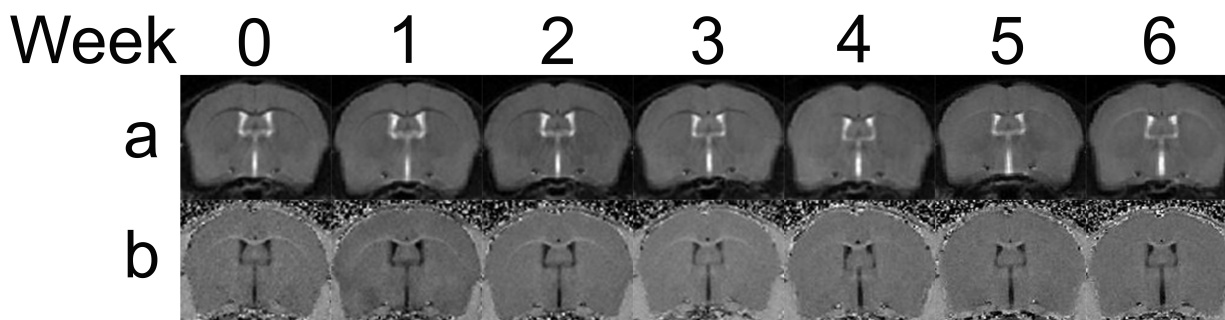


Figure 4.4: Weekly (a) normalized  $T_2$ -weighted signal intensity images and (b) MTR maps for a cuprizone mouse.

callosum and external capsule in cuprizone fed (dotted) and control (solid) mice are shown in Figure 4.2. Independent sample t tests verified differences in normalized  $T_2$ -weighted signal intensities between control and cuprizone fed mice in the corpus callosum and external capsule were both significantly different beginning week 1 ( $p < .01$  for both). One-way ANOVA confirmed significant week to week normalized  $T_2$ -weighted signal changes occurred in the cuprizone fed corpus callosum and external capsule ( $p < .0001$  for both). Comparisons using Tukeys *post hoc* test indicated the largest significant week to week change in the normalized  $T_2$ -weighted signal of the external capsule of the cuprizone fed mice occurred between weeks 4 and 5 whereas it occurred between weeks 2 and 3 in the corpus callosum. No significant week to week changes occurred after week 3 in the corpus callosum of the cuprizone fed mice whereas significant week to week changes ceased at week 5 in the external capsule. Mixed Models analysis showed significant differences in the normalized  $T_2$ -weighted signal intensity of the corpus callosum between the control and cuprizone groups ( $p < .0001$ ). Significant weekly changes and significant interaction between week and treatment were also apparent ( $p < .0001$  for both).

While the pathological changes due to cuprizone feeding cause an increase in normalized  $T_2$ -weighted signal intensity, they cause a decrease in the MTR. Decreased MTR was

observed in the white matter regions of the cuprizone fed mice compared to control mice as shown in Figure 4.3. Similar to normalized  $T_2$ -weighted signal results, MTR values in the external capsule appear to experience the most change in response to the cuprizone treatment. Independent sample T tests verified differences in MTR between control and cuprizone fed mice in the corpus callosum were significantly different beginning at week 2 ( $p < .01$ ), excluding week 3. Independent sample T tests also indicated differences in MTR between control and cuprizone fed mice in the external capsule were only marginally significantly different at week 2 ( $p < .05$ ) and became substantially significantly different beginning week 4 ( $p < .0001$  for all).

One-way ANOVA confirmed significant week to week changes occurred in the cuprizone fed corpus callosum and external capsule ( $p < .0001$  for both). Comparisons using Tukeys *post hoc* test indicated the largest significant week to week change in both the corpus callosum and external capsule of the cuprizone fed mice occurred between weeks 3 and 4. Week to week changes were not significant after week 4. Mixed Models analysis showed significant differences in MTR values of the corpus callosum between the control and cuprizone groups ( $p < .0001$ ). Significant weekly changes ( $p < .01$ ) and significant interaction between week and treatment were also apparent ( $p < .0001$ ).

### **4.3 *In vivo* normalized $T_2$ -weighted signal and MTR correlations**

Weekly normalized  $T_2$ -weighted signal intensity and MTR weekly voxel based Spearman correlation coefficients for the corpus callosum and external capsule are shown in Table 4.2 for the control, cuprizone and combined mice (control and cuprizone) data sets. Weekly ROI based correlation showed strong but insignificant relationships. Correlations are stronger in

Table 4.2: Normalized T<sub>2</sub>-weighted signal intensity and MTR weekly voxel based Spearman correlation coefficients ( $\rho$ ) for the corpus callosum (CC) and external capsule (EC) for the control, cuprizone fed and combined mice (control and cuprizone) data sets. All coefficients have  $***p < .0001$ .

Week	Control		Cuprizone		Combined	
	CC	EC	CC	EC	CC	EC
0	-0.37	-0.46	-0.37	-0.54	-0.37	-0.49
1	-0.48	-0.59	-0.45	-0.54	-0.47	-0.58
2	-0.44	-0.64	-0.45	-0.52	-0.51	-0.60
3	-0.43	-0.71	-0.49	-0.56	-0.43	-0.55
4	-0.53	-0.73	-0.60	-0.45	-0.76	-0.80
5	-0.34	-0.57	-0.70	-0.49	-0.65	-0.84
6	-0.33	-0.66	-0.37	-0.40	-0.65	-0.85

the external capsule than in the corpus callosum at nearly all weeks in the control, cuprizone and combined control and cuprizone mice data sets with the strongest correlation occurring in the external capsule at week 6 in the combined data set ( $\rho=-0.85$ ,  $p<.0001$ ). The strongest correlation in the corpus callosum of the combined data set occurred at week 4 ( $\rho=-0.77$ ,  $p<.0001$ ). The combined data set was analyzed to include measurements with varying degrees of myelination at each week of the study to improve the power of correlations.

The combined data set of all weeks for control, cuprizone and the combined control and cuprizone mice data sets ROI based Spearman correlation coefficients showed weaker negative correlations than the voxel based analysis which were still statistically significant (Table 4.3). This analysis showed the strongest correlation in the external capsule of the cuprizone fed mice using the voxel based values ( $\rho=-0.69$ ,  $p<.0001$ ). The combined data set corpus callosum gave a coefficient of  $\rho=-0.52$  ( $p<.0001$ ).

Table 4.3: Normalized  $T_2$ -weighted signal intensity and MTR combined week voxel-based and ROI-based Spearman correlation coefficients ( $\rho$ ) for the corpus callosum (CC) and external capsule (EC) for the control, cuprizone fed and combined mice (control and cuprizone) data sets. All coefficients have  $***p < .0001$ .

Week	Control		Cuprizone		Combined	
	CC	EC	CC	EC	CC	EC
Voxel-based	-0.44	-0.61	-0.50	-0.70	-0.52	-0.68
ROI-based	-0.41	-0.23	-0.54	-0.55	-0.57	-0.51

## 4.4 *Ex vivo* MRI

### 4.4.1 Relaxometry

#### $T_1$ Measurements

Visual inspection of Figure 4.5 shows an overall increase in  $T_1$  as changes from the cuprizone feeding progressed in the corpus callosum and external capsule of the cuprizone fed mice.

Independent sample t tests indicated  $T_1$  values were significantly smaller at week 1 ( $p=.05$ ) in the corpus callosum of the cuprizone fed mice compared to control mice. At weeks 5 and 6 of feeding,  $T_1$  values were significantly larger ( $p<.05$  and  $p=.05$ , respectively) in the corpus callosum of cuprizone fed mice compared to control mice. One-way ANOVA and Tukeys *post hoc* tests indicated  $T_1$  values in the corpus callosum of cuprizone fed mice were significantly larger at weeks 5 and 6 than weeks 1 and 2 ( $p<.01$ ).

Independent sample t tests indicated  $T_1$  values were significantly larger in the external capsule of cuprizone fed mice when compared to control mice at week 5 ( $p<.01$ ) and week 6 ( $p<.05$ ).  $T_1$  values from the first 3 weeks of feeding were significantly smaller than values

from weeks 5 and 6 in the external capsule of cuprizone fed mice while week 4 was only significantly different from week 6 ( $p < .0001$  for all).

$T_1$  values from a control mouse at week 4 were excluded from the analysis. It is suspected magnetization transfer effects from acquiring 3 slices caused a significant increase in  $T_1$  values. Slices were acquired in the following order: 1, 3, 2 with slice 3 being the slice of interest. The RF pulse used to select these slices is not a perfect rectangular pulse (in the frequency domain). Instead, it takes on a Gaussian shape. If the slices are close together, the edges of the Gaussian RF pulse overlap with the adjacent slices and cross talk occurs. The frequencies at the edge of the RF pulse from slice 1 will excite bound pool protons (with a frequency approximately 500 to 2500 Hz away from the bulk protons) in slice 3. This means the bound pool protons will lose all of their longitudinal magnetization and will gain transverse magnetization. However, the bound pool and free pool exchange magnetization causing a net transfer of longitudinal magnetization from the free pool to the bound pool. When a  $\pi$  pulse is sent to slice 3 which is meant to decrease the longitudinal magnetization of the free pool (ideally) to zero, it instead decreases to a value below zero. Thus the time it takes the free pool to recover its full longitudinal magnetization increases and therefore so does  $T_1$ . Additionally, free protons in slice 3 may be unintentionally but directly excited due to cross talk. This would prematurely decrease the longitudinal magnetization of the free pool and a similar result described above would occur after the  $\pi$  pulse is applied.

## **$T_2$ Measurements**

$T_2$  values tended to fluctuate throughout the study in the corpus callosum and external capsule of the cuprizone fed mice and had large standard deviations (Figure 4.6). No comparisons between groups were significant.

There was no clear trend in  $T_2$  values in the cuprizone fed mice throughout the weeks

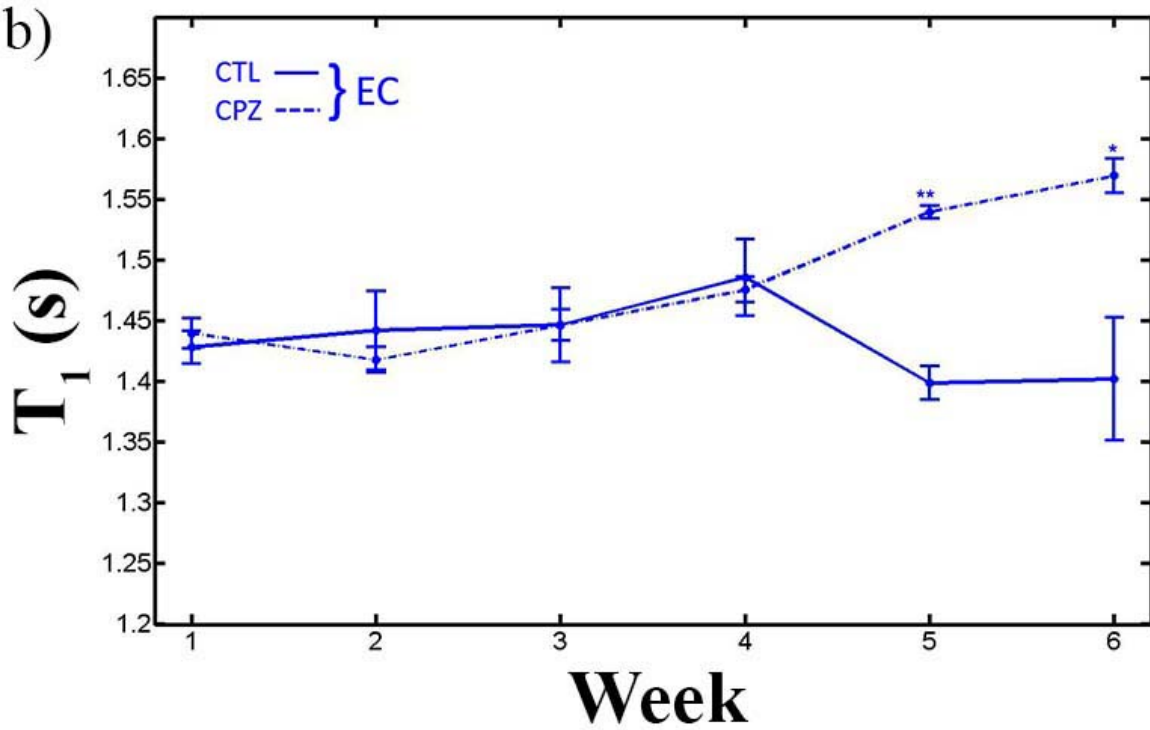
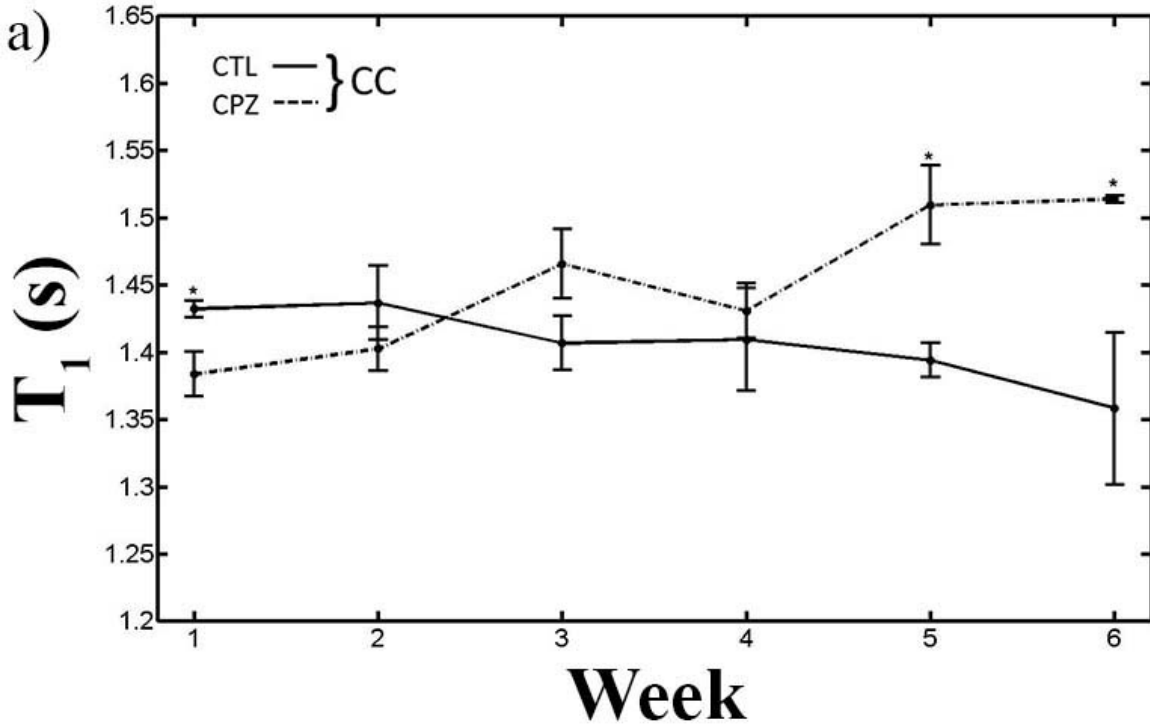


Figure 4.5: (a)  $T_1$  (s) vs week in the corpus callosum of control (solid) and cuprizone fed (dotted) mice. (b)  $T_1$  (s) vs week in the external capsule of control (solid) and cuprizone fed (dotted) mice. Each group mean at each week contains  $n=3$  measurements excluding CTL week 4 where  $n=2$  due to suspected cross talk effects. \* denotes significant differences between groups. \* $p < 0.05$ , \*\* $p < 0.01$ , \*\*\* $p < 0.0001$ . All data shown for the corpus callosum in Figure B.3.

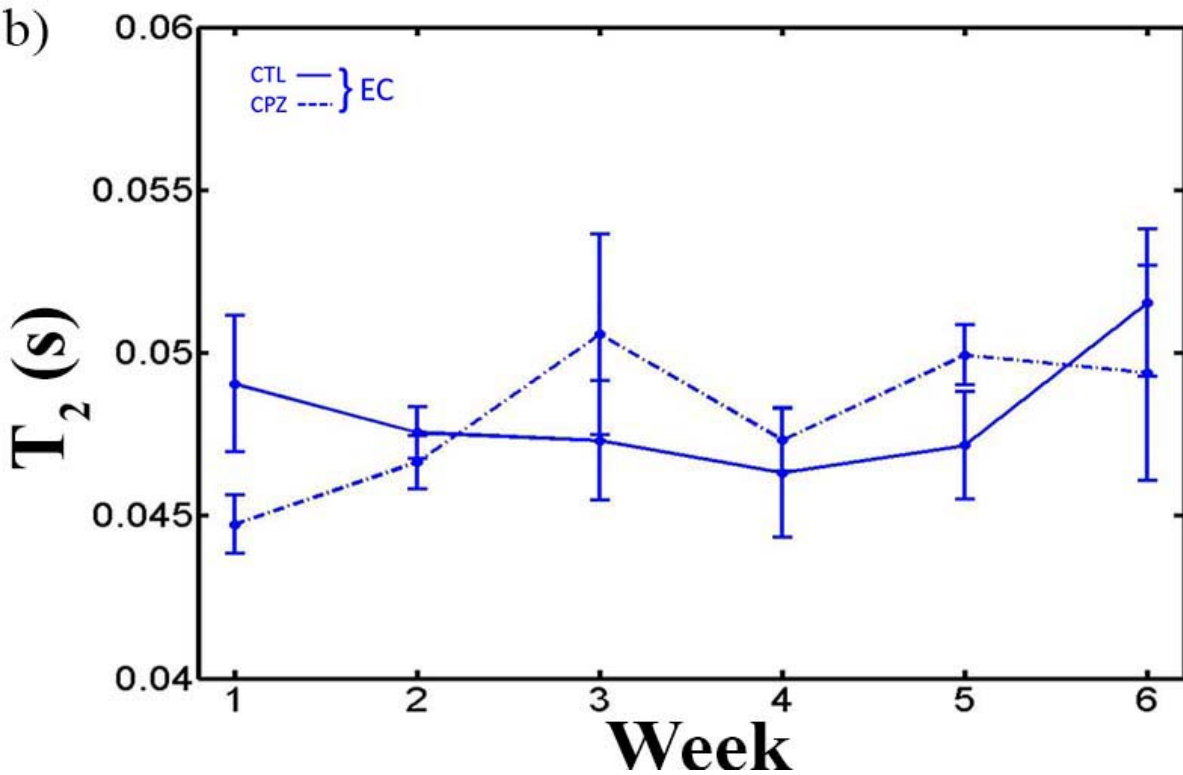
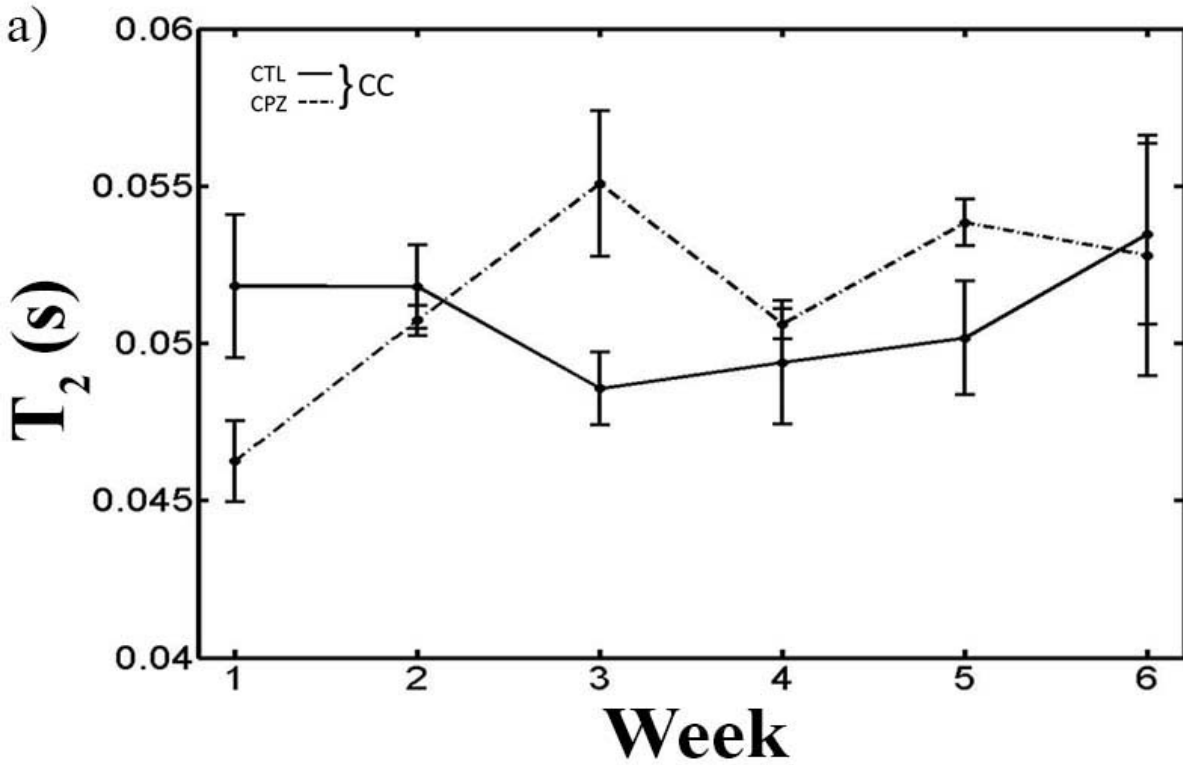


Figure 4.6: (a)  $T_2$  (s) vs week in the corpus callosum of control (solid) and cuprizone fed (dotted) mice. (b)  $T_2$  (s) vs week in the external capsule of control (solid) and cuprizone fed (dotted) mice. Each group mean contain  $n=3$  measurements excluding CTL week 4 where  $n=2$  due to suspected cross talk effects. \* denotes significant differences between groups.  $*p < 0.05$ ,  $**p < 0.01$ ,  $***p < 0.0001$ . All data shown for the corpus callosum in Figure B.4.

rather they fluctuated as feeding progressed. Values were more consistent in the control mice but were not steady as would be expected in control measurements.  $T_2$  signal amplitude should decrease as echo number increases but this was not the case in some of the control and cuprizone images throughout the study. In many cases, echo 1 was smaller than echo 2, and echoes 3-5 decreased as expected. In these cases echoes 2-5 were fit to Equation 2.20. The fit  $T_2$  value was higher when fitting all the echoes to this equation than when fitting only echoes 2-5. The  $T_2$  value was decreased in each case after echo 1 was excluded from the fitting, but values were still higher than previous measurements.

Representative  $T_1$  and  $T_2$  maps for control and cuprizone-fed mice at weeks 2 and 3 are shown in Figure 4.7, with numerical values at each week in Table 4.1.

#### 4.4.2 DTI

$\langle D \rangle$ ,  $\lambda_{\parallel}$ , and  $\lambda_{\perp}$  showed an overall increase as changes from the cuprizone progressed in the corpus callosum and external capsule in the cuprizone fed mice.

In both regions,  $\langle D \rangle$  was significantly larger in cuprizone fed mice than control mice at weeks 4 ( $p < .01$  in the CC,  $p < .05$  in the EC) and 6 ( $p < .05$  in the CC,  $p < .01$  in the EC).  $\langle D \rangle$  values from the first 2 weeks of feeding were significantly smaller than values from the last 4 weeks in the corpus callosum of cuprizone fed mice ( $p < .01$ ). In the external capsule,  $\langle D \rangle$  was significantly larger at weeks 3, 5 and 6 when compared to week 1 ( $p < .05$ ). Figure 4.8 shows the weekly progression of  $\langle D \rangle$  in the corpus callosum and external capsule of the control and cuprizone fed mice.

$\lambda_{\perp}$  was significantly larger in cuprizone fed mice than control mice at weeks 4 ( $p < .05$  in the CC,  $p < .01$  in the EC) and 6 ( $p < .01$  in the CC,  $p < .05$  in the EC) as shown in Figure 4.9. In addition,  $\lambda_{\perp}$  was significantly smaller at week 1 in the cuprizone fed mice compared to

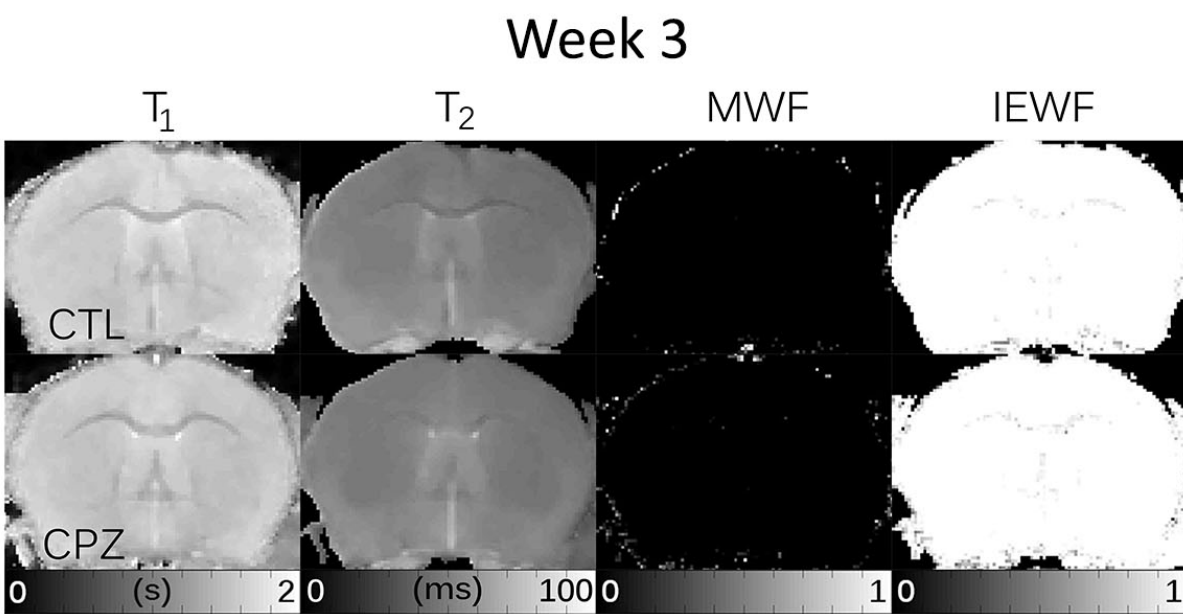
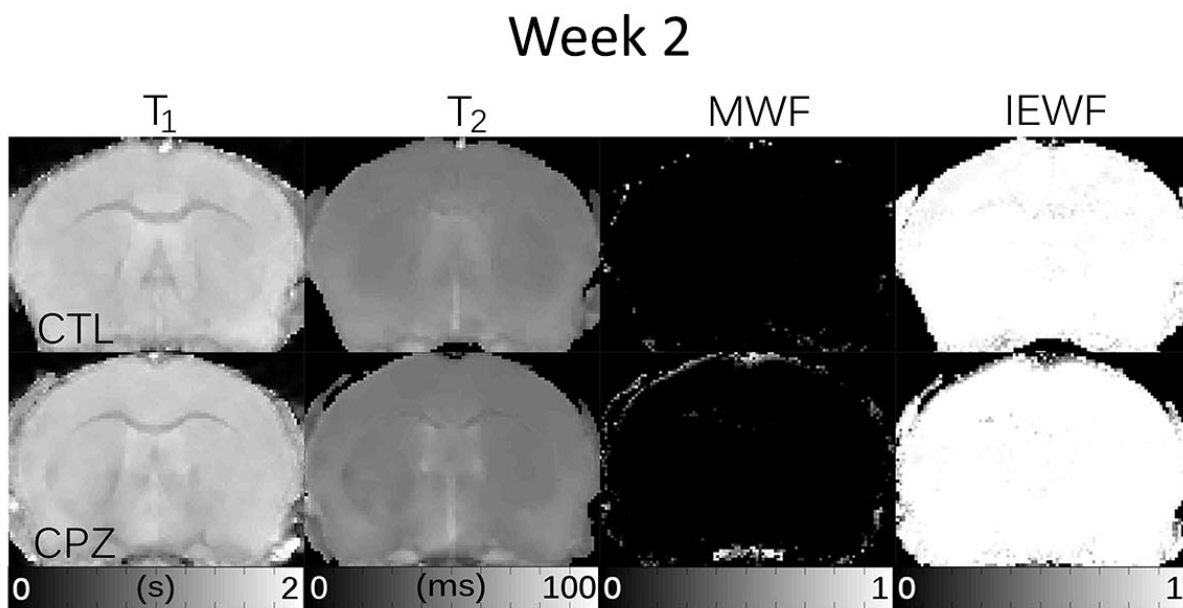


Figure 4.7: Representative Relaxometry metric maps for control (CTL) and cuprizone fed (CPZ) mice at weeks 2 and 3.

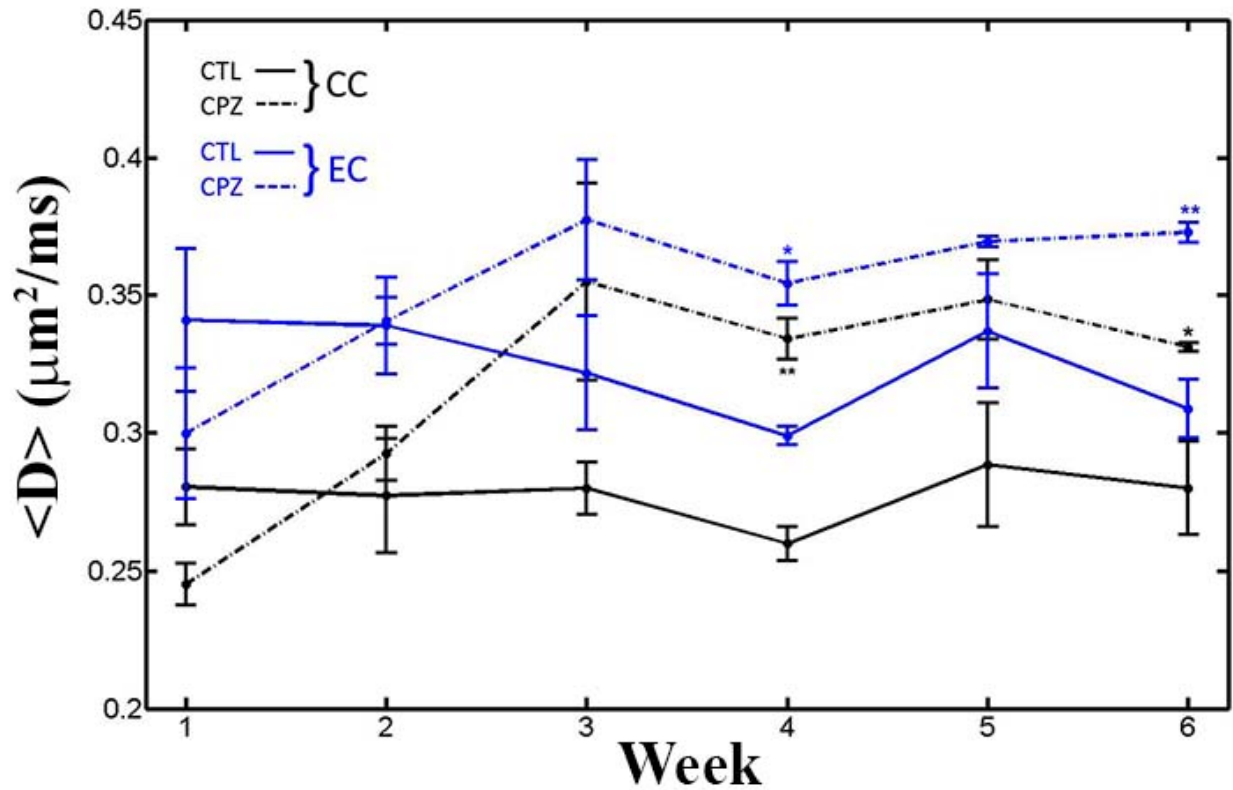


Figure 4.8: Weekly mean diffusivity,  $\langle D \rangle$ , in the corpus callosum (CC,black) and external capsule (EC,blue) of control (CTL,solid) and cuprizone fed (CPZ,dotted) mice. Each group mean at each week contains  $n=3$  measurements excluding CTL week 4 where  $n=2$  due to suspected cross talk effects. \* denotes significant differences between groups.  $*p < 0.05$ ,  $**p < 0.01$ ,  $***p < 0.0001$ . All data shown for the corpus callosum in ??.

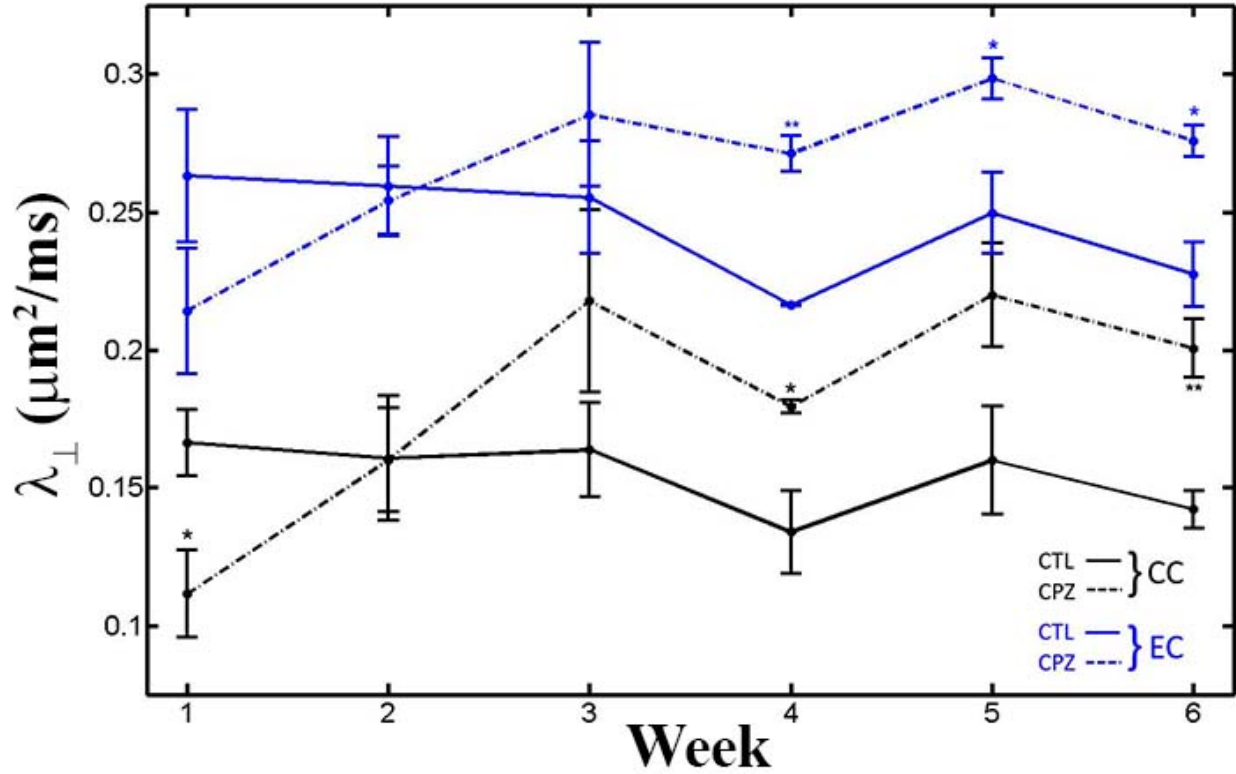


Figure 4.9: Weekly radial diffusivity,  $\lambda_{\perp}$ , in the corpus callosum (CC,black) and external capsule (EC,blue) of control (CTL,solid) and cuprizone fed (CPZ,dotted) mice. Each group mean at each week contains  $n=3$  measurements excluding CTL week 4 where  $n=2$  due to suspected cross talk effects. \* denotes significant differences between groups.  $*p < 0.05$ ,  $**p < 0.01$ ,  $***p < 0.0001$ . All data shown for the corpus callosum in Figure B.6.

controls ( $p=.05$ ). In the corpus callosum of the cuprizone fed mice,  $\lambda_{\perp}$  was only significantly smaller at week 1 compared to weeks 3 and 5 ( $p<.05$ ). In the external capsule, it was only significantly smaller at week 1 compared to week 5 ( $p<.05$ ).

$\lambda_{\parallel}$  was larger in the corpus callosum of cuprizone fed mice compared to control mice at all weeks but only by a significant amount at week 4 ( $p<.05$ ). In the external capsule, in addition to be significantly larger at week 4 ( $p<.05$ ),  $\lambda_{\parallel}$  was larger at weeks 3 ( $p<.05$ ) and 6 ( $p<.01$ ) in the cuprizone fed mice compared to controls. A significant increase in  $\lambda_{\parallel}$  of the cuprizone fed mice corpus callosum was apparent between weeks 1 and 4 ( $p<.05$ ). This increase was only apparent between weeks 1 and 3 as well as between weeks 1 and 6 in the external capsule ( $p<.05$ ). Figure 4.10 shows the weekly progression of  $\lambda_{\parallel}$  in the corpus

Table 4.4: Weekly *ex vivo* DTI metrics in the corpus callosum of control (CTL) and cuprizone (CPZ) mice. Values are reported as mean (SEM). Each group mean at each week contains n=3 measurements. \* denotes significant differences between groups.  $*p < 0.05$ ,  $**p < 0.01$ ,  $***p < 0.0001$

Week	Mouse	DTI			FA
		$\langle D \rangle$ ( $\mu m^2/ms$ )	$\lambda_{\perp}$ ( $\mu m^2/ms$ )	$\lambda_{\parallel}$ ( $\mu m^2/ms$ )	
1	CTL	0.28 (0.01)	0.17 (0.01)	0.51 (0.02)	0.62 (0.02)
	CPZ	0.25 (0.01)	0.11* (0.01)	0.51 (0.01)	0.75 (0.03)
2	CTL	0.28 (0.02)	0.16 (0.02)	0.51 (0.03)	0.62 (0.05)
	CPZ	0.29 (0.01)	0.16 (0.02)	0.56 (0.03)	0.65 (0.05)
3	CTL	0.28 (0.01)	0.16 (0.01)	0.51 (0.03)	0.61 (0.05)
	CPZ	0.35 (0.03)	0.22 (0.03)	0.63 (0.04)	0.59 (0.03)
4	CTL	0.260 (0.004)	0.13 (0.01)	0.51 (0.01)	0.69 (0.03)
	CPZ	0.33** (0.01)	0.179* (0.002)	0.64* (0.02)	0.67 (0.01)
5	CTL	0.29 (0.02)	0.16 (0.02)	0.55 (0.03)	0.66 (0.03)
	CPZ	0.35 (0.01)	0.22 (0.02)	0.61 (0.01)	0.57 (0.03)
6	CTL	0.28 (0.01)	0.14 (0.01)	0.56 (0.03)	0.697 (0.004)
	CPZ	0.33* (0.01)	0.20** (0.01)	0.59 (0.01)	0.60* (0.03)

callosum and external capsule of the control and cuprizone fed mice.

FA showed differences between groups at week 6 in the corpus callosum ( $p < .05$ ) and at week 4 in the external capsule ( $p < .01$ ). The weekly progression of FA in the corpus callosum and external capsule of the control and cuprizone fed mice is shown in Figure 4.11. Week to week decreases in the corpus callosum of the cuprizone fed mice were shown to be non-significant. In the external capsule the decrease from week 1 to week 5 proved to be significant ( $p < .05$ ).

Representative DTI metric maps for control and cuprizone fed mice at weeks 2 and 3 are shown in Figure 4.12 with numerical values shown in Table 4.4.

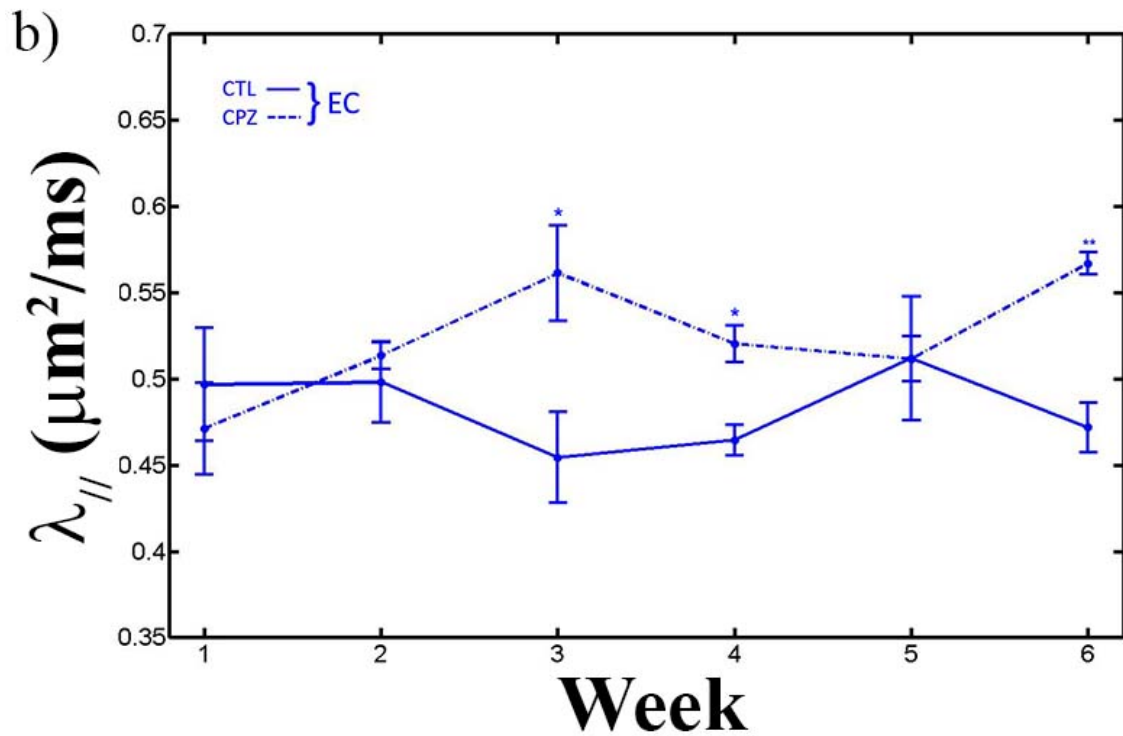
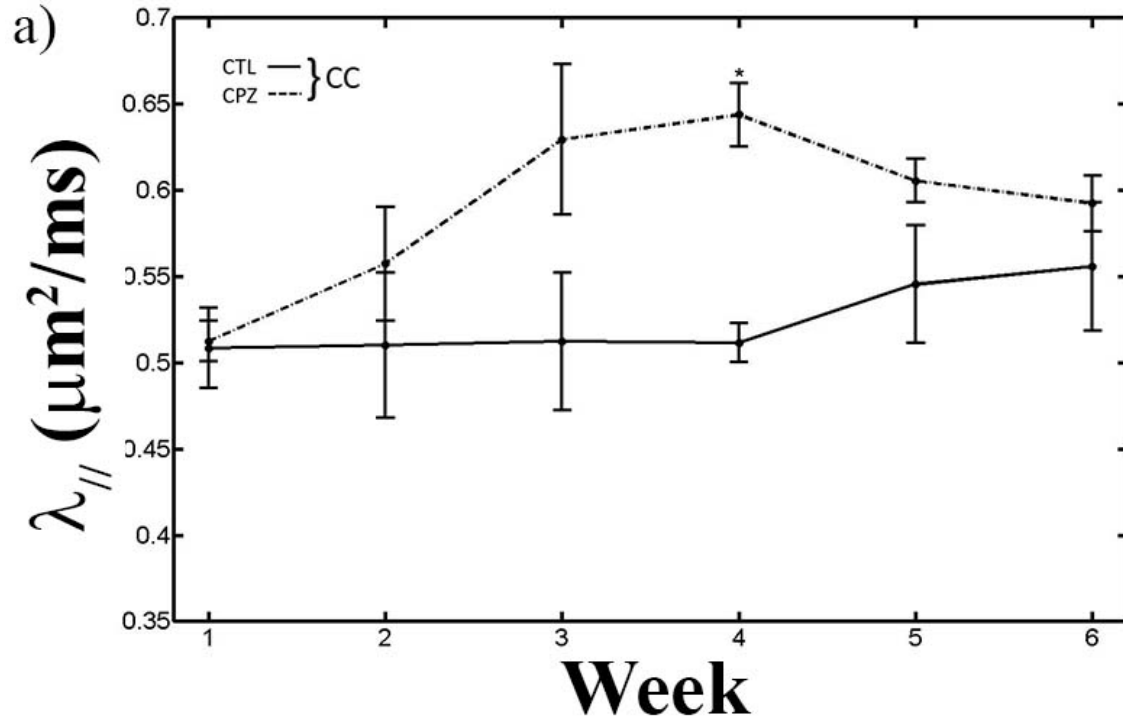


Figure 4.10: Weekly axial diffusivity,  $\lambda_{||}$ , in the corpus callosum (CC,black) and external capsule (EC,blue) of control (CTL,solid) and cuprizone fed (CPZ,dotted) mice. Each group mean at each week contains  $n=3$  measurements excluding CTL week 4 where  $n=2$  due to suspected cross talk effects. \* denotes significant differences between groups.  $*p < 0.05$ ,  $**p < 0.01$ ,  $***p < 0.0001$ . All data shown for the corpus callosum in Figure B.7.

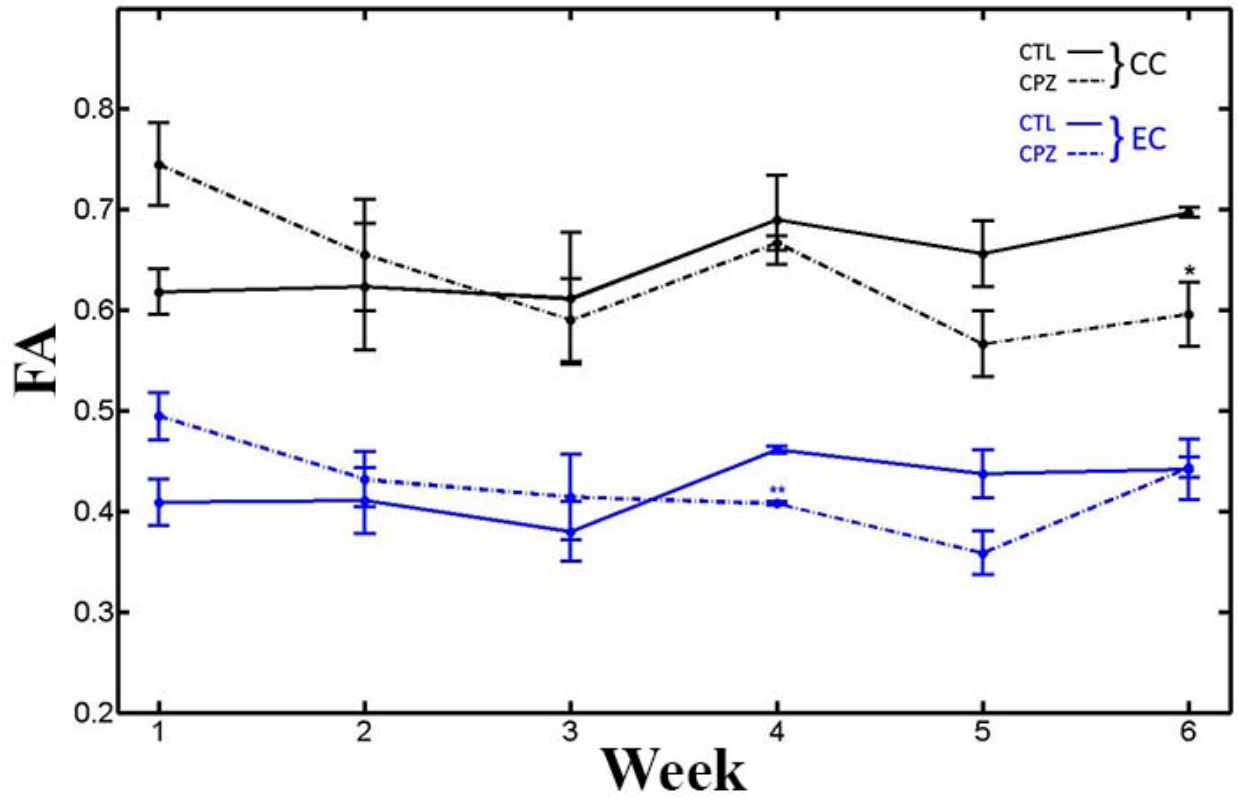


Figure 4.11: Weekly fractional anisotropy, FA, in the corpus callosum (CC,black) and external capsule (EC,blue) of control (CTL,solid) and cuprizone fed (CPZ,dotted) mice. Each group mean at each week contains n=3 measurements excluding CTL week 4 where n=2 due to suspected cross talk effects. \* denotes significant differences between groups. \* $p < 0.05$ , \*\* $p < 0.01$ , \*\*\* $p < 0.0001$ . All data shown for the corpus callosum in Figure B.8.

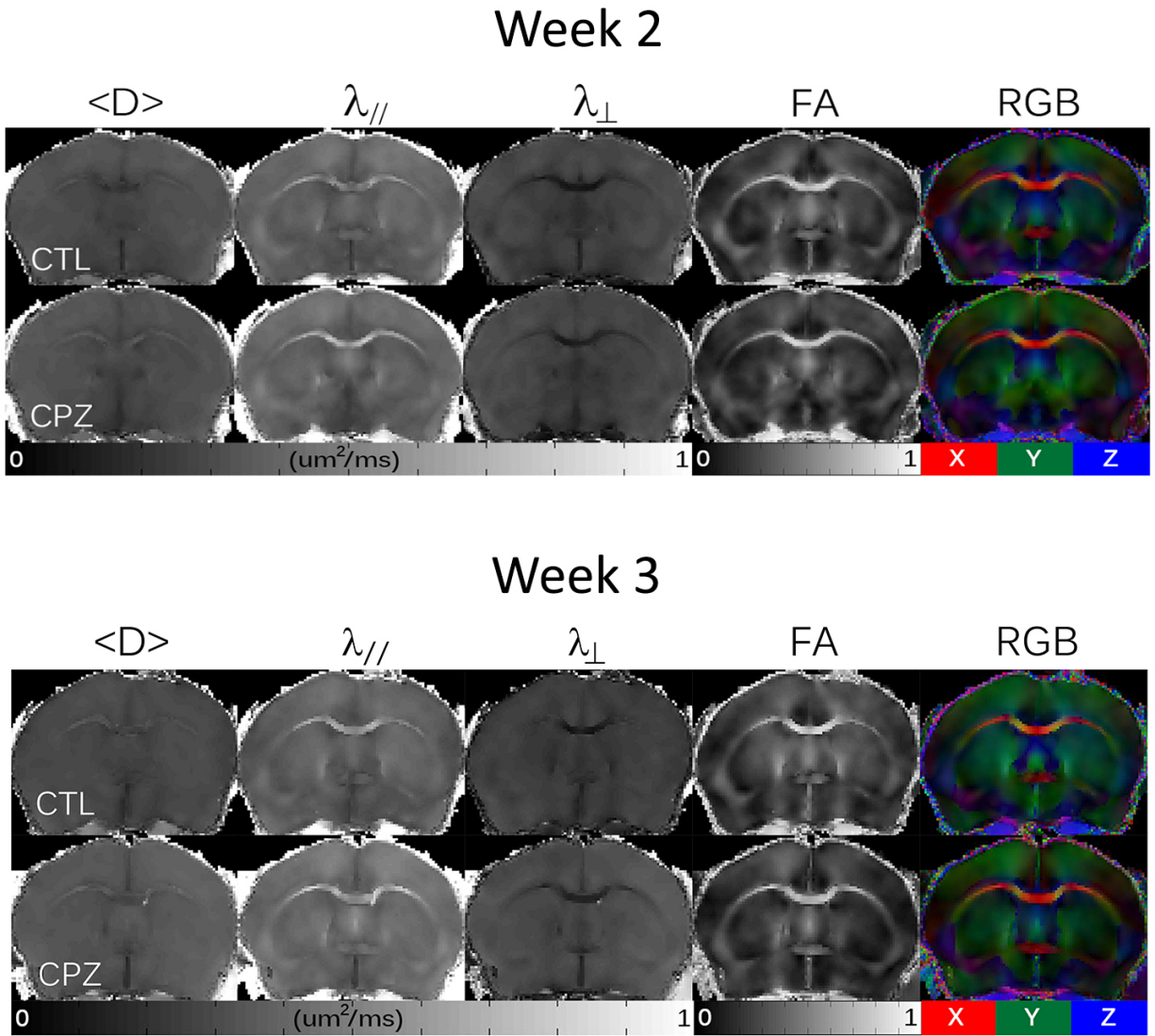


Figure 4.12: Representative DTI metric maps for control (CTL) and cuprizone fed (CPZ) mice at weeks 2 and 3.

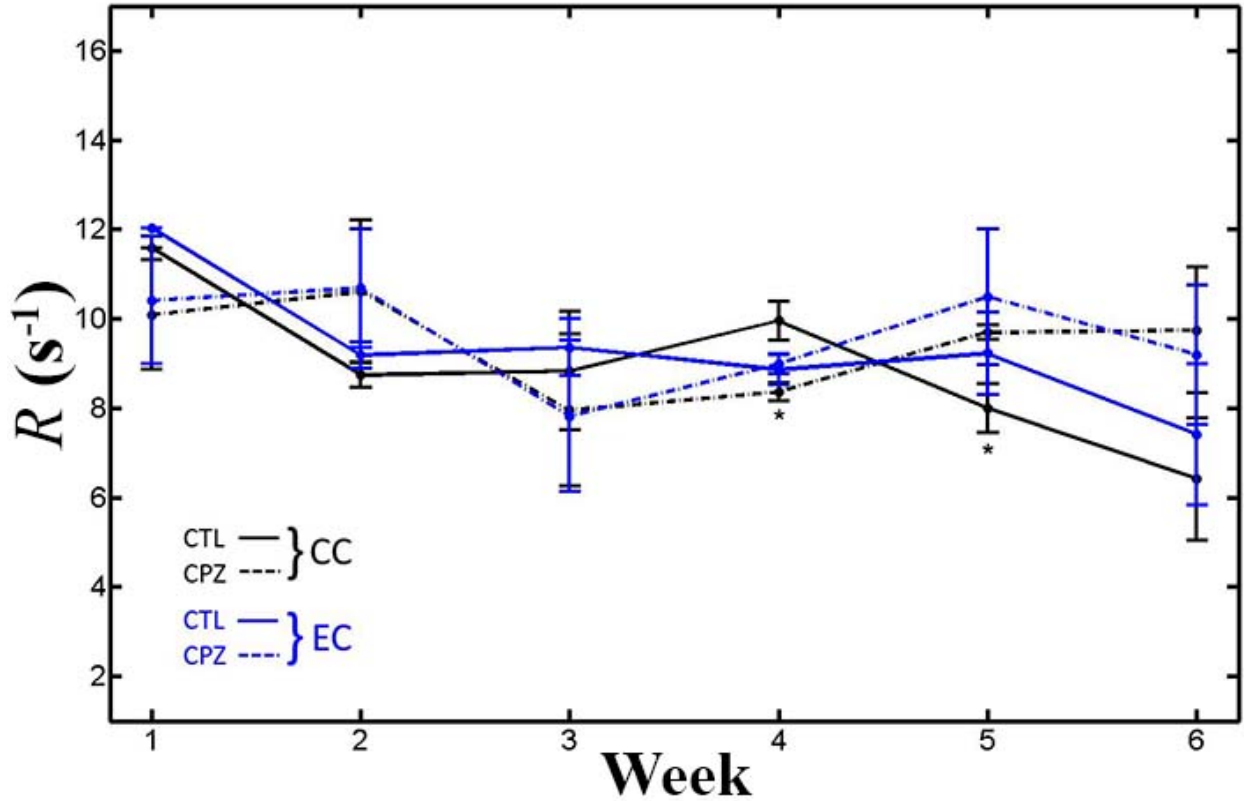


Figure 4.13: Weekly magnetization transfer rate,  $R$ , values in the corpus callosum (CC, black) and external capsule (EC, blue) of control (CTL, solid) and cuprizone fed (CPZ, dotted) mice. Each group mean at each week contains  $n=3$  measurements excluding CTL week 1 where  $n=1$  due to contamination of  $k$ -space with high frequency noise in  $M_{sat}$  images that was unable to be removed and CTL week 4 where  $n=2$  for suspected cross talk effects. \* denotes significant differences between groups. \* $p < 0.05$ , \*\* $p < 0.01$ , \*\*\* $p < 0.0001$ . All data shown for the corpus callosum in Figure B.9.

### 4.4.3 qMTI

The magnetization transfer rate,  $R$ , in the corpus callosum was found to be significantly smaller in the cuprizone fed mice at week 4 ( $p < .05$ ) and larger at week 5 ( $p < .05$ ) when compared to the control mice (Figure 4.13). There were no significant week to week changes in  $R$  in the corpus callosum or external capsule of the cuprizone-fed mice.

The transverse relaxation time of the liquid pool,  $T_2^A$  (Figure 4.14), was found to be significantly larger in the cuprizone-fed mice corpus callosum and external capsule compared

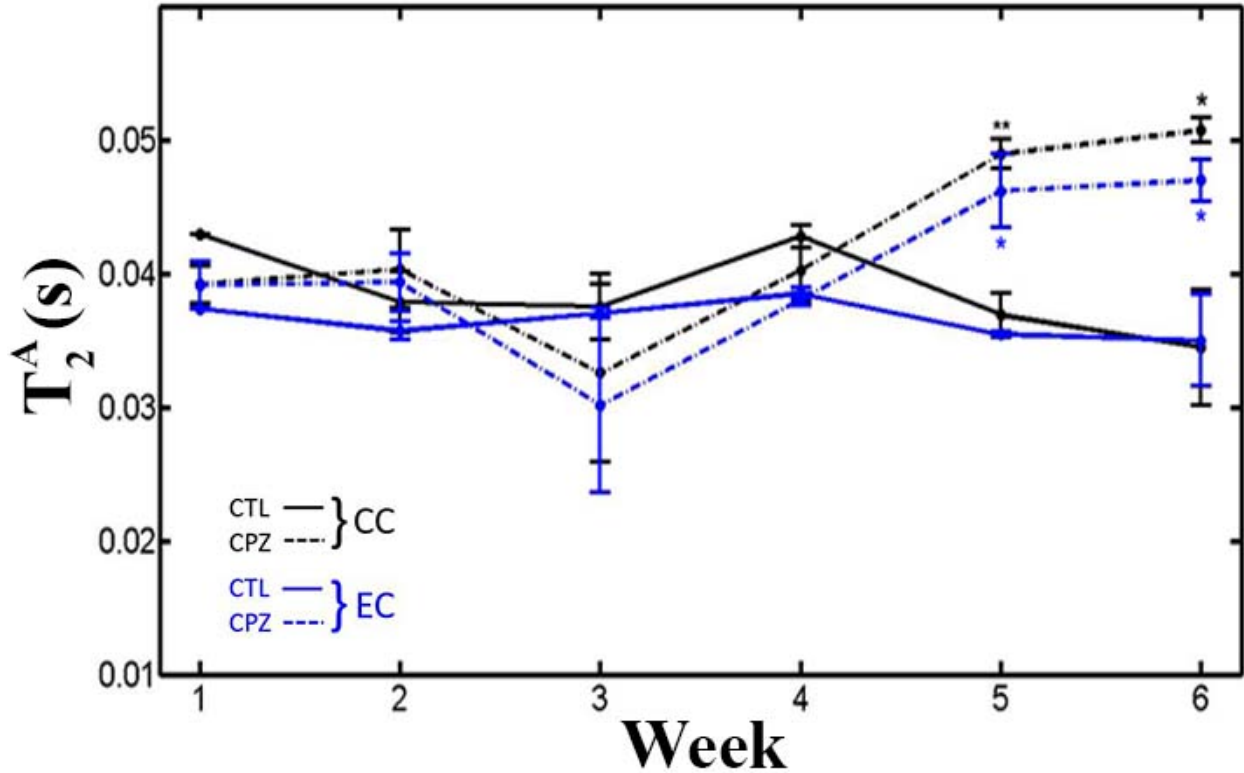


Figure 4.14: Weekly transverse relaxation time of the liquid pool,  $T_2^A$ , values in the corpus callosum (CC, black) and external capsule (EC, blue) of control (CTL, solid) and cuprizone fed (CPZ, dotted) mice. Each group mean at each week contains  $n=3$  measurements excluding CTL week 1 where  $n=1$  due to contamination of  $k$ -space with high frequency noise in  $M_s$ at images that was unable to be removed and CTL week 4 where  $n=2$  for suspected cross talk effects. \* denotes significant differences between groups. \* $p < 0.05$ , \*\* $p < 0.01$ , \*\*\* $p < 0.0001$ . All data shown for the corpus callosum in Figure B.10.

to control mice at week 5 ( $p < .01$  in the CC,  $p < .05$  in the EC) and week 6 ( $p < .05$  for both). In the corpus callosum of the cuprizone-fed mice,  $T_2^A$  was found to be significantly smaller at week 3 compared to weeks 5 and 6 ( $p < .05$ ).  $T_2^A$  was also found to be significantly smaller at week 3 compared to week 5 in the external capsule ( $p < .05$ ).

The transverse relaxation time of the bound pool,  $T_2^B$ , was not significantly different between groups throughout cuprizone feeding and no significant week to week changes occurred in the corpus callosum of the cuprizone fed mice (Figure 4.15).

The longitudinal relaxation rate of the liquid pool,  $R_A$ , in the corpus callosum and

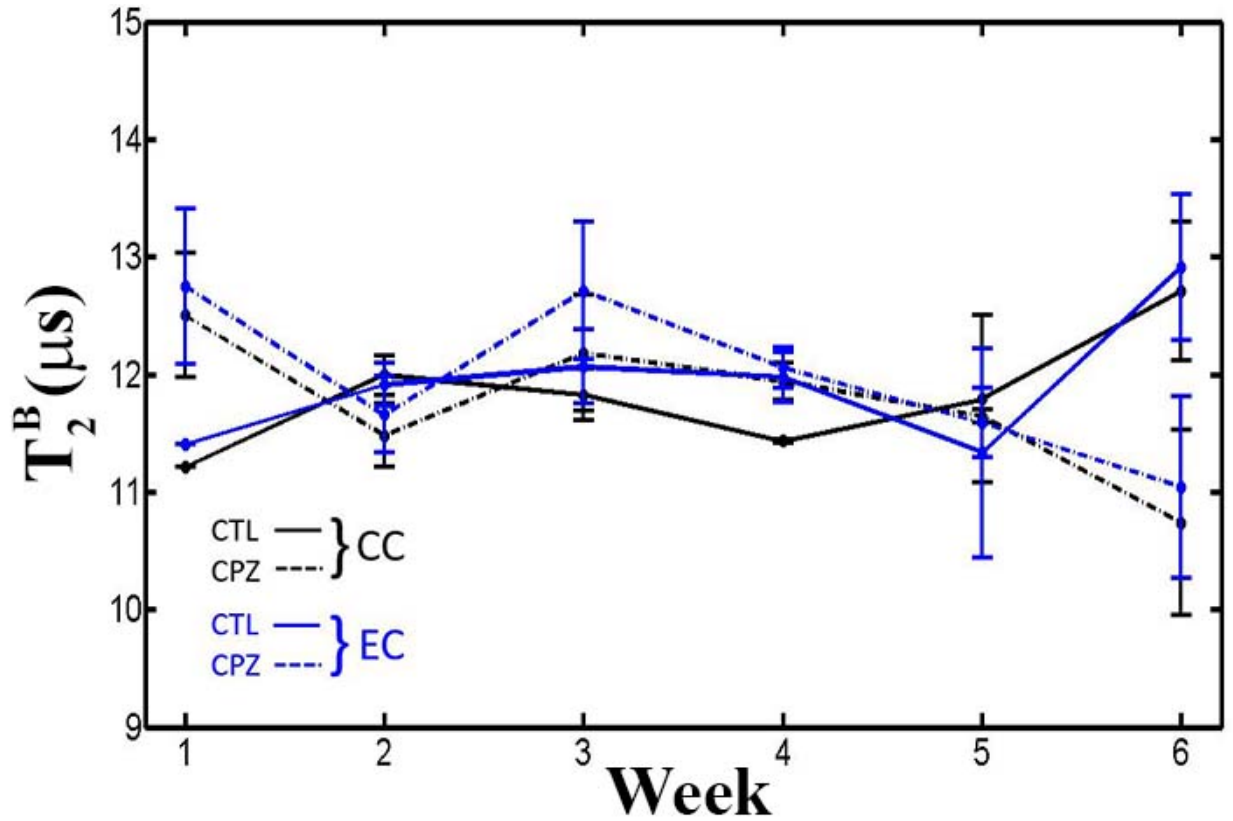


Figure 4.15: Weekly transverse relaxation time of the bound pool,  $T_2^B$ , values in the corpus callosum (CC, black) and external capsule (EC, blue) of control (CTL, solid) and cuprizone fed (CPZ, dotted) mice. Each group mean at each week contains  $n=3$  measurements excluding CTL week 1 where  $n=1$  due to contamination of  $k$ -space with high frequency noise in  $M_s$  images that was unable to be removed and CTL week 4 where  $n=2$  for suspected cross talk effects.  $*p < 0.05$ ,  $**p < 0.01$ ,  $***p < 0.0001$ . All data shown for the corpus callosum in Figure B.11.

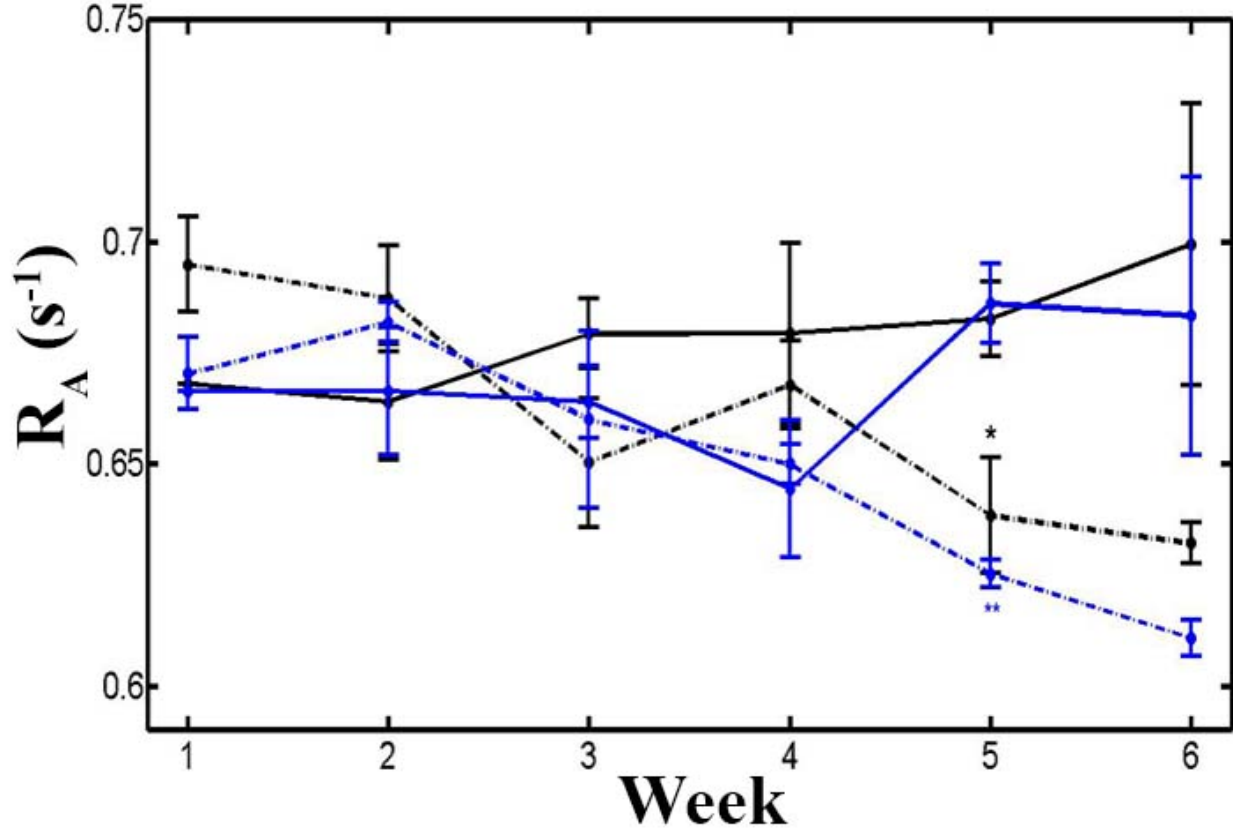


Figure 4.16: Weekly longitudinal relaxation rate of the liquid pool,  $R_A$ , values in the corpus callosum (CC,black) and external capsule (EC,blue) of control (CTL,solid) and cuprizone fed (CPZ,dotted) mice. Each group mean at each week contains  $n=3$  measurements excluding CTL week 1 where  $n=1$  due to contamination of  $k$ -space with high frequency noise in  $M_s$  at images that was unable to be removed and CTL week 4 where  $n=2$  for suspected cross talk effects. \* denotes significant differences between groups.  $*p < 0.05$ ,  $**p < 0.01$ ,  $***p < 0.0001$ . All data shown for the corpus callosum in Figure B.12.

external capsule of the cuprizone-fed mice was only significantly smaller than control mice values at week 5 ( $p < .05$  in the CC,  $p < .01$  in the EC).  $R_A$  was significantly smaller at weeks 5 and 6 compared to week 1 in the corpus callosum of the cuprizone-fed mice. Week 6 values were also significantly smaller compared to week 2 ( $p < .01$  for all). In the external capsule,  $R_A$  values during the first 3 weeks of feeding was significantly larger than values from the last 3 weeks of feeding (Figure 4.16).

The bound pool fraction,  $f$ , in the corpus callosum and external capsule of the cuprizone-fed mice was significantly smaller when compared to control mice at week 5 ( $p < .01$  for both)

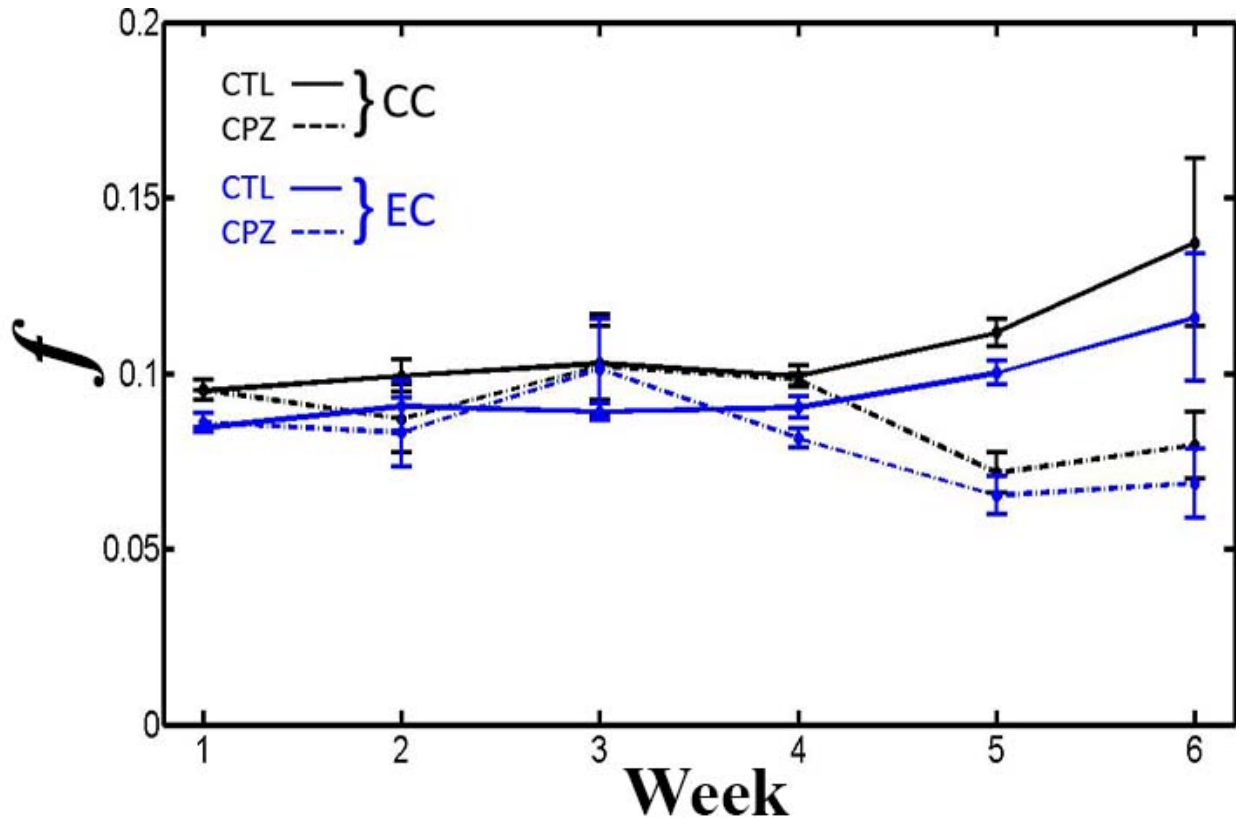


Figure 4.17: Weekly bound pool fraction,  $f$ , in the corpus callosum (CC,black) and external capsule (EC,blue) of control (CTL,solid) and cuprizone fed (CPZ,dotted) mice. Each group mean at each week contains  $n=3$  measurements excluding CTL week 1 where  $n=1$  due to contamination of  $k$ -space with high frequency noise in  $M_{sat}$  images that was unable to be removed and CTL week 4 where  $n=2$  for suspected cross talk effects. \* denotes significant differences between groups.  $*p < 0.05$ ,  $**p < 0.01$ ,  $***p < 0.0001$ . All data shown for the corpus callosum in Figure B.13.

(Figure 4.17). There were no significant week to week changes in  $f$  in the corpus callosum or external capsule of the cuprizone-fed mice.

Representative qMTI metric maps for control and cuprizone-fed mice at weeks 2 and 3 are shown in Figure 4.18 with numerical values shown in Table 4.5.

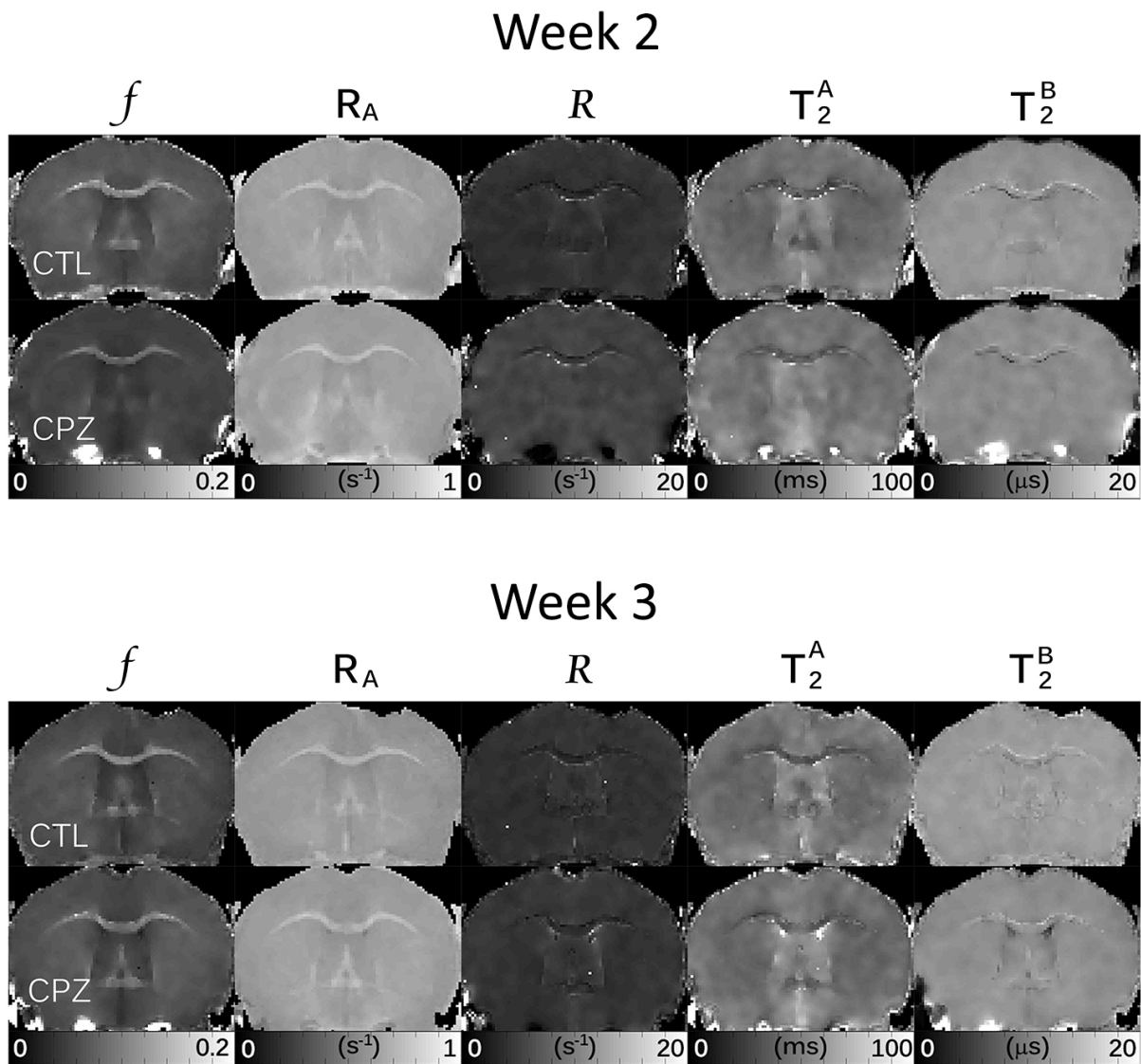


Figure 4.18: Representative qMTI metric maps for control (CTL) and cuprizone fed (CPZ) mice at weeks 2 and 3.

Table 4.5: Weekly *ex vivo* qMTI metrics in the corpus callosum of control (CTL) and cuprizone (CPZ) mice. Values are reported as mean (SEM). Measurements contain  $n = 3$  per group at each week (except for week 1 where CTL=1 and week 4 where  $n=2$  CTL). \* denotes significant differences between groups.  $*p < 0.05$ ,  $**p < 0.01$ ,  $***p < 0.0001$

Week	Mouse	qMTI				
		$R$ ( $s^{-1}$ )	$T_2^A$ ( $ms$ )	$T_2^B$ ( $\mu s$ )	$R_A$ ( $s^{-1}$ )	$f$
1	CTL	11.6 (-)	43 (-)	11.2 (-)	0.67 (-)	0.10 (-)
	CPZ	10 (1)	39 (1)	12.5 (0.4)	0.69 (0.01)	0.095 (0.002)
2	CTL	8.7 (0.2)	38 (2)	11.9 (0.1)	0.66 (0.01)	0.10 (0.01)
	CPZ	11 (1)	40 (2)	11.5 (0.2)	0.69 (0.01)	0.09 (0.01)
3	CTL	9 (1)	38 (5)	11.8 (0.2)	0.68 (0.01)	0.10 (0.01)
	CPZ	8 (1)	33 (5)	12.2 (0.4)	0.65 (0.01)	0.10 (0.01)
4	CTL	10.0 (0.3)	43 (2)	11.43 (0.01)	0.68 (0.01)	0.099 (0.001)
	CPZ	8.4* (0.2)	40 (2)	11.9 (0.1)	0.67 (0.01)	0.098 (0.001)
5	CTL	8.0 (0.4)	37 (1)	11.8 (0.6)	0.68 (0.01)	0.11 (0.01)
	CPZ	9.7* (0.1)	49** (1)	11.64 (0.05)	0.64* (0.01)	0.07** (0.01)
6	CTL	6 (1)	34 (1)	12.7 (0.5)	0.70 (0.03)	0.14 (0.01)
	CPZ	10 (1)	51* (1)	10.7 (0.6)	0.632 (0.004)	0.08 (0.01)

## 4.5 MRI Correlations

### *Voxel-based analysis of the combined corpus callosum and external capsule data*

Voxel based Spearman correlation coefficients were calculated between all *ex vivo* MRI metrics in the CC+EC of control (n=17), cuprizone (n=18) and combined data set (n=35). ROI based Spearman correlation coefficients were calculated between all *ex vivo* and *in vivo* MRI metrics in the CC+EC. The combined mouse data set was analyzed to include measurements with varying degrees of myelination throughout the 6 weeks of *ex vivo* measurements. The increased number of measurements can improve the power of correlations.

Voxel based analysis in the corpus callosum showed nearly all correlations to be statistically significant due to the large amount of data points available in the combined data set. Amongst some of the strongest correlations in the combined data set were  $T_2$  and  $T_2^A$  ( $\rho=-.98$ ),  $f$  and  $R_A$  ( $\rho=.97$ ),  $R$  and  $R_A$  ( $\rho=-.77$ ), and FA and  $T_1$  ( $\rho=-.87$ ). Similarly, nearly all voxel based correlations in the separate control and cuprizone data sets were statistically significant. Both individual data sets shared the same strong correlations as the combined data set. In some cases these coefficients were slightly weaker or stronger than in the combined data set.

Comparison of voxel-based Spearman correlation coefficients of the control and cuprizone fed mice CC+EC is shown in Table 4.6.

### *ROI-based analysis of the corpus callosum and external capsule*

There were fewer significant correlations in the ROI based analysis than in the voxel based analysis due to the decreased number of data points. P-values of the coefficients for the control, cuprizone and combined data sets were also not as small as with the voxel based analysis.

Table 4.6: Comparison of voxel-based Spearman correlation coefficients ( $\rho$ ) for MRI metrics between the control (upper right) and cuprizone fed mice (lower left) corpus callosum + external capsule.  $*p \ll 0.05$ ,  $**p < 0.01$ ,  $***p < 0.0001$ ,  $^\dagger p \ll 0.0001$

Metric	$f$	$R_A$	$R$	$T_2^A$	$T_2^B$	$\langle D \rangle$	$\lambda_{\parallel}$	$\lambda_{\perp}$	FA	$T_1$	$T_2$	$T_2w$	MTR
$f$	-	0.96 <sup>†</sup>	-0.75 <sup>†</sup>	0.65 <sup>†</sup>	-0.51 <sup>†</sup>	0.22 <sup>†</sup>	-0.23 <sup>†</sup>	0.35 <sup>†</sup>	-0.47 <sup>†</sup>	0.49 <sup>†</sup>	-0.75 <sup>†</sup>	-	-
$R_A$	0.96 <sup>†</sup>	-	-0.83 <sup>†</sup>	0.46 <sup>†</sup>	-0.48 <sup>†</sup>	0.25 <sup>†</sup>	-0.29 <sup>†</sup>	0.25 <sup>†</sup>	-0.46 <sup>†</sup>	0.44 <sup>†</sup>	-0.58 <sup>†</sup>	-	-
$R$	-0.67 <sup>†</sup>	-0.79 <sup>†</sup>	-	-0.18 <sup>†</sup>	0.60 <sup>†</sup>	-0.29 <sup>†</sup>	0.26 <sup>†</sup>	0.00	0.27 <sup>†</sup>	-0.18 <sup>†</sup>	0.30 <sup>†</sup>	-	-
$T_2^A$	0.52 <sup>†</sup>	0.29 <sup>†</sup>	0.10 <sup>†</sup>	-	-0.38 <sup>†</sup>	-0.01	-0.02	0.48 <sup>†</sup>	-0.35 <sup>†</sup>	0.47 <sup>†</sup>	-0.98 <sup>†</sup>	-	-
$T_2^B$	-0.66 <sup>†</sup>	-0.61 <sup>†</sup>	0.47 <sup>†</sup>	-0.44 <sup>†</sup>	-	0.09 <sup>†</sup>	-0.01	-0.12 <sup>†</sup>	0.06 <sup>**</sup>	-0.07 <sup>**</sup>	0.42 <sup>†</sup>	-	-
$\langle D \rangle$	0.25 <sup>†</sup>	0.24 <sup>†</sup>	-0.25 <sup>†</sup>	0.10 <sup>†</sup>	-0.29 <sup>†</sup>	-	-0.01	-0.02	-0.01	-0.02	-0.04 <sup>*</sup>	-	-
$\lambda_{\parallel}$	-0.22 <sup>†</sup>	-0.17 <sup>†</sup>	-0.09 <sup>†</sup>	-0.24 <sup>†</sup>	0.10 <sup>†</sup>	-0.15 <sup>†</sup>	-	0.35 <sup>†</sup>	0.76 <sup>†</sup>	-0.43 <sup>†</sup>	0.05 <sup>**</sup>	-	-
$\lambda_{\perp}$	0.24 <sup>†</sup>	0.19 <sup>†</sup>	-0.15 <sup>†</sup>	0.26 <sup>†</sup>	-0.06 <sup>**</sup>	-0.10 <sup>†</sup>	0.47 <sup>†</sup>	-	-0.31 <sup>†</sup>	0.67 <sup>†</sup>	-0.48 <sup>†</sup>	-	-
FA	-0.42 <sup>†</sup>	-0.33 <sup>†</sup>	0.02	-0.46 <sup>†</sup>	0.14 <sup>†</sup>	-0.10 <sup>†</sup>	0.69 <sup>†</sup>	-0.25 <sup>†</sup>	-	-0.90 <sup>†</sup>	0.38 <sup>†</sup>	-	-
$T_1$	0.46 <sup>†</sup>	0.37 <sup>†</sup>	-0.11 <sup>†</sup>	0.47 <sup>†</sup>	-0.14 <sup>†</sup>	0.02	-0.32 <sup>†</sup>	0.62 <sup>†</sup>	-0.88 <sup>†</sup>	-	-0.49 <sup>†</sup>	-	-
$T_2$	-0.65 <sup>†</sup>	-0.44 <sup>†</sup>	0.03	-0.98 <sup>†</sup>	0.52 <sup>†</sup>	-0.14 <sup>†</sup>	0.26 <sup>†</sup>	-0.27 <sup>†</sup>	0.50 <sup>†</sup>	-0.51 <sup>†</sup>	-	-	-
$T_2w$	-	-	-	-	-	-	-	-	-	-	-	-	0.54 <sup>†</sup>
MTR	-	-	-	-	-	-	-	-	-	-	-	0.69 <sup>†</sup>	-

Amongst some of the strongest correlations in the combined data set were  $T_2$  and  $T_2^A$  ( $\rho=-.96$ ),  $f$  and  $R_A$  ( $\rho=.98$ ),  $\lambda_{\parallel}$  and FA ( $\rho=.89$ ), and  $\lambda_{\parallel}$  and  $\lambda_{\perp}$  ( $\rho=.85$ ). These strong correlations also existed in the separate control and cuprizone data sets.

Comparison of voxel-based and ROI-based Spearman correlation coefficients ( $\rho$ ) of MRI metrics the combined dataset CC+EC are shown in Table 4.7.

Table 4.7: Comparison of voxel-based (upper right) and ROI-based (lower left) Spearman correlation coefficients ( $\rho$ ) of MRI metrics for the combined data set corpus callosum + external capsule. Values in bold are amongst the strongest correlations and are mentioned in the text.  $*p \ll 0.05$ ,  $**p < 0.01$ ,  $***p < 0.0001$ ,  $^\dagger p \ll 0.0001$

Metric	$f$	$R_A$	$R$	$T_2^A$	$T_2^B$	$\langle D \rangle$	$\lambda_{\parallel}$	$\lambda_{\perp}$	FA	$T_1$	$T_2$	$T_2w$	MTR
$f$	-	<b>0.97<sup>†</sup></b>	-0.68 <sup>†</sup>	0.60 <sup>†</sup>	-0.61 <sup>†</sup>	0.26 <sup>†</sup>	-0.31 <sup>†</sup>	0.19 <sup>†</sup>	-0.48 <sup>†</sup>	0.45 <sup>†</sup>	-0.71 <sup>†</sup>	-	-
$R_A$	<b>0.98<sup>†</sup></b>	-	<b>-0.78<sup>†</sup></b>	0.40 <sup>†</sup>	-0.57 <sup>†</sup>	0.26 <sup>†</sup>	-0.31 <sup>†</sup>	0.12 <sup>†</sup>	-0.42 <sup>†</sup>	0.37 <sup>†</sup>	-0.53 <sup>†</sup>	-	-
$R$	-0.69*	<b>-0.77<sup>†</sup></b>	-	-0.04**	0.55 <sup>†</sup>	-0.27 <sup>†</sup>	0.11 <sup>†</sup>	-0.06	0.15 <sup>†</sup>	-0.14 <sup>†</sup>	0.16 <sup>†</sup>	-	-
$T_2^A$	0.38*	0.22	0.23	-	-0.42 <sup>†</sup>	0.06 <sup>†</sup>	-0.20 <sup>†</sup>	0.30 <sup>†</sup>	-0.44 <sup>†</sup>	0.47 <sup>†</sup>	<b>-0.98<sup>†</sup></b>	-	-
$T_2^B$	-0.78 <sup>†</sup>	-0.78 <sup>†</sup>	0.60**	-0.36*	-	-0.12 <sup>†</sup>	0.12 <sup>†</sup>	-0.03*	0.13 <sup>†</sup>	-0.10 <sup>†</sup>	0.48 <sup>†</sup>	-	-
$\langle D \rangle$	0.35*	0.35*	-0.41*	0.04	-0.37*	-	-0.13 <sup>†</sup>	-0.08 <sup>†</sup>	-0.08 <sup>†</sup>	0.00	-0.11 <sup>†</sup>	-	-
$\lambda_{\parallel}$	-0.43*	-0.36*	0.11	-0.51**	0.36*	-0.24	-	0.46 <sup>†</sup>	0.74 <sup>†</sup>	-0.36 <sup>†</sup>	0.23 <sup>†</sup>	-	-
$\lambda_{\perp}$	-0.32	-0.26	0.08	-0.34*	0.25	-0.13	<b>0.85<sup>†</sup></b>	-	-0.21 <sup>†</sup>	0.62 <sup>†</sup>	-0.30 <sup>†</sup>	-	-
FA	-0.41*	-0.32	0.15	-0.47**	0.31	-0.29	<b>0.89<sup>†</sup></b>	0.57**	-	<b>-0.87<sup>†</sup></b>	0.47 <sup>†</sup>	-	-
$T_1$	0.25	0.16	0.03	0.44**	-0.15	0.13	-0.57**	-0.13	-0.83 <sup>†</sup>	-	-0.49 <sup>†</sup>	-	-
$T_2$	-0.55**	-0.41*	0.06	<b>-0.96<sup>†</sup></b>	0.50**	-0.14	0.52**	0.33	0.50**	-0.46**	-	-	-
$T_2w$	0.09	0.19	-0.37*	-0.43*	-0.07	-0.08	0.35*	0.16	0.41*	-0.48**	0.31	-	0.62 <sup>†</sup>
MTR	-0.14	-0.07	0.01	-0.42**	0.47**	-0.26	0.19	0.09	0.25	-0.27	0.43**	0.16	-

## 4.6 Electron Microscopy

Electron Microscopy (EM) images of control and cuprizone fed corpus callosum at weeks 2 and 3 are shown in Figure 4.19, Figure 4.20, Figure 4.21, and Figure 4.22.

EM 5000x magnification images show swollen glial cell processes at both weeks in 5 of the 6 (n=2 from week 2, n= 3 from week 3) cuprizone fed mice analyzed. Two of the 5 control mice (n=1 from week 2, n=1 from week 3) analyzed displayed glial cell process swelling (Figure 4.23) with fractions similar to those in the cuprizone fed mice. This apparent anomaly may be explained by delayed or incomplete fixation after the PBS flush causing the cells to swell before they were fixed, or as an artifact of the subsequent imaging conditions.

Images from the corpus callosa of the cuprizone fed mouse at week 2 and 3 reveal persistence of myelinated axons, swelling of axons, microglia and the apoptosis of oligodendrocytes. Fraying of the myelin bilayers at week 3 can be seen in the 15 000 x magnification images (Figure 4.24). Ultrastructural analysis showed mainly non-significant differences in the cellular feature fractions being measured between groups at weeks 2 and 3. A signifi-

Table 4.8: Summary of measurements and distributions taken from EM images of control and cuprizone fed corpus callosa. Values are reported as mean (SEM). Significant differences between groups are denoted with \* where  $*p < 0.05$ .

		Metric	Week 2		Week 3	
			Control	Cuprizone	Control	Cuprizone
Distribution of Cells	Myelinated Axons (%)	0.31 (0.01)	0.28* (0.02)	0.35 (0.02)	0.25 (0.02)	
	Myelin Sheaths (%)	0.19 (0.04)	0.18 (0.03)	0.16 (0.04)	0.16 (0.03)	
	Non-Myelinated Content (%)	0.46 (0.01)	0.48 (0.06)	0.45 (0.03)	0.54 (0.06)	
	Extracellular Space (%)	0.04 (0.02)	0.06 (0.02)	0.05 (0.02)	0.05 (0.03)	
	Myelinated Axons/ $100\mu\text{m}^2$	77 (1)	70 (15)	78 (21)	88 (6)	
	Myelinated Axons (%) + Myelin Sheaths (%)	0.50 (0.02)	0.47 (0.05)	0.51 (0.05)	0.41 (0.04)	
Myelinated Axon Diameters	Mean ( $\mu\text{m}$ )	0.44 (0.02)	0.51 (0.09)	0.44 (0.04)	0.47 (0.02)	
	<0.3 $\mu\text{m}$ (%)	0.25 (0.07)	0.21 (0.05)	0.27 (0.02)	0.19 (0.05)	
	0.3 - 0.45 $\mu\text{m}$ (%)	0.40 (0.10)	0.34 (0.08)	0.38 (0.07)	0.36 (0.04)	
	>0.45 $\mu\text{m}$ (%)	0.34 (0.03)	0.44 (0.10)	0.34 (0.06)	0.45 (0.08)	
Myelin Sheath Thickness	Mean ( $\mu\text{m}$ )	0.061 (0.003)	0.08 (0.02)	0.0590 (0.0002)	0.068 (0.006)	
	<0.06 $\mu\text{m}$ (%)	0.55 (0.09)	0.40 (0.14)	0.57 (0.02)	0.41 (0.11)	
	0.06 - 0.075 $\mu\text{m}$ (%)	0.26 (0.04)	0.24 (0.01)	0.24 (0.03)	0.26 (0.01)	
	>0.075 $\mu\text{m}$ (%)	0.19 (0.06)	0.36 (0.15)	0.19 (0.03)	0.33 (0.11)	
Ratios	g-Ratio	0.76 (0.01)	0.76 (0.01)	0.77 (0.01)	0.76 (0.01)	
	M/A Ratio	0.16 (0.01)	0.17 (0.01)	0.161 (0.001)	0.16 (0.01)	

cant difference existed in the myelinated axon fraction between groups at week 3 of feeding ( $p < .05$ ).

A non-significant decrease in the myelinated axon fraction and myelin sheath fraction (11% and 13%, respectively) from week 2 to week 3 was apparent in the cuprizone fed corpus callosum. The non-myelinated content fraction increased by 13% while the sum of the myelinated axon fraction and myelin sheath fraction decreased by 12% from week 2 to week 3. The mean myelinated axon diameter decreased from 0.51  $\mu\text{m}$  at week 2 to 0.47  $\mu\text{m}$  at week 3. The mean sheath thickness decreased from 0.077  $\mu\text{m}$  to 0.068  $\mu\text{m}$  between weeks 2 and 3 in the cuprizone fed mice with <0.02% change in the g-ratio and M/A (all changes statistically non-significant). A summary of EM cellular distributions and measurements can be found in Table 4.8.

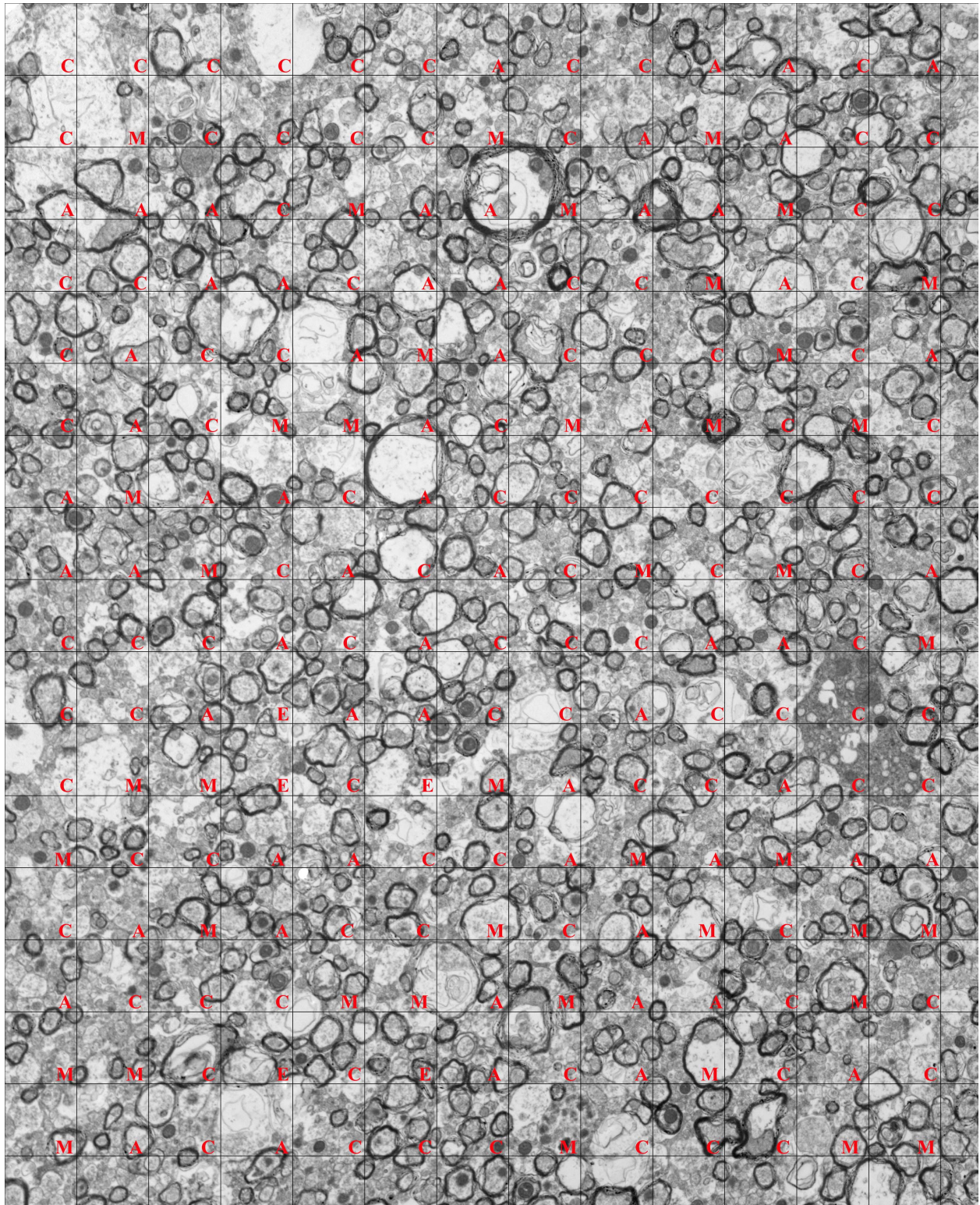


Figure 4.19: Sample 5000x EM image of a control mouse corpus callosum at week 2. Each point on the  $2 \times 2 \mu\text{m}$  grid was classified as either a myelinated axon (A), myelin sheath (M), non-myelinated content (C), or extracellular space (E). The non-myelinated content included unmyelinated cells, apoptotic cells, glial nuclei, glial processes and material in extracellular space.

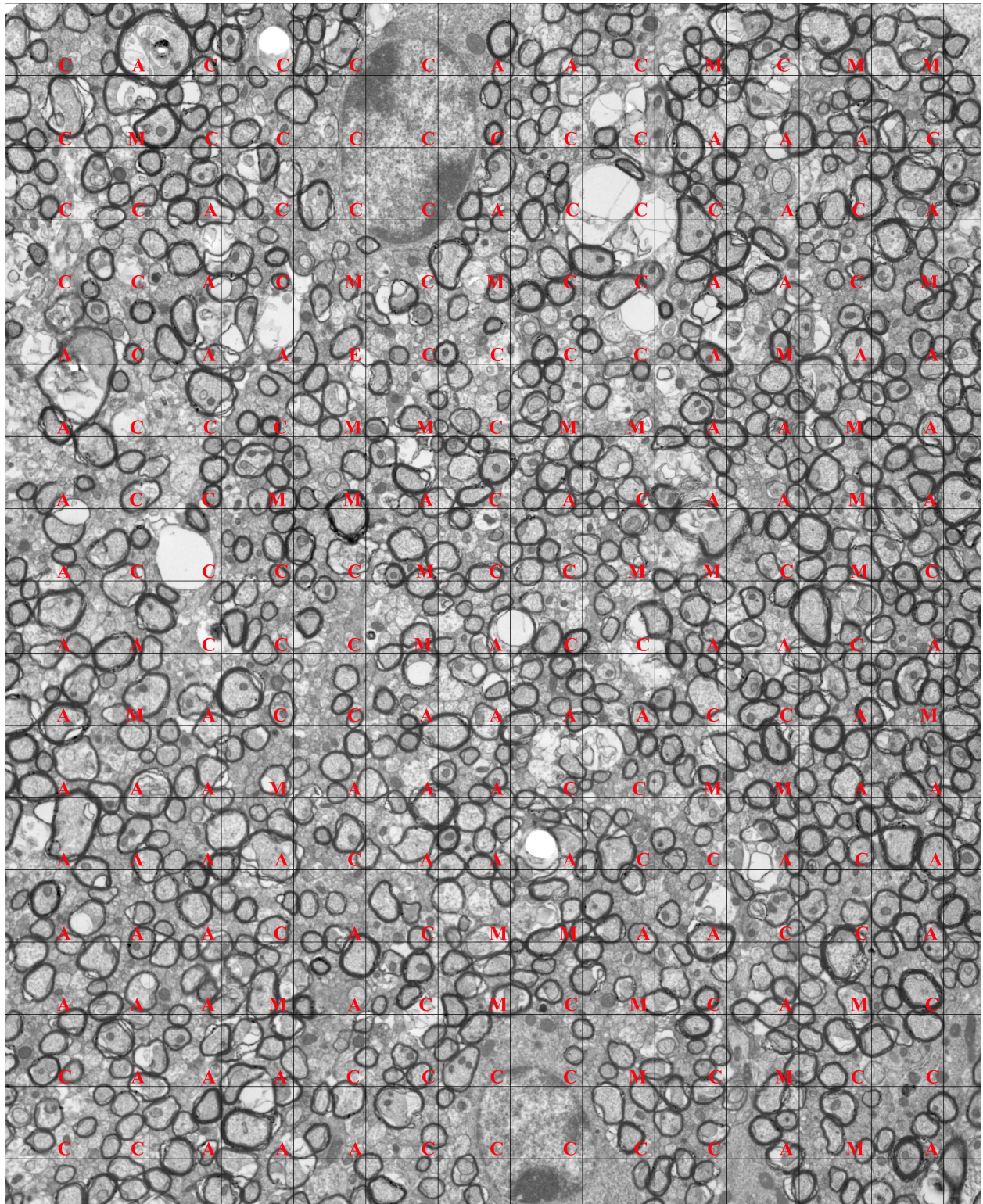


Figure 4.20: Sample 5000x EM image of a control mouse corpus callosum at week 3. Each point on the  $2 \times 2 \mu\text{m}$  grid was classified as either a myelinated axon (A), myelin sheath (M), non-myelinated content (C), or extracellular space (E). The non-myelinated content included unmyelinated cells, apoptotic cells, glial nuclei, glial processes and material in extracellular space. Apoptotic cells are indicated with asterisks.

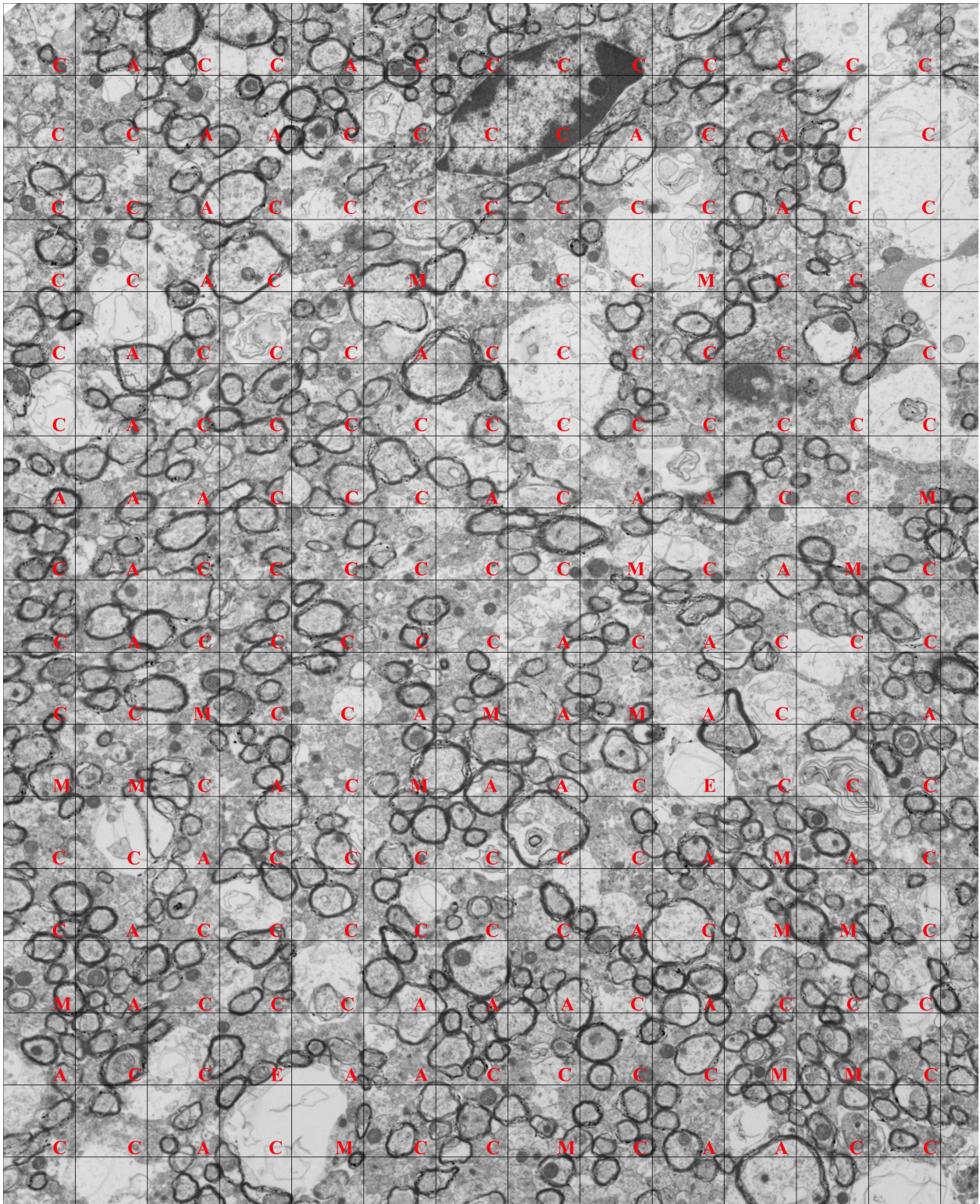


Figure 4.21: Sample 5000x EM image of a cuprizone fed mouse corpus callosum at week 2. Persistence of myelinated axons is apparent as well as apoptosis of oligodendrocytes and swelling of the glial processes. Each point on the  $2 \times 2 \mu\text{m}$  grid was classified as either a myelinated axon (A), myelin sheath (M), non-myelinated content (C), or extracellular space (E). The non-myelinated content included unmyelinated cells, apoptotic cells, glial nuclei, glial processes and material in extracellular space.

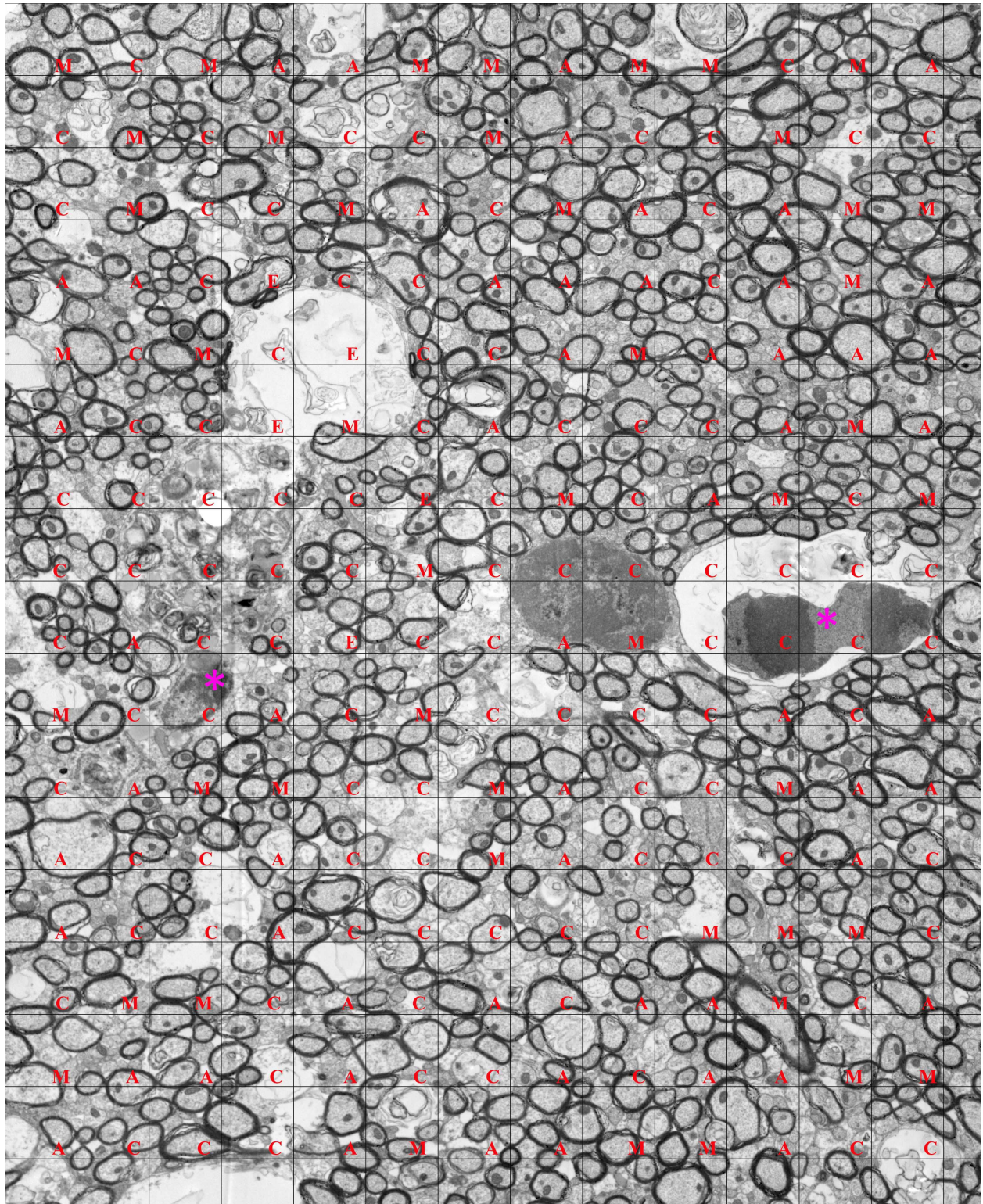


Figure 4.22: Sample 5000x EM image of a cuprizone fed mouse corpus callosum at week 3. Persistence of myelinated axons is apparent as well as apoptosis of oligodendrocytes, swelling of the glial processes and damage to the axons. Each point on the  $2 \times 2 \mu\text{m}$  grid was classified as either a myelinated axon (A), myelin sheath (M), non-myelinated content (C), or extracellular space (E). The non-myelinated content included unmyelinated cells, apoptotic cells, glial nuclei, glial processes and material in extracellular space.

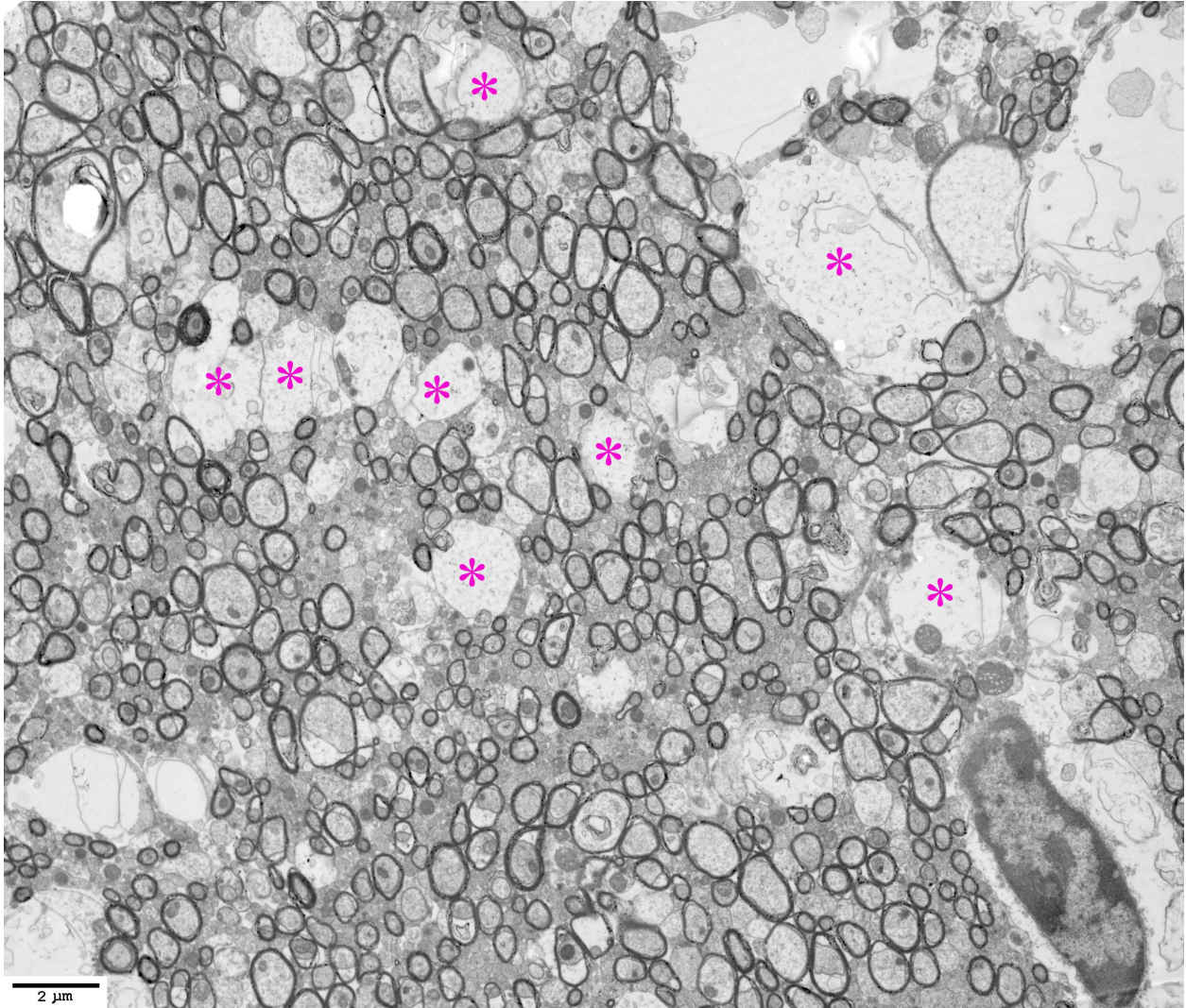


Figure 4.23: Sample 5000x EM image of a control corpus mouse callosum at week 3 displaying excess swelling of glial cell processes (asterisks).

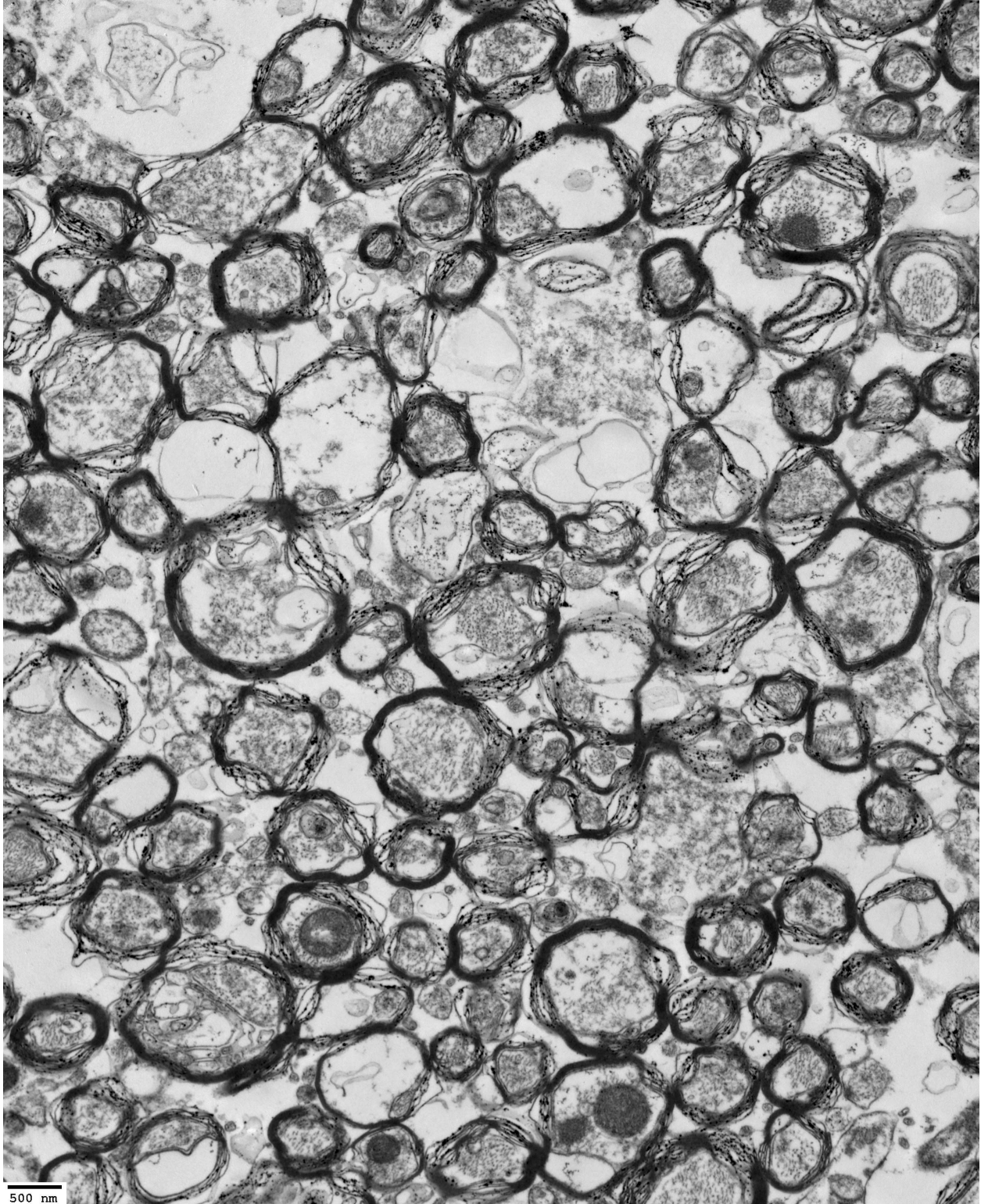


Figure 4.24: Sample 15 000x EM image of a cuprizone fed mouse corpus callosum showing fraying or disorganization of the myelin bi-layers at week 3. Normal appearing myelinated axons have uniform organized rings of myelin.

## 4.7 MRI and EM Correlations

Spearman and Pearson correlation coefficients were calculated between *in vivo*, *ex vivo*, and EM metrics for the subset of mice (n=2 control, 3 cuprizone for week 2, n=3 control, 3 cuprizone for week 3) that underwent EM analysis. Data from both weeks were combined for the control (n=5), cuprizone (n=6) and combined data sets (n=11). The combined data set was analyzed to include measurements with varying degrees of myelination at each week of the study to improve the power of these correlations.

### *Spearman Analysis*

The strongest Spearman correlation in the combined data set was found between  $R$  and the fraction of myelinated axons with diameters greater than  $0.45 \mu\text{m}$  ( $\rho=.85$ ,  $p<.01$ ). Myelinated axon fraction correlated with several MRI metrics including:  $\langle D \rangle$  ( $\rho=-.84$ ,  $p<.01$ ), normalized  $T_2$ -weighted signal intensity ( $\rho=-.80$ ,  $p<.01$ ),  $T_2$  ( $\rho=-.68$ ,  $p<.05$ ), and  $\lambda_{\parallel}$  ( $\rho=-.64$ ,  $p<.01$ ). Non-myelinated content fraction held weak correlations with  $\langle D \rangle$  ( $\rho=.53$ ) and MTR ( $\rho=-.49$ ) while only the correlation with normalized  $T_2$ -weighted signal intensity ( $\rho=.63$ ,  $p<.05$ ) was significant. The fraction of extracellular space correlated with  $R$  ( $\rho=.72$ ,  $p<.05$ ),  $T_2^A$  ( $\rho=.63$ ,  $p<.05$ ), and  $f$  ( $\rho=-.62$ ,  $p<.05$ ). When the fraction of myelinated axons was added to the fraction of myelin sheath, a weak correlation existed with  $\langle D \rangle$  ( $\rho=-.54$ ) while a more moderate correlation existed with normalized  $T_2$ -weighted signal intensity ( $\rho=-.64$ ,  $p<.05$ ). The number of myelinated axons per  $100 \mu\text{m}^2$  correlated with  $f$  ( $\rho=.55$ ) but was not significant. The fraction of myelinated axons with diameters less than  $0.30 \mu\text{m}$  held correlations with  $T_2$  ( $\rho=-.82$ ,  $p<.01$ ) and  $\lambda_{\perp}$  ( $\rho=-.60$ ,  $p<.05$ ). The fraction of myelinated axons with diameters between  $0.30$  to  $0.45 \mu\text{m}$  held moderate correlations with  $R$  ( $\rho=-.65$ ,  $p<.05$ ) and  $f$  ( $\rho=.62$ ,  $p<.01$ ) while the fraction of myelinated axons with diameters greater than  $0.45 \mu\text{m}$  held correlations with  $f$  ( $\rho=-.82$ ,  $p<.01$ ) and  $T_2^B$  ( $\rho=-.65$ ,  $p<.05$ ). The fraction of myelin sheaths less than  $0.06 \mu\text{m}$  in thickness had moderate correlations with  $f$  ( $\rho=.63$ ,

$p < .05$ ),  $\langle D \rangle$  ( $\rho = -.63$ ,  $p < .05$ ) and  $\lambda_{\parallel}$  ( $\rho = -.62$ ,  $p < .05$ ). The fraction of myelin sheaths greater than  $0.075 \mu\text{m}$  in thickness held these same correlations:  $f$  ( $\rho = -.64$ ,  $p < .05$ ),  $\langle D \rangle$  ( $\rho = .68$ ,  $p < .05$ ) and  $\lambda_{\parallel}$  ( $\rho = .65$ ,  $p < .05$ ).

### *Pearson Analysis*

Fewer correlations were apparent in the Pearson correlations suggesting many of the above correlations are not simply linear. Myelinated axon fraction was only found to correlate with normalized  $T_2$ -weighted signal intensity ( $r = -.75$ ,  $p < .05$ ) and  $T_2$  ( $r = -.68$ ,  $p < .05$ ). Non-myelinated content fraction held correlations with  $T_2^A$  ( $r = -.70$ ,  $p < .05$ ),  $T_2$  ( $r = .66$ ,  $p < .05$ ) and normalized  $T_2$ -weighted signal intensity ( $r = .65$ ,  $p < .05$ ). The fraction of extracellular space correlated with  $R$  ( $r = .78$ ,  $p < .01$ ),  $T_2^A$  ( $r = .74$ ,  $p < .01$ ), and  $f$  ( $r = -.77$ ,  $p < .01$ ). When the fraction of myelinated axons was added to the fraction of myelin sheath, moderate correlations existed with normalized  $T_2$ -weighted signal intensity ( $r = -.65$ ,  $p < .05$ ) and  $T_2$  ( $r = -.60$ ,  $p < .05$ ). The fraction of myelinated axons with diameters between  $0.30$  to  $0.45 \mu\text{m}$  and the fraction of myelinated axons with diameters greater than  $0.45 \mu\text{m}$  both held moderate correlations with  $f$  ( $r = .65$  and  $r = -.59$ , respectively) and with  $R$  ( $r = -.67$  and  $r = .67$ , respectively) with  $p < .05$  for all correlations.

A summary of Spearman correlation coefficients can be found in Table 4.9. Selected scatter plots for the MRI and EM correlations are shown in Figure 4.25 for the combined mouse data set.

Table 4.9: A summary of Spearman correlation coefficients ( $\rho$ ) of mean MRI metrics in the corpus callosum to EM measurements of the combined (n=11), control (n=5) and cuprizone fed (n=6) data sets from weeks 2 and 3 of the study. Values in bold are statistically significant where  $*p < 0.05$ ,  $**p < 0.01$ ,  $***p < 0.0001$

Metric	$f$	$R_A$	$R$	$T_2^A$	$T_2^B$	$\langle D \rangle$	$\lambda_{\parallel}$	$\lambda_{\perp}$	FA	$T_1$	$T_2$	$T_{2w}$	MTR
<b>Combined</b>													
Myelinated Axons	0.19	0.17	-0.07	0.09	0.08	<b>-0.84**</b>	<b>-0.64*</b>	-0.40	-0.13	-0.25	<b>-0.68*</b>	<b>-0.80**</b>	0.36
Myelin Sheaths	-0.15	0.32	0.07	0.25	-0.27	-0.15	-0.09	-0.06	-0.19	-0.28	-0.13	-0.28	0.29
Non-Myelinated Content	-0.04	-0.32	0.05	-0.10	0.05	0.53	0.38	0.25	0.14	0.38	0.49	<b>0.63*</b>	-0.49
Extracellular Space	<b>-0.62*</b>	0.29	<b>0.72*</b>	<b>0.63*</b>	-0.42	0.11	0.20	0.09	0.04	-0.06	-0.08	-0.19	0.46
Myelinated Axons/ $100\mu m^2$	0.55	-0.19	-0.50	-0.15	0.10	-0.08	-0.17	0.04	-0.11	0.03	0.23	0.23	0.09
Myelinated Axons + Myelin Sheaths	0.11	0.28	-0.14	0.05	-0.03	-0.54	-0.40	-0.26	-0.18	-0.36	-0.48	<b>-0.64*</b>	0.40
Axon Diameters $< 0.3 \mu m$	0.21	-0.09	-0.21	-0.45	0.31	-0.20	0.11	<b>-0.60*</b>	0.44	0	<b>-0.82**</b>	-0.25	-0.08
Axon Diameters $0.3 - 0.45 \mu m$	<b>0.62*</b>	-0.47	<b>-0.65*</b>	-0.25	0.49	-0.48	-0.46	0.03	-0.36	0.28	0.11	-0.09	-0.08
Axon Diameters $> 0.45 \mu m$	<b>-0.82**</b>	0.48	<b>0.85**</b>	0.46	<b>-0.65*</b>	0.52	0.44	0.23	0.14	-0.22	0.10	0.09	0.06
g-Ratio	0.29	-0.25	-0.26	-0.38	0.48	-0.25	-0.03	-0.31	0.26	0.16	-0.08	-0.05	-0.18
M/A Ratio	-0.45	0.26	0.45	0.32	-0.37	0.32	0.26	0.09	0.01	-0.13	-0.30	-0.18	0.25
<b>Control</b>													
Myelinated Axons	0.60	0.60	-0.20	-0.40	0.30	-0.70	-0.40	-0.30	0.10	-0.60	-0.20	-0.90	0.90
Myelin Sheaths	0.50	-0.10	-0.80	-0.40	0.30	0.00	0.10	-0.20	-0.10	0.10	0.50	-0.10	-0.50
Non-Myelinated Content	-1.00	-0.70	0.90	0.70	-0.40	0.50	0.20	0.60	-0.20	0.70	0.00	0.80	-0.50
Extracellular Space	-0.40	-0.10	0.70	-0.10	0.30	0.30	0.40	-0.20	0.50	0.10	-0.70	-0.10	0.40
Myelinated Axons/ $100\mu m^2$	0.10	0.40	-0.30	0.50	-0.80	-0.20	-0.50	0.30	-0.40	-0.40	0.30	0.40	-0.10
Myelinated Axons + Myelin Sheaths	0.90	0.50	-1.00	-0.60	0.30	-0.30	-0.10	-0.50	0.10	-0.50	0.20	-0.50	0.10
Axon Diameters $< 0.3 \mu m$	0.10	0.10	-0.20	-0.60	0.50	0.80	0.90	-0.80	0.90	-0.10	-0.70	-0.10	-0.10
Axon Diameters $0.3 - 0.45 \mu m$	0.20	0.00	0.00	0.20	-0.10	-0.90	-0.80	0.50	-0.70	0.00	0.60	-0.50	0.30
Axon Diameters $> 0.45 \mu m$	-0.60	-0.10	0.70	0.10	0.00	0.70	0.60	-0.20	0.60	0.10	-0.80	0.40	0.10
g-Ratio	-0.10	0.00	0.50	-0.10	0.30	-0.30	-0.10	0.00	0.10	0.00	-0.30	-0.50	0.60
M/A Ratio	-0.20	0.00	0.00	-0.20	0.10	0.90	0.80	-0.50	0.70	0.00	-0.60	0.50	-0.30
<b>Cuprizone</b>													
Myelinated Axons	-0.37	0.26	0.26	0.43	-0.26	-0.66	-0.37	-0.37	-0.03	-0.09	<b>-0.94*</b>	-0.26	0.83
Myelin Sheaths	-0.49	0.43	0.60	<b>0.94*</b>	-0.60	-0.49	-0.49	-0.20	-0.20	-0.31	-0.49	-0.83	0.83
Non-Myelinated Content	0.49	-0.26	-0.43	-0.77	0.43	0.54	0.49	0.14	0.31	0.09	0.77	0.60	<b>-0.89*</b>
Extracellular Space	-0.52	0.35	0.61	<b>0.99**</b>	-0.61	-0.14	-0.17	0.06	-0.38	-0.17	-0.23	<b>-0.93*</b>	0.64
Myelinated Axons/ $100\mu m^2$	0.77	-0.43	-0.60	-0.14	0.60	0.09	0.09	-0.26	0.26	0.37	0.31	0.31	0.14
Myelinated Axons + Myelin Sheaths	-0.49	0.26	0.43	0.77	-0.43	-0.54	-0.49	-0.14	-0.31	-0.09	-0.77	-0.60	<b>0.89*</b>
Axon Diameters $< 0.3 \mu m$	0.14	-0.03	-0.31	-0.54	0.31	-0.31	0.14	-0.43	0.43	0.09	-0.54	0.60	0.09
Axon Diameters $0.3 - 0.45 \mu m$	0.77	-0.66	<b>-0.89*</b>	-0.71	<b>0.89*</b>	0.03	0.09	-0.14	0.20	0.60	-0.03	<b>0.89*</b>	-0.09
Axon Diameters $> 0.45 \mu m$	-0.77	0.66	<b>0.89*</b>	0.71	<b>-0.89*</b>	-0.03	-0.09	0.14	-0.20	-0.60	0.03	<b>-0.89*</b>	0.09
g-Ratio	0.37	-0.09	-0.43	<b>-0.94*</b>	0.43	0.09	0.37	-0.26	0.60	-0.03	0.14	0.83	-0.60
M/A Ratio	-0.60	0.37	0.66	<b>1.00**</b>	-0.66	-0.20	-0.26	0.09	-0.43	-0.20	-0.31	<b>-0.94*</b>	0.66

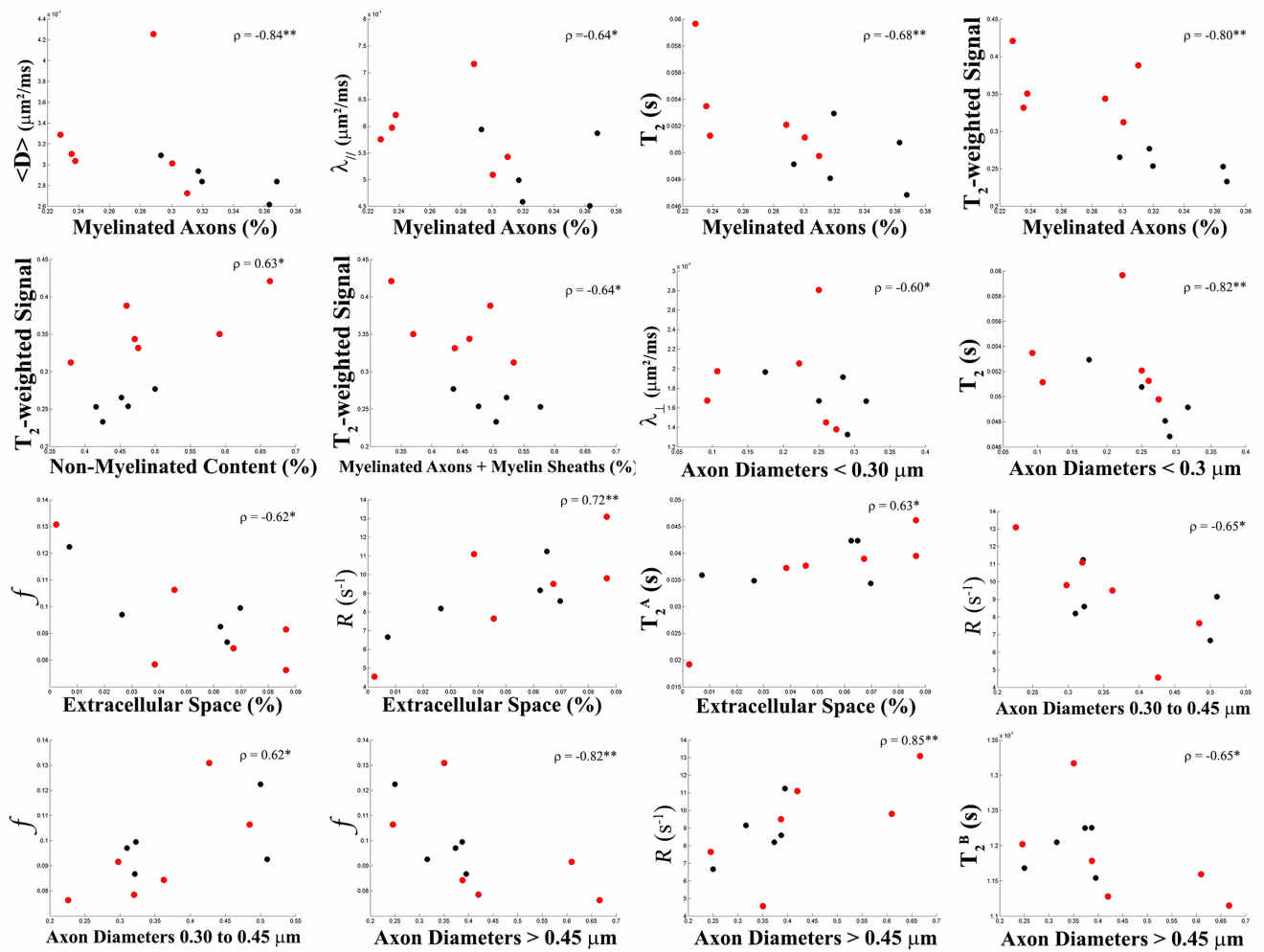


Figure 4.25: Selected scatter plots for the MRI and EM correlations in the corpus callosum of the combined data set at weeks 2 and 3. Black dots represent control mice measurements. Red dots represent cuprizone fed mice measurements. (Only combined data set correlations with significant coefficients are shown with  $*p < 0.05$ ,  $**p < 0.01$ ,  $***p < 0.0001$ ).

# Chapter 5

## Discussion

This study investigated how the ultrastructure of tissue affects MRI metrics during cuprizone induced demyelination with a focus on weeks 2 and 3 of feeding as explained below. A previous study examined the cuprizone mouse model during 6 weeks of feeding and found both *in vivo* normalized T<sub>2</sub>-weighted signal and the MTR began to show significant differences in the corpus callosum between groups at 3 weeks of feeding, but the T<sub>2</sub>-weighted signal difference peaked at 4 weeks whereas the MTR difference peaked at 5 weeks (2). Detailed EM tissue analysis was completed only at week 6 of feeding making it difficult to estimate the contributions cellular level changes have to MRI metric sensitivities. In the current study, the first and largest significant change in normalized T<sub>2</sub>-weighted signal in the corpus callosum of cuprizone fed mice occurred between weeks 2 and 3 while the small change in MTR was insignificant. Based on this, EM of control and cuprizone mice corpus callosa from weeks 2 and 3 was done to see how MRI is influenced by anatomical damage. The corpus callosum is most affected by the cuprizone treatment and therefore was the focus of this study. Data and tissue from the other ROIs previously mentioned are saved for analysis in future studies. As explained below, these ultrastructural examinations found increased swelling of glial cell processes rather than substantial demyelination at week 3 of cuprizone

feeding as well as confirmation of oligodendrocyte apoptosis, thus MRI can detect brain cell abnormality before demyelination begins in the corpus callosum.

## 5.1 Electron Microscopy

Apoptosis of oligodendrocyte nuclei along with extensive swelling of glial cell processes were visibly apparent at weeks 2 and 3 of cuprizone feeding. The majority of oligodendrocyte nuclei captured in the 5000x magnification EM images displayed signs of apoptosis at week 3 in the cuprizone fed corpus callosum consistent with studies observing almost complete mature oligodendrocyte depletion by week 3 of 0.3% (w/w) cuprizone feeding (29; 30; 31). These studies also reported the maximal number of apoptotic oligodendrocytes was reached at this same time point and confirmed the start of oligodendrocyte apoptosis 3-7 days after cuprizone feeding was initiated (3). Already at week 2 of feeding is when microglia and hypertrophic astrocytes with thick (and sometimes swollen) processes are known to appear and proliferate (termed astrogliosis). These glial cells, along with disorganization of the myelin bilayers were apparent beginning week 2 in the cuprizone fed mice which were not seen in control mice.

At 3 weeks of feeding, the fraction of myelinated axons decreased by 11% from week 2 and was significantly different from the control mouse fraction at the same week. Swelling of the glial cell processes seemed to distort the normal cell organization and occupy space axons otherwise would have occupied, decreasing the fraction of axons (myelinated or not) measured. This anomaly in the control mice is suspected to be what caused the differences in cellular fractions to be non-significant. Of the cuprizone fed mice analyzed through EM, 5 of them showed substantial swelling in the glial cell processes, compared to the 2 control mice.

Substantial demyelination has been observed by *Matsushima and Morell* at week 3 and more than 90% of axons were demyelinated by weeks 4-5 as assessed by ultrastructure, using a 0.02% (w/w) cuprizone mouse chow. Measured by immunohistochemistry, peak demyelination has been observed as early as week 4-4.5 (using CNPase- and MBP-antibodies) and week 5 (by PLP staining) (3; 32).

The degree of demyelination is known to vary among regions of the corpus callosum. Specifically the rostral region, imaged in this study, is less susceptible to demyelination (13; 33) which may explain the low degree of change in myelinated axon fraction and myelin sheath thickness found through EM of the tissue at weeks 2 and 3 of feeding.

Local and migrated oligodendrocyte precursor cells (OPCs) proliferate even while demyelination is occurring (between weeks 3-5) and begin differentiating to new mature oligodendrocytes at week 5 that go on to remyelinate axons. Up to 50% of axons have been reported to be remyelinated in week 6 of 0.2% (w/w) cuprizone feeding (34). This process occurs after demyelination is complete, even if cuprizone feeding continues past 5 weeks (3; 34). The number of activated microglia begins to decline after week 5 while astrogliosis continues for a number of weeks once cuprizone feeding has stopped (3).

## 5.2 *In vivo* MRI and EM

Normalized T<sub>2</sub>-weighted signal intensity images show signal inversion in the corpus callosum of the cuprizone fed mice in response to the cuprizone treatment, beginning as early as week 2 of cuprizone feeding. The non-significant increase in myelinated axons might be due to one cuprizone mouse who EM slide showed larger axons than the other mice. It is possible that a slightly more posterior section toward the genu of the corpus callosum was imaged with EM in the mouse with larger axons compared to the other mice and the MRI.

Significant increases in the normalized T<sub>2</sub>-weighted signal intensity remained throughout the study between groups.

The correlation between normalized T<sub>2</sub>-weighted signal and myelinated axon fraction as well as between the normalized T<sub>2</sub>-weighted signal and myelinated axon + myelin sheath fraction that existed at week 6 (2) also existed at weeks 2 and 3. These time points correspond to when demyelination begins to occur and when it is deemed to be substantial, respectively.

The correlation of normalized T<sub>2</sub>-weighted signal and non-myelinated content apparent in the previous study at week 6 of cuprizone feeding remained at weeks 2 and 3 of feeding in this study. Tissue cellularity begins to increase at week 2 and substantially increases at week 3 of feeding marked by increased number of astrocytes and microglia (3). The first and largest significant week-to-week increase found in the normalized T<sub>2</sub>-weighted signal of the cuprizone corpus callosum is in parallel to these cellular feature changes.

The existence of these correlations at weeks 2 and 3 increases the power of these previously found correlations at week 6. This is important because at weeks 2 and 3, the range of pathologies is greater than what is apparent at week 6, suggesting normalized T<sub>2</sub>-weighted signal changes reflect cellularity changes while demyelination is occurring and when it is complete.

MTR had a small although non-significant increase from weeks 2 to 3 in the corpus callosum of the cuprizone fed mice and showed no correlation with tissue features relating to myelin or myelinated axons during the first weeks of cuprizone feeding. This suggests that the normalized T<sub>2</sub>-weighted signal is sensitive to early changes in tissue pathology, specifically increase in tissue cellularity and slight decreases in myelin content whereas MTR is not. The first and largest significant week to week change in MTR in the cuprizone fed corpus callosum occurred between weeks 3 and 4. The decreases continue to week 5 where it reached its peak

value. It is between weeks 3.5 to 5 where demyelination is found to be most severe (3) with peak demyelination occurring at week 5 (34). MTR decreases and severe demyelination processes appear to mirror each other. This may suggest why no correlations were apparent between MTR and myelinated axon fraction, myelin sheath fraction or the sum of the two in the current study where correlations were made during early demyelination. This also is in agreement with previous studies (2; 19) that hypothesized MTR reflects demyelination.

As mentioned above, both the normalized T<sub>2</sub>-weighted signal intensity and MTR reached peak values at week 5 of feeding. This time point corresponds to peak demyelination and consequently peak activation of microglia and astrogliosis and peak OPC numbers (3; 34; 35). Histology will be completed throughout the 6 week *ex vivo* study to determine relationships between MRI metrics and glial activation or OPC numbers as part of a future students project. Both the normalized T<sub>2</sub>-weighted signal intensity and MTR deflect from their peak values at week 5 in the corpus callosum of the cuprizone fed mice which may reflect the appearance of new mature oligodendrocytes and the processes of remyelination (3).

### 5.2.1 Normalized T<sub>2</sub>-weighted Signal and MTR Correlations

The initial weak voxel based correlations between normalized T<sub>2</sub>-weighted signal and MTR in the CC, EC and CC+EC of the combined data set at weeks 0-3 reflect how the 2 methods are not sensitive to the same pathological features during the beginning of cuprizone feeding. Specifically the appearance and activation of microglia and astrocytes (increased cellularity), the start of oligodendrocyte apoptosis, peak apoptotic oligodendrocyte numbers, and early demyelination all appear to have some effect on normalized T<sub>2</sub>-weighted signal but not MTR. The preceding moderate correlations at weeks 4-6 between normalized T<sub>2</sub>-weighted signal and MTR of the combined data set reflect how the two methods show similar sensitivities to pathological features once the processes of severe to complete demyelination begin. Peak

microglia activation and astrogliosis, differentiation of OPCs to new mature oligodendrocytes and remyelination towards the end of cuprizone feeding are all processes occurring that change myelin content, tissue structure and water mobility after weeks 3 of feeding. EM and tissue staining will be completed at weeks 4 and 5 to separate these pathological processes in a future study.

These *in vivo* results suggest longitudinal measurements of normalized  $T_2$ -weighted signal and MTR would be useful in determining the amount of demyelination occurring as well as the effectiveness of treatments working to stop further demyelination.

## 5.3 *Ex vivo* MRI and EM

### 5.3.1 Relaxometry

#### $T_1$ Measurements

The measured  $T_1$  relaxation times from this study ( $1360 \pm 50$  ms for control and  $1514 \pm 2$  ms for cuprizone-fed) are higher than the measured times in the corpus callosum of control ( $1350 \pm 7$  ms) and cuprizone fed mice ( $1496 \pm 7$  ms) measured at week 6 in the previous study which followed the same imaging protocols (2). The previous study used a higher concentration of cuprizone (0.4%, w/w) and followed a different schedule of bringing tissues to the same temperature before imaging. Temperature is known to effect self-diffusion in free water (36) and its dependence on diffusion in tissue is complicated (2). Thus temperature changes can affect relaxometry as well as diffusion measurements in lengthy *ex vivo* imaging studies (37; 38; 39). The previous study (2) demonstrated tissue temperatures were likely higher than the ambient temperature in the bore ( $18^\circ\text{C}$ ) during overnight imaging, but were assumed to drift

approximately 0.2°C/hour between 6 and 12 hours of imaging. Although this temperature change may contribute a small error in DTI and relaxometry measurements, it is consistent across *ex vivo* experiments from the same week. This error should be considered when comparing week to week relaxometry and diffusion measurements as well as relaxometry and diffusion measurements from other studies where the time prior to *ex vivo* imaging may be different.

It is also useful to keep in mind when comparing measurements and combining MRI data that other factors beyond temperature changes which include magnetic field strength, *in vivo* vs *ex vivo* conditions, tissue fixation processes and durations, the region of the corpus callosum imaged as well as subtleties in the preparation of the cuprizone diet, to name a few all introduce variability.

$T_1$  increases with field strength (2; 40) as well as with increased water mobility as in cases of demyelination, inflammation, gliosis, edema and axonal loss (1; 2).  $T_1$  did increase when comparing measurements from the first 4 weeks of feeding to the last 2 weeks of feeding in the CC and EC of cuprizone fed mice. The strong correlation that existed between  $T_1$  and myelinated axon fraction at week 6 (2; 15) did not exist at weeks 2 and 3. This may be contributed to the small change in myelinated axon fraction, and thus small change in water mobility, between weeks 2 and 3 as well as between groups. A comparable amount of myelinated axons remained in the cuprizone fed mice and control mice at weeks 2 and 3 of feeding.

## **$T_2$ Measurements**

The mono-exponential  $T_2$  relaxation times were also higher than measurements made in the previous study in the corpus callosum of control and cuprizone fed mice (19). Problems with the echo signal amplitude explained in section 4.4.1 may explain this discrepancy.

One might expect that the mono-exponential  $T_2$  carried more weight from the intra-/extra cellular water fraction than from the decrease in myelinated axon + myelin sheath fraction given the increase in intracellular water from the larger swollen processes and the relatively smaller change in myelin water, thus increasing  $T_2$  values. Yet the latter seems to be true which is supported by the correlation between myelinated axon fraction and  $T_2$  found through *ex vivo* analysis of the tissue.

A recent review on the various imaging techniques that have been used to image MWF (41) concluded that not only is MWF imaging a strong candidate for assessing changes related to myelin but it is specifically a reliable marker for myelin. Previous studies have found good reproducibility of MWF imaging (42) and have found strong correlations between MWF and myelin stain (used a measure for myelin density) in human postpartum MS brain samples (41; 43). The calculated MWF in this study was essentially zero in the whole slice of the mouse brain under examination consistent with other measurements of MWF in the mouse brain at this field strength (2) making correlations with EM measurements infeasible. This is most likely due to the thinner myelin sheaths in the corpus callosum and/or insufficient amount of myelin water present in the white matter tracts of the mouse brain causing increased intercompartmental exchange (19).

### 5.3.2 DTI

$\langle D \rangle$  values at week 6 of feeding are in agreement with values ( $0.375 \pm 0.009 \mu\text{m}^2/\text{ms}$ ) in the corpus callosum of the cuprizone fed mice from the previous study (2).

The peak values of  $\langle D \rangle$  and  $\lambda_{\perp}$  (at weeks 3 and 5) correspond to the time points where first the maximal amount of apoptotic oligodendrocytes was apparent and then where complete demyelination has been known to be reached (3; 34; 44; 45). Astrogliosis is also

known to peak around the time point of maximal demyelination (3; 45).

Inflammation, edema and swelling as well as decreased cellularity are known to increase  $\langle D \rangle$  (2; 17). There was no significant change in diffusion tensor metrics in the corpus callosum of the control mice suggesting the excess swelling seen in the control EM images may be an artifact of fixation or post imaging conditions (the delay in EM analysis). This suggests the excess swelling seen in the tissue of the control and cuprizone fed mice may have occurred after imaging and may be attributed to the delayed EM analysis. This also suggests largest week to week increase in  $\langle D \rangle$  which occurred between weeks 2 and 3 in the corpus callosum of the cuprizone fed mice may be attributed to true pathology such as astrocytes that have become gemistocytic or anatomical damage such as vacuolated swollen axons or vasogenic edema.

Weekly changes of less than 6% occurred after week 3 suggesting  $\langle D \rangle$  is less sensitive to severe demyelination or that the change in extracellular tortuosity during the first weeks of cuprizone feeding persists throughout the remainder of weeks. Other studies on the effects of microscopic tissue parameters on DTI metrics found that demyelination reduces the tortuosity of the extracellular space subsequently increasing  $\langle D \rangle$  (46; 47). The strong negative correlation between  $\langle D \rangle$  and myelinated axon fraction found here was also found using data at week 6 (19). This may help confirm that water mobility does in fact increase as a result of extracellular tortuosity changes from the decrease in myelinated axon fraction.

$\lambda_{\perp}$  and FA did not correlate with myelin fraction as *Thiessen et al.* (2) found at week 6. This may be due to the small and insignificant changes in myelin fraction in the control and cuprizone fed mice between weeks 2 and 3.

*In vivo*  $\lambda_{\parallel}$  has been shown to decrease during the initial stages of demyelination (after 4 weeks of 0.2% w/w cuprizone) in the corpus callosum (13; 15; 48) and during the early

stages of axonal injury in the optic nerve after ischemia (12). This decrease is thought to be attributed to axonal swelling and beading supported by electron microscopy and immunohistochemistry of the tissue (13). *Xie et al.* also suggested decreases in  $\lambda_{\parallel}$  may be attributed to the presence of microglia and macrophages. Larger swollen axons (with large vacuoles) as well as microglia are apparent in EM images of the cuprizone fed mice at weeks 2 and 3.

This study is the first to our knowledge to show a significant increase in *ex vivo* DTI derived  $\lambda_{\parallel}$  from week 1 through week 4 of cuprizone treatment. Values at weeks 3 and 4 remained unaltered or increased non-significantly in other studies (14; 15). It is hypothesized the changes caused by PFA fixation, such as increases in membrane permeability, may reduce the effects axon pathology has on *in vivo* radial diffusivity (15).

The negative correlation found between  $\lambda_{\parallel}$  and myelinated axon fraction at week 6 of cuprizone feeding (2) existed at weeks 2 and 3 although it was not as strong. In the experimental autoimmune encephalomyelitis (EAE) model,  $\lambda_{\parallel}$  was highly correlated with axonal damage although the authors found the specificity of  $\lambda_{\parallel}$  to axonal damage may be reduced in the presence of inflammation (11).

### 5.3.3 qMTI

The overall decrease in  $R_A$  and  $f$  along with the increase in  $T_2^A$  in the corpus callosum of the cuprizone fed mice were expected although the changes in  $f$  and  $T_2^A$  were not significant.

Mean  $R_A$  values in the corpus callosum of control mice ( $0.69 \pm 0.03 \text{ s}^{-1}$ ) agreed within error with previously measured values (2) while values in the cuprizone fed mice were slightly shorter ( $0.632 \pm 0.004 \text{ s}^{-1}$ ) than previously measured values. The largest consecutive week

to week decrease in  $R_A$  in the cuprizone-fed corpus callosum occurred between weeks 2 and 3 but no significant correlations were apparent between  $R_A$  and EM cellular distributions or measurements.

The strong correlation between the metrics  $T_1$  and  $R_A$  and the myelinated axons fraction that existed in the previous study (2) was not apparent when considering EM cellular distributions or measurements during weeks 2 and 3 of cuprizone feeding. The small change in myelinated axon fraction and thus the number of myelinated axons per  $100 \mu\text{m}^2$  may not have altered water mobility or the surrounding lattice of macromolecules enough to have an influence on these metrics.

The bound pool fraction,  $f$ , agreed with previously measured values in the corpus callosum of control and cuprizone fed mice at week 6 and has been suggested to be the most consistent and relevant qMTI metric for myelin content (19). A weak correlation between  $f$  and myelinated axons per  $100 \mu\text{m}^2$  existed. Direct correlation to myelin content was not found as it was in *Thiessen et al.*'s study who reported the strongest correlation to myelin sheath fraction was with  $f$ . Several other studies have reported correlations between  $f$  and myelin content as well (49; 50). The lack of correlation in this study may be contributed to the relatively small change in myelin content between weeks 2 and 3 when compared to the change in myelin content that would be apparent if measured between weeks with larger separation.

The measured  $T_2^A$  from the last 3 weeks of cuprizone feeding did not change significantly from the first 2 weeks of cuprizone feeding although an overall increase was apparent as well as a significant difference between the groups at week 6. Comparison of calculated  $T_2^A$  values as well as its interpretation of its changes is difficult due to its dependence on the pulse sequence parameters as well as the model used to estimate its value (51).  $T_2^A$  values from this experiment were slightly shorter than values from the previous study (2) which used the

same MTI pulse sequence as well as estimation method. The previous study used 0.4% (w/w) cuprizone and may have caused more extensive demyelination at week 6 of feeding.

$T_2^B$  values in the corpus callosum of the cuprizone fed mice agreed with previous measurements at week 6 feeding (2) and only a correlation between it and the fraction of axons with diameters greater than  $0.45 \mu\text{m}$  existed. It has been reported that  $T_2^B$  can be accurately estimated and compared regardless of the estimation model (51).

Like  $T_2^A$ ,  $R$  has high variability in tissue based on the imaging protocol and estimation method (2; 51).  $R$  values measured in this study in the corpus callosum of control and cuprizone fed mice at week 6 were smaller than previously measured values which used the same FLASH sequence although a lower concentration of cuprizone in the diet (2). Insignificant week to week changes in the CC of cuprizone fed mice are supported by studies that have demonstrated  $R$  has low sensitivity to white matter pathology (51; 52).

Two of the three control mice at week 1 had saturation pulse images that contained high frequency noise contaminating  $k$ -space. The sinebell filter failed to remove this noise so as another solution, abnormally high points in  $k$ -space were zeroed. The data was Fourier transformed once again, registered to the reference image, and qMTI metrics were recalculated with these new filtered images in place of the ones with the artifacts. Most of the qMTI metrics calculated from these two mice remained abnormal and so qMTI metrics were recalculated a last time omitting the 2 contaminated images. The qMTI metric maps from these 2 control mice were removed from all analysis after both attempts failed to fix the problem. Comparisons with week 1 control qMTI metrics should be taken with caution since the group only contained measurements from 1 mouse.

qMTI metrics in the cuprizone and even control mice fluctuated throughout the 6 weeks of *ex vivo* imaging.  $T_2^A$  and  $R$  are sensitive to noise and the fitting model while  $R_A$ ,  $f$ , and  $T_2^A$  are dependent on the calculated  $T_1$  map.

Correlations between the distribution of myelinated axon diameters, myelin sheath thickness and M/A ratio may not be meaningful because many of the myelinated axons in the cuprizone fed mice had regions of myelin along the ring that were frayed, separated or disorganized (Figure 4.24). The measurements were taken in regions where the myelin was most compact. This then assumes the axons were surrounded by full and uniform rings of myelin.

## 5.4 MRI Metric Correlations

Determining the relationship between different MRI metrics as they change with white matter damage may help to improve the interpretation of clinical MRI results. Correlations between MRI metrics were made using the mean ROI values and individual voxel values in the corpus callosum + external capsule combined data set. This was done to see if correlations made at week 6 in the previous study (2), when severe demyelination was apparent, still hold when data from all the weeks with the full range of pathological processes in the cuprizone mouse is analyzed.

Voxel based correlations give more meaningful results than ROI based correlations because the latter may naively assume the average characteristics of the region accurately reflect pathology in individual voxels (2). Based on this, voxel based correlations are discussed in further detail.

$f$  was found to correlate moderately with the number of myelinated axons per  $100\mu\text{m}^2$  (although not significantly) as well as with the extracellular space fraction (indicative of vasogenic edema). As described in section 2.3.4,  $f$  is sensitive to protons contained in myelin and is expected to correlate strongly with myelin content as it did in previous studies (2). The correlation of other MRI metrics to  $f$  may then reveal or confirm their sensitivities to myelin

content and integrity as well as vasogenic edema. Considering ROI based correlations, strong correlations remained between  $f$  and  $R_A$  and  $f$  and  $R$  with the addition of  $f$  and  $T_2^B$  and  $f$  and  $T_2$  when considering the full range of pathology compared to only the pathology present at week 6 from the previous study. Many strong correlations at week 6, from the previous study, were decreased to moderate or weak correlations when the full range of pathology was considered. These correlations include  $T_2^A$ ,  $\langle D \rangle$ ,  $\lambda_{\perp}$ , FA, and  $T_1$  with  $f$ . This suggests that  $f$  may be the only qMTI metric needed to investigate myelin content in longitudinal studies while the lack of correlation with DTI and  $T_1$  measurements suggest they provide complementary information on tissue pathology outside of myelin content.

$\langle D \rangle$  did not hold strong correlations with any other MRI metric in the voxel based or ROI based analysis. This suggests  $\langle D \rangle$  follows a different time line than relaxometry and qMTI metrics during the course of cuprizone feeding and may provide additional insight into pathology such as edema, inflammation, demyelination and cellular swelling.

The change in lattice size and water mobility reflected by  $T_1$  increases are also reflected by decreases in FA shown by the correlation the 2 MRI metrics share. The strong correlation between  $T_2$  and  $T_2^A$  supports the idea that the mono-exponential  $T_2$  is more heavily influenced by intra/extra cellular water fraction than the relatively small change in myelin water.

# Chapter 6

## Conclusion and Future Studies

In summary, this thesis developed and applied MRI methods and imaging analysis techniques to the cuprizone mouse model of MS to improve the specificity of MRI and to make steps towards bridging the gap between white matter damage detected in clinical images and clinical status associated with MS. White matter changes were investigated by developing and adapting analysis code in MATLAB. Multiple metrics spanning various MR methods sensitive to different tissue structures and content were used to quantify the white matter changes shown in the images and were correlated to microstructural changes found through electron microscopy tissue analysis.

*In vivo* normalized  $T_2$ -weighted signal intensity and MTR were found to follow a different time course although they both peaked at week 5 of cuprizone feeding. The weak correlation between the normalized  $T_2$ -weighted signal intensity and MTR in the corpus callosum + external capsule of the combined data set at weeks 0-3 reflect how the 2 methods are not sensitive to the same pathological features during the beginning of cuprizone feeding. Specifically the appearance and activation of microglia and astrocytes (increased cellularity), the start of oligodendrocyte apoptosis, peak apoptotic oligodendrocyte numbers, and

early demyelination all appear to have some effect on normalized T<sub>2</sub>-weighted signal but not MTR. T<sub>2</sub>-weighted signal intensity correlated with non-myelinated content (tissue cellularity) as previously hypothesized although MTR was not found to correlate with any of the EM measurements or distributions related to myelin at weeks 2 and 3 of feeding.

The *ex vivo* MRI metrics at weeks 2 and 3 lacked the correlations with EM metrics that were present at week 6 of the previous study (2). The relatively small change in myelinated axon fraction, myelin fraction and non-myelinated content fraction between weeks 2 and 3 and between groups compared to the large change in these fractions between groups at week 6 of cuprizone feeding is thought to contribute to the lack of correlation.

When *ex vivo* MRI data from weeks 1-6 containing the full range of pathological features of the cuprizone model were included in MRI metric correlations, few strong correlations were present. This suggested that metrics from each imaging method are in fact needed to provide complementary information on tissue pathology throughout a longitudinal study. Specifically, it was found that  $f$  may be the only qMTI metric needed to accurately assess myelin content (based on the number of myelinated axons per  $100\mu\text{m}^2$ ) and that T<sub>2</sub> is more heavily influenced by intra/extra cellular water fraction than a relatively small change in myelin water.

The quantitative MRI analysis methods developed in this project contribute to the biomedical engineering community by enabling others in the Martin lab the ability to analyze, quantify and compare MRI data for a variety of white matter diseases.

#### *Future Studies*

The imaging methods and analysis code developed in this project are ready to be used by other members of the Martin lab in various types of projects described below. Histology and ultrastructural examination will be completed by a future student on tissue from the remaining weeks of this study to determine relationships between MRI metrics and pathol-

ogy when a possibly different set of pathological features are present, specifically increased glial activation, increased oligodendrocyte precursor cell proliferation and differentiation and intermediate to severe demyelination. This further examination into the tissue at remaining weeks can also confirm if there were problems with fixation or storage of the tissue until EM analysis after *ex vivo* imaging and improve the power of the correlations made at weeks 2 and 3 in this study, as well as at week 6 in the previous study (2).

Improvements to the study that should be considered for future studies include the timing of fixation and the amount of time between sacrifice and EM, better slice alignment that considers the position of the anterior commissure and the possibility of choosing a different area in the corpus callosum for examination. To investigate how time and fixative duration influence MRI measurements, imaging directly after *ex vivo* imaging as well as directly before EM analysis would need to be completed. The anterior commissure is another white matter structure in the brain that is present in some, but not all of the *ex vivo* images in this study due to the focus on the corpus callosum and is also thought to be affected by the cuprizone treatment (53). The splenium region of the corpus callosum has been reported to be more severely affected by the cuprizone treatment than the central, rostral and ventral genu of the corpus callosum (53; 54).

To ensure consistent image results, a tube of water could be imaged simultaneously with *ex vivo* tissue samples. Changes in the signal from the water would indicate problems with the setup, methods used or MRI system.

Temperature changes of the tissue samples during long imaging sessions could be corrected by allowing all tissue samples to equilibrate to the temperature in the bore of the magnet for a longer period prior to imaging.

It is also important to remember that fixation, temperature difference, changes in membrane permeability and the cease of cellular and axon transport all affect *ex vivo* MRI tissue

measurements thus causing *in vivo* and *ex vivo* measurements to differ, specifically in DTI (2; 53; 54; 55). Much research has been done to study these differences (12; 15; 56; 57; 58; 59). Future studies could include full *in vivo* analysis for direct correlation comparisons although the resolution of the images would need to be drastically reduced to limit the time between *ex vivo* imaging and tissue analysis.

The cuprizone mouse model was chosen to apply these MRI methods and analysis techniques to due to the reproducibility of its de- and re-myelination in the corpus callosum as well as the simplicity of disease induction. The time course of demyelination and re-myelination is well studied as is the locations cuprizone causes severe demyelination. Future directions for this study would be applying these same methods to more complex disease models containing greater pathological features. Such models include the lysolecithin model which causes a demyelinating disease course in the spinal cord and corpus callosum lasting approximately 1 month following injection of lysophosphatidylcholine. Another commonly studied model is the experimental autoimmune encephalomyelitis (EAE) which causes blood brain barrier breakdown, inflammation, optic neuritis, vascular changes, functional changes, changes in metabolites, and those included in the cuprizone model. This model displays the same paradox as in MS: the damage captured in MR images does not always correlate with clinical symptoms (17; 60).

White matter pathology outside of MS can be studied using these MRI methods and analysis techniques including schizophrenia, epilepsy, Parkinsons disease, Alzheimers disease and various types of brain tumors. The latter two of these have most recently been completed using DTI measurements in our lab.

# Appendix A

## List of Acronyms

MRI	magnetic resonance imaging
MS	multiple sclerosis
$\mu$	magnetic dipole moment
<b>I</b>	spin angular momentum
$m$	magnetic quantum number
$\mathbf{B}_0$	external magnetic field vector
$\gamma$	gyromagnetic ratio
<b>M</b>	net magnetization vector
$M_z$	longitudinal component of magnetization
$M_{xy}$	transverse component of magnetization
$\omega_0$	Larmor frequency
RF	radio-frequency
$\mathbf{B}_1(t)$	applied magnetic field
FID	free induction decay
$T_2$	transverse relaxation time
$T_2w$	$T_2$ -weighted image

PD proton density image  
CSF cerebral spinal fluid  
 $T_1$  longitudinal relaxation time  
PEG,  $G_y$  phase encode gradient  
FEG,  $G_x$  frequency encode gradient  
FOV field of view  
 $FT$  Fourier Transform  
 $T_E$  echo time  
 $T_{Eff}$  effective echo time  
 $T_R$  repetition time  
CPMG Carr-Purcell Meiboom-Gill  
RARE Rapid Acquisition with Relaxation Enhancement  
PGSE pulsed gradient spin echo  
FLASH Fast Low Angle Shot  
MSME Multi-Slice Multi-Echo  
DTI Diffusion tensor imaging  
 $b$  diffusion weighted factor  
ADC apparent diffusion coefficient  
 $\langle D \rangle$  mean diffusivity  
 $\lambda_{\parallel}$  axial diffusivity  
 $\lambda_{\perp}$  radial diffusivity  
FA fractional anisotropy  
RGB red-green-blue  
qMTI quantitative magnetization transfer imaging  
 $M_0^A$  equilibrium magnetization of the liquid pool  
 $M_0^B$  equilibrium magnetization of the bound pool  
 $R_A$  longitudinal relaxation rate of the liquid pool

$T_1^A$  longitudinal relaxation time of the liquid pool  
 $T_1^B$  longitudinal relaxation time of the bound pool  
 $T_2^A$  transverse relaxation time of the liquid pool  
 $T_2^B$  transverse relaxation time of the bound pool  
 $R$  magnetization transfer rate  
 $MTR$  magnetization transfer ratio  
 $f$  bound pool fraction  
 $mcT_2$  multicomponent transverse relaxation time  
MWF myelin water fraction  
IEWF intra-/extracellular water fraction  
CTL control mice  
CPZ cuprizone-fed mice  
AC anterior commissure  
CC corpus callosum  
EC external capsule  
PBS phosphate buffered saline  
PFA paraformaldehyde  
ROI region of interest  
GUI graphical user interface  
EM electron microscopy  
A myelinated axons  
M myelin sheaths  
C non-myelinated content  
E extracellular space  
ANOVA analysis of variance  
SEM standard error of the mean  
SD standard deviation

$\rho$  Spearman's correlation coefficient

$r$  Pearson's correlation coefficient

OPCs oligodendrocyte precursor cells

EAE experimental autoimmune encephalomyelitis

# Appendix B

## Additional Figures

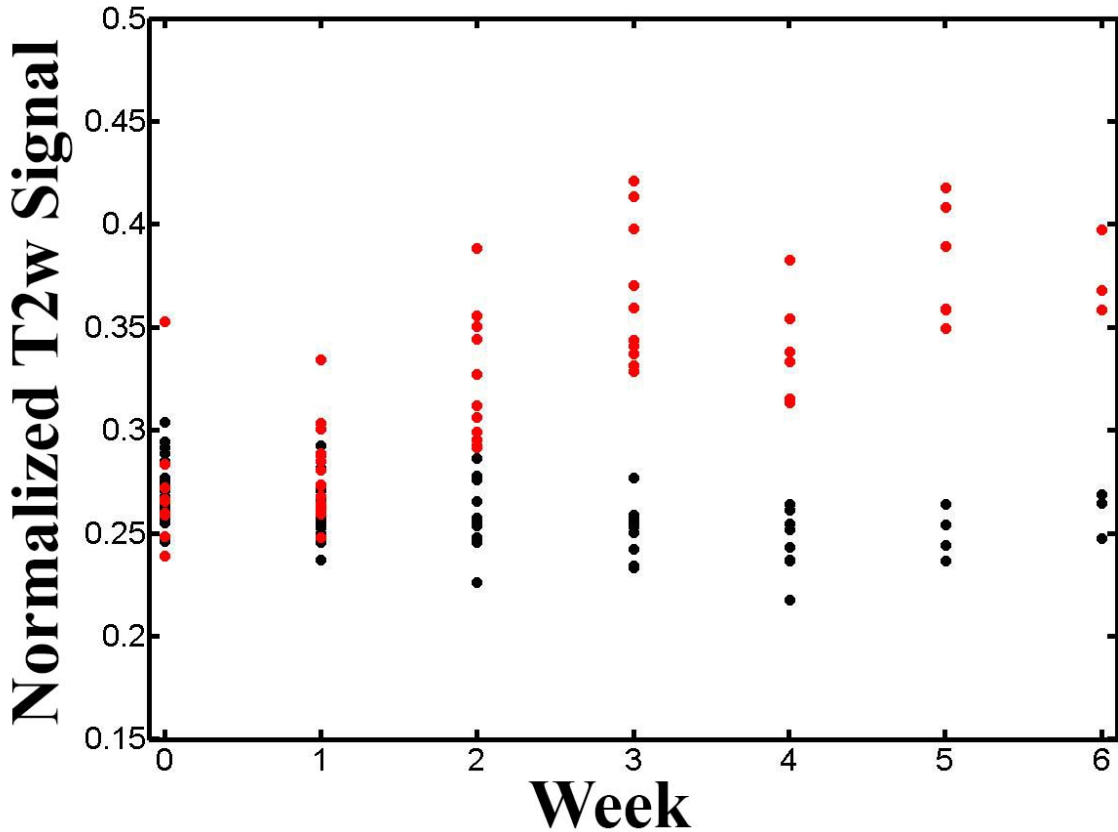


Figure B.1: Individual normalized  $T_2$ -weighted signal intensity mouse measurements in the corpus callosum. Red and black dots represent cuprizone and control measurements, respectively. [Week 0:  $n=16(\text{CTL})/11(\text{CPZ})$ , Week 1:  $n=17(\text{CTL})/18(\text{CPZ})$ , Week 2:  $n=12(\text{CTL})/15(\text{CPZ})$ , Week 3:  $n=11(\text{CTL})/11(\text{CPZ})$ , Week 4:  $n=9(\text{CTL})/9(\text{CPZ})$ , Week 5:  $n=6(\text{CTL})/6(\text{CPZ})$ , Week 6:  $n=3(\text{CTL})/3(\text{CPZ})$ ]. Data from weeks excluded due to high noise.

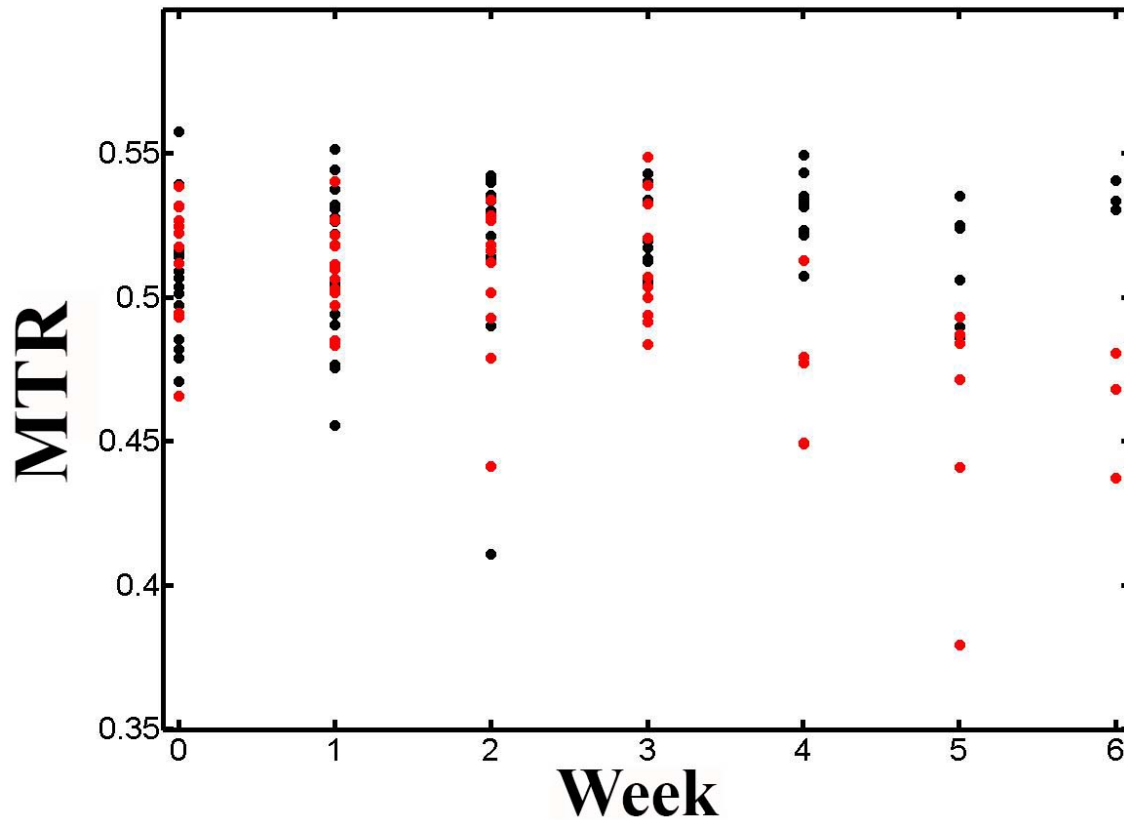


Figure B.2: Individual MTR mouse measurements in the corpus callosum. Red and black dots represent cuprizone and control measurements, respectively. [Week 0: n=16(CTL)/11(CPZ), Week 1: n=17(CTL)/18(CPZ), Week 2: n=12(CTL)/15(CPZ), Week 3: n=11(CTL)/11(CPZ), Week 4: n=9(CTL)/9(CPZ), Week 5: n=6(CTL)/6(CPZ), Week 6: n=3(CTL)/3(CPZ)]. Data from weeks excluded due to high noise.

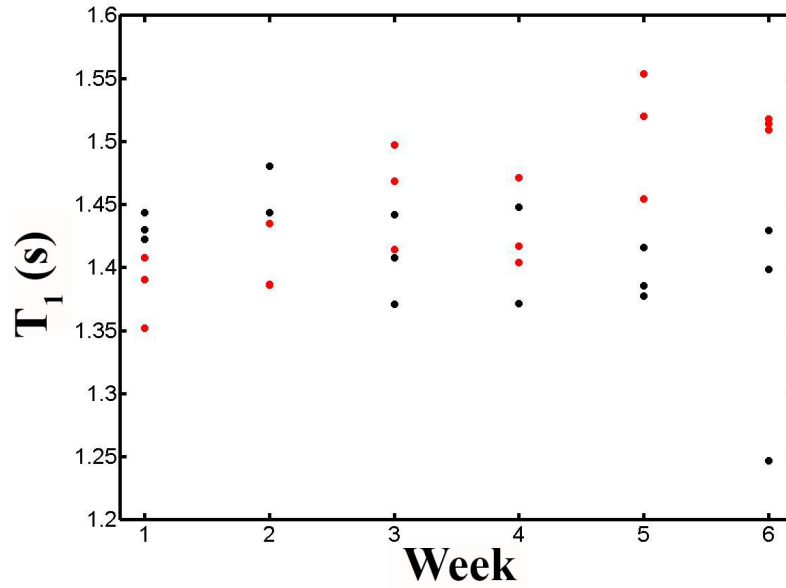


Figure B.3: Individual longitudinal relaxation time,  $T_1$ , mouse measurements in the corpus callosum. Red and black dots represent cuprizone and control measurements, respectively. Each group mean at each week contains  $n=3$  measurements excluding CTL week 4 where  $n=2$  due to suspected cross talk effects.

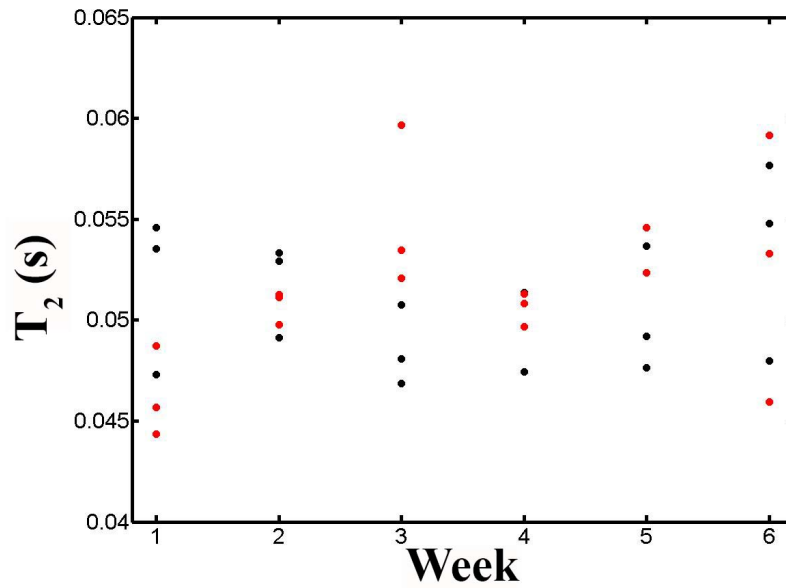


Figure B.4: Individual transverse relaxation time,  $T_2$ , mouse measurements in the corpus callosum. Red and black dots represent cuprizone and control measurements, respectively. Each group mean at each week contains  $n=3$  measurements excluding CTL week 4 where  $n=2$  due to suspected cross talk effects.

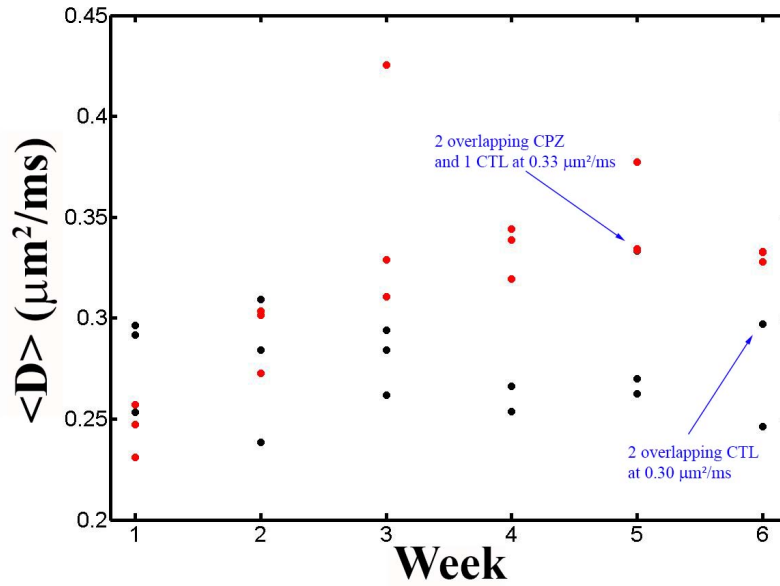


Figure B.5: Individual mean diffusivity,  $\langle D \rangle$ , mouse measurements in the corpus callosum. Red and black dots represent cuprizone and control measurements, respectively. Each group mean at each week contains  $n=3$  measurements excluding CTL week 4 where  $n=2$  due to suspected cross talk effects.

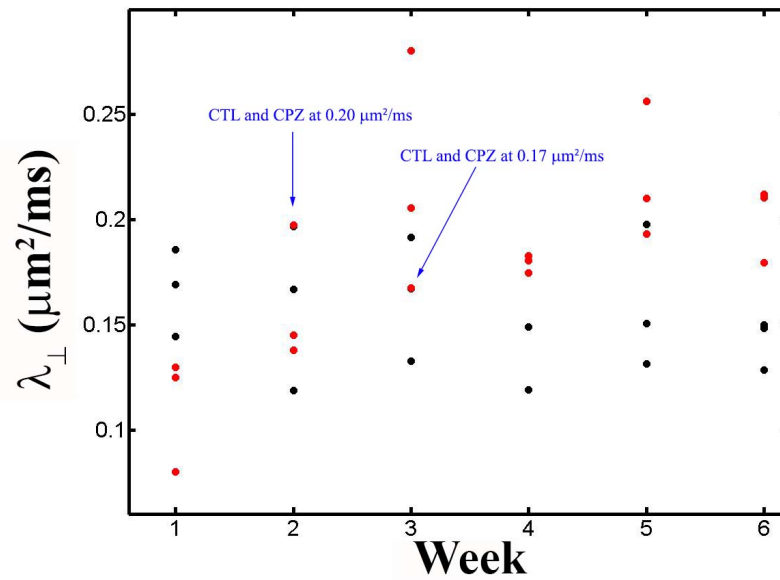


Figure B.6: Individual radial diffusivity,  $\lambda_{\perp}$ , mouse measurements in the corpus callosum. Red and black dots represent cuprizone and control measurements, respectively. Each group mean at each week contains  $n=3$  measurements excluding CTL week 4 where  $n=2$  due to suspected cross talk effects.

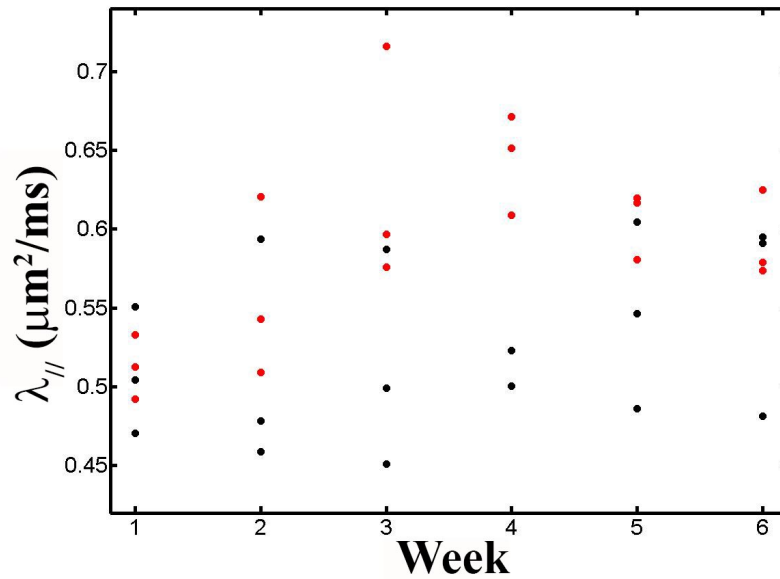


Figure B.7: Individual axial diffusivity,  $\lambda_{\parallel}$ , mouse measurements in the corpus callosum. Red and black dots represent cuprizone and control measurements, respectively. Each group mean at each week contains  $n=3$  measurements excluding CTL week 4 where  $n=2$  due to suspected cross talk effects.

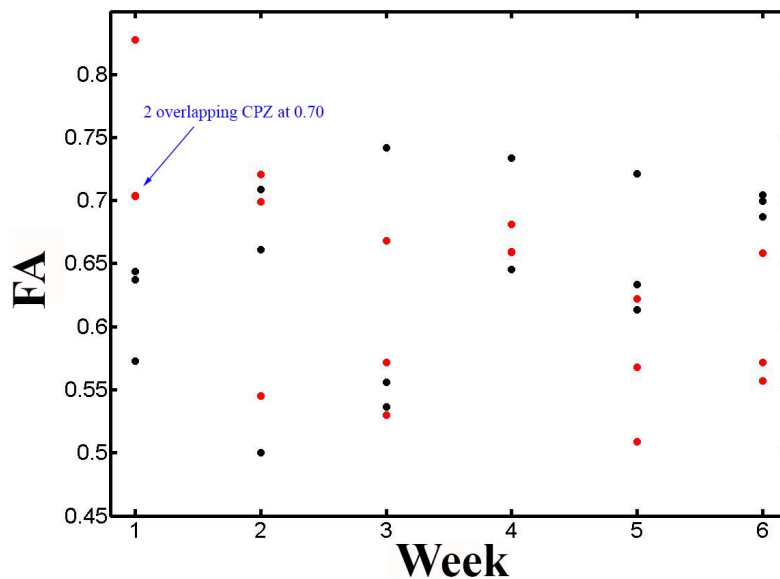


Figure B.8: Individual fractional anisotropy, FA, mouse measurements in the corpus callosum. Red and black dots represent cuprizone and control measurements, respectively. Each group mean at each week contains  $n=3$  measurements excluding CTL week 4 where  $n=2$  due to suspected cross talk effects.

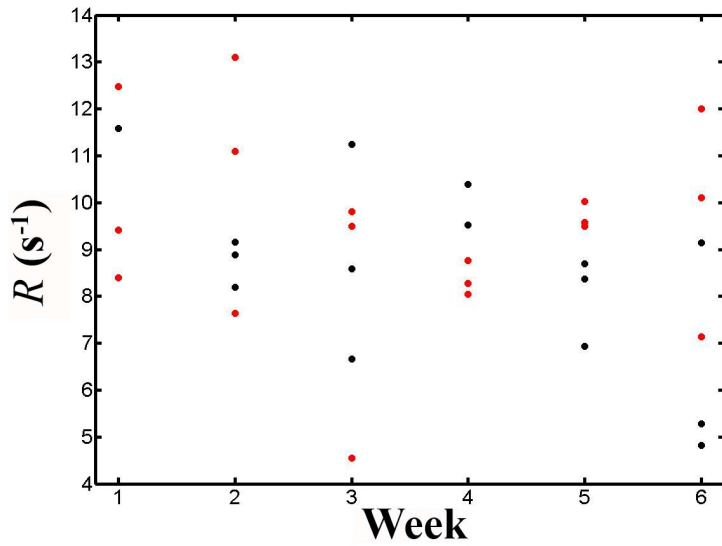


Figure B.9: Individual magnetization transfer rate,  $R$ , mouse measurements in the corpus callosum. Red and black dots represent cuprizone and control measurements, respectively. Each group mean at each week contains  $n=3$  measurements excluding CTL week 1 where  $n=1$  due to contamination of  $k$ -space with high frequency noise in  $M_{sat}$  images that was unable to be removed and CTL week 4 where  $n=2$  for suspected cross talk effects.

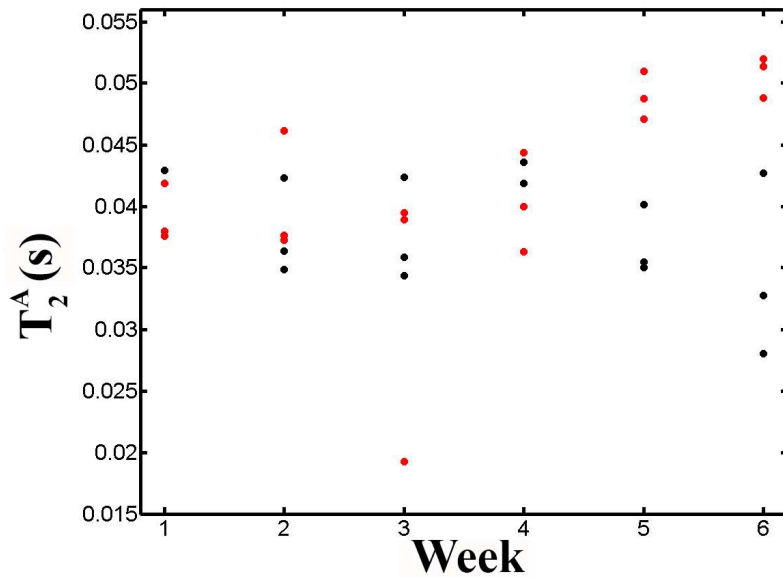


Figure B.10: Individual transverse relaxation times of the liquid pool,  $T_2^A$ , mouse measurements in the corpus callosum. Red and black dots represent cuprizone and control measurements, respectively. Each group mean at each week contains  $n=3$  measurements excluding CTL week 1 where  $n=1$  due to contamination of  $k$ -space with high frequency noise in  $M_{sat}$  images that was unable to be removed and CTL week 4 where  $n=2$  for suspected cross talk effects.

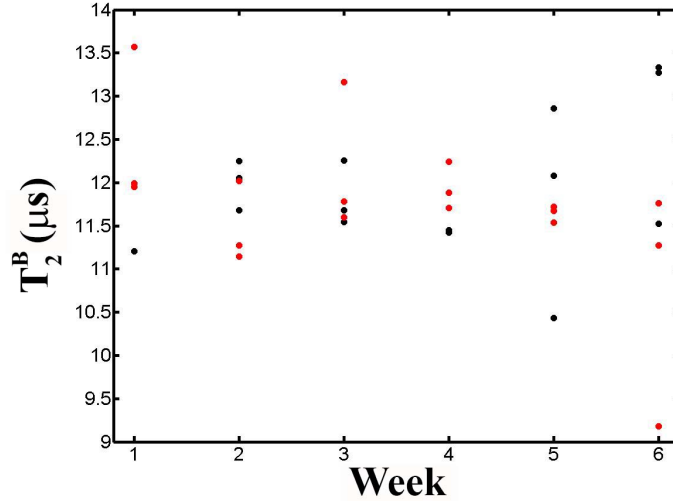


Figure B.11: Individual transverse relaxation times of the bound pool,  $T_2^B$ , mouse measurements in the corpus callosum. Red and black dots represent cuprizone and control measurements, respectively. Each group mean at each week contains  $n=3$  measurements excluding CTL week 1 where  $n=1$  due to contamination of  $k$ -space with high frequency noise in  $M_{sat}$  images that was unable to be removed and CTL week 4 where  $n=2$  for suspected cross talk effects.

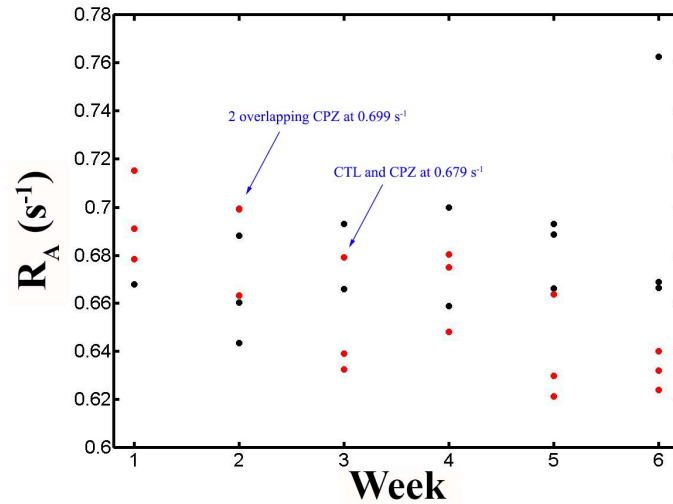


Figure B.12: Individual longitudinal relaxation times of the liquid pool,  $R_A$ , mouse measurements in the corpus callosum. Red and black dots represent cuprizone and control measurements, respectively. Each group mean at each week contains  $n=3$  measurements excluding CTL week 1 where  $n=1$  due to contamination of  $k$ -space with high frequency noise in  $M_{sat}$  images that was unable to be removed and CTL week 4 where  $n=2$  for suspected cross talk effects.

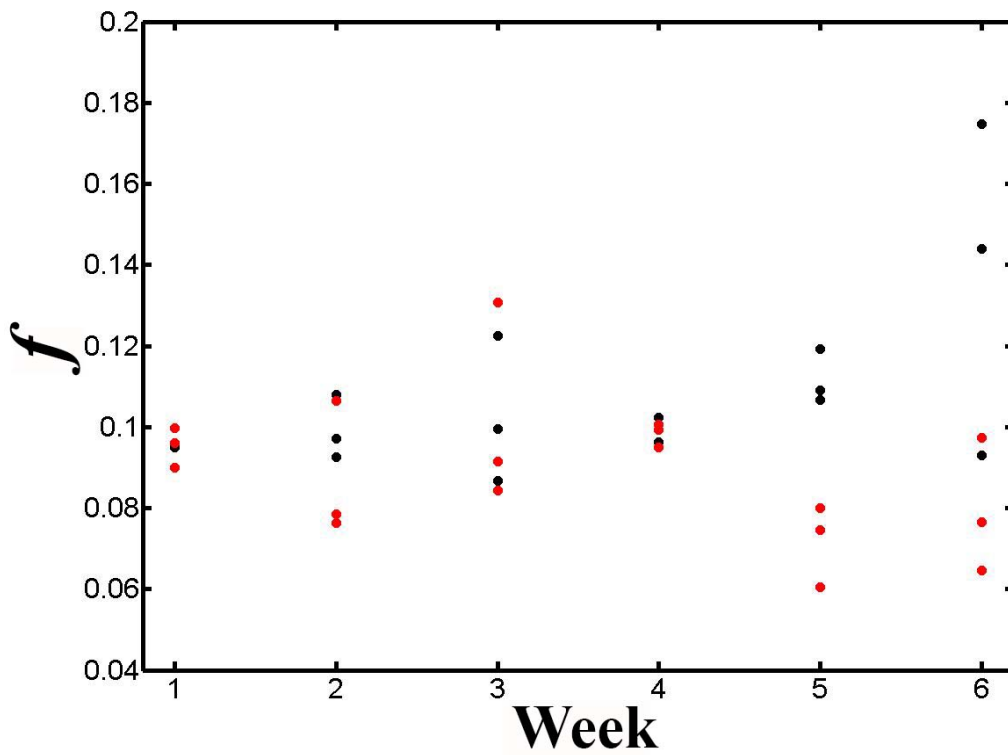


Figure B.13: Individual bound pool fraction,  $f$ , mouse measurements in the corpus callosum. Red and black dots represent cuprizone and control measurements, respectively. Each group mean at each week contains  $n=3$  measurements excluding CTL week 1 where  $n=1$  due to contamination of  $k$ -space with high frequency noise in  $M_{sat}$  images that was unable to be removed and CTL week 4 where  $n=2$  for suspected cross talk effects.

# Bibliography

- [1] M. Neema, J. Stankiewicz, A. Arora, V. S. Dandamudi, C. E. Batt, Z. D. Guss, A. Al-Sabbagh, and R. Bakshi, “T1- and t2-based mri measures of diffuse gray matter and white matter damage in patients with multiple sclerosis,” *Journal of Neuroimaging*, vol. 17, pp. 16S–21S, 2007.
- [2] J. D. Thiessen, *Development and Application of Quantitative MRI Methods for Assessing White Matter Integrity in the Mouse Brain*. PhD thesis, University of Manitoba, 2012.
- [3] V. Gudi, S. Gingele, T. Skripuletz, and M. Stangel, “Glial response during cuprizone-induced de- and remyelination in the cns: lessons learned,” *Frontiers in Cellular Neuroscience*, vol. 9, pp. 1–24, 2014.
- [4] Z.-P. Liang and P. C. Lauterbur, *Principles of Magnetic Resonance Imaging: A Signal Processing Perspective*. Wiley-IEEE Press: New York, 1999.
- [5] J. T. Bushberg, *The Essential Physics of Medical Imaging*. Lippincott, Williams and Wilkins: Philadelphia, 2002.
- [6] D. L. Bihan, “Magnetic resonance diffusion imaging: Introduction and concepts,” in *Diffusion MRI: Theory, Methods, and Applications* (D. Jones, ed.), Oxford University Press, Inc. , New York, 2011.
- [7] H. C. Torrey, “Bloch equation with diffusion terms,” *Physical Review*, vol. 104, no. 3,

pp. 563–565, 1956.

- [8] P. Basser and E. Ozarslan, “Anisotropic diffusion: From the apparent diffusion coefficient to the apparent diffusion tensor,” in *Diffusion MRI: Theory, Methods, and Applications* (D. Jones, ed.), Oxford University Press, Inc. , New York, 2011.
- [9] A. Leemans, “Visualization of diffusion mri data,” in *Diffusion MRI: Theory, Methods, and Applications* (D. Jones, ed.), Oxford University Press, Inc. , New York, 2011.
- [10] M. D. Budde, J. H. Kim, H.-F. Liang, J. H. Russell, A. H. Cross, and S.-K. Song, “Axonal injury detected by in vivo diffusion tensor imaging correlates with neurological disability in a mouse model of multiple sclerosis,” *NMR in Biomedicine*, vol. 21, pp. 589–597, 2008.
- [11] M. D. Budde, M. Xie, A. H. Cross, and S.-K. Song, “Axial diffusivity is the primary correlate of axonal injury in the experimental autoimmune encephalomyelitis spinal cord: A quantitative pixelwise analysis,” *The Journal of Neuroscience*, vol. 29(9), pp. 2805–2813, 2009.
- [12] S.-K. Song, S.-W. Sun, W.-K. Ju, S.-J. Lin, A. H. Cross, and A. H. Neufeld, “Diffusion tensor imaging detects and differentiates axon and myelin degeneration in mouse optic nerve after retinal ischemia,” *NeuroImage*, vol. 20, pp. 1714–1722, 2003.
- [13] M. Xie, J. E. Tobin, M. D. Budde, C.-I. Chen, K. Trinkaus, A. H. Cross, D. P. McDaniel, S.-K. Song, and R. C. Armstrong, “Rostro-caudal analysis of corpus callosum demyelination and axon damage across disease stages refines diffusion tensor imaging correlations with pathological features,” *Journal of Neuropathology and Experimental Neurology*, vol. 69(7), pp. 704–716, 2010.
- [14] S.-K. Song, J. Yoshino, T. Q. Le, S.-J. Lin, S.-W. Sun, A. H. Cross, and R. C. Armstrong, “Demyelination increases radial diffusivity in corpus callosum of mouse brain,” *NeuroImage*, vol. 26, pp. 132–140, 2005.

- [15] J. Zhang, M. V. Jones, M. T. McMahon, S. Mori, and P. A. Calabresi, “In vivo and ex vivo diffusion tensor imaging of cuprizone-induced demyelination in the mouse corpus callosum,” *Magnetic Resonance in Medicine*, vol. 67, pp. 750–759, 2012.
- [16] P. Basser, “Inferring microstructural features and the physiological state of tissues from diffusion-weighted images,” *NMR in Biomedicine*, vol. 8, pp. 333–344, 1995.
- [17] A. L. Alexander, J. E. Lee, M. Lazar, and A. S. Field, “Diffusion tensor imaging of the brain,” *Neurotherapeutics*, vol. 4(3), pp. 316–329, 2007.
- [18] M. A. Brown and R. C. Semelka, “Mr imaging abbreviations , definitions , and descriptions: A review,” *Radiology*, vol. 213, pp. 647–662, 1999.
- [19] J. D. Thiessen, Y. Zhang, H. Zhang, L. Wang, R. Buist, M. R. D. Bigio, J. Kong, X.-M. Lic, and M. Martin, “Quantitative mri and ultrastructural examination of the cuprizone mouse model of demyelination,” *NMR in BioMedicine*, vol. 26, pp. 1562–1581, 2013.
- [20] R. M. Henkelman, G. J. Stanisz, and S. J. Graham, “Magnetization transfer in mri: a review,” *NMR in BioMedicine*, vol. 14, pp. 57–64, 2001.
- [21] G. R. Davies, D. J. Tozer, M. Cercignani, A. Ramani, C. M. Dalton, A. J. Thompson, G. Barker, P. S. Tofts, and D. Miller, “Estimation of the macromolecular proton fraction and bound pool t2 in multiple sclerosis,” *Multiple Sclerosis*, vol. 10, pp. 607–613, 2004.
- [22] J. Henning, A. Nauerth, and H. Friedburg, “Rare imaging: A fast imaging method for clinical mr,” *Magnetic Resonance in Medicine*, vol. 3, pp. 823–833, 1986.
- [23] A. Haase, “Snapshot flash mri. applications to to t1, t2, and chemical-shift imaging,” *Magnetic Resonance in Medicine*, vol. 13, pp. 77–89, 1990.
- [24] E. O. Stejskal and J. E. Tanner, “Spin diffusion measurements: Spin echoes in the presence of a time-dependent field gradient,” *The Journal of Chemical Physics*, vol. 42(1), pp. 288–292, 1965.

- [25] A. Leemans and D. K. Jones, “The b-matrix must be rotated when correcting for subject motion in dti data,” *Magnetic Resonance in Medicine*, vol. 61(6), pp. 1336–1349, 2009.
- [26] G. . Gerig, O. Kubler, and F. A. Jolesz, “Nonlinear anisotropic filtering of mri data,” *IEEE Transactions on Medical Imaging*, vol. 11(2), pp. 221–232, 1992.
- [27] P. Perona and J. Malik, “Scale-space and edge detection using anisotropic diffusion,” *IEEE Transactions on Medical Imaging*, vol. 12(7), pp. 629–639, 1990.
- [28] J. D. Singer, “Using sas proc mixed to fit multilevel models, hierarchical models, and individual growth models,” *Journal of Educational and Behavioral Statistics*, vol. 23(4), pp. 323–355, 1998.
- [29] A. Hesse, M. Wagner, J. Held, W. Brck, G. Salinas-Riester, Z. Hao, A. Waisman, and T. Kuhlmann, “In toxic demyelination oligodendroglial cell death occurs early and is fas independent,” *Neurobiology of Disease*, vol. 37, pp. 362–369, 2010.
- [30] J. L. Mason, A. Toews, J. D. Hostettler, P. Morell, K. Suzuki, J. E. Goldman, and G. K. Matsushima, “Oligodendrocytes and progenitors become progressively depleted within chronically demyelinated lesions,” *American Journal of Pathology*, vol. 164(5), pp. 1673–1682, 2004.
- [31] T. Skripuletz, E. Miller, L. Grote, V. Gudi, R. Pul, E. Voss, J. kuljec, D. Moharreggh-Khiabani, C. Trebst, and M. Stangel, “Lipopolysaccharide delays demyelination and promotes oligodendrocyte precursor proliferation in the central nervous system,” *Brain, Behavior, and Immunity*, vol. 25, pp. 1592–1606, 2011.
- [32] V. Gudia, D. Moharreggh-Khiabania, T. Skripuletz, P. N. Koutsoudakia, A. Kotsiaria, J. Skuljeca, C. Trebsta, and M. Stangela, “Regional differences between grey andwhite matter in cuprizone induced demyelination,” *Brain Research*, vol. 1283, pp. 127–138, 2009.
- [33] A. J. Steelman, J. P. Thompson, and J. Li, “Demyelination and remyelination in

- anatomically distinct regions of the corpus callosum following cuprizone intoxication,” *Neuroscience Research*, vol. 72, pp. 32–42, 2012.
- [34] G. K. Matsushima and P. Morell, “The neurotoxicant, cuprizone, as a model to study demyelination and remyelination in the centralnervous system,” *Brain Pathology*, vol. 11, pp. 107–116, 2001.
- [35] Y. S. M.M. Hiremath and, G. Knapp, J.-Y. Ting, K. Suzuki, and G. Matsushima, “Microglialmacrophage accumulation during cuprizone-induced demyelination in c57bl/6 mice,” *Journal of Neuroimmunology*, vol. 92, pp. 38–49, 1998.
- [36] M. Holz, S. R. Heila, and A. Saccob, “Temperature-dependent self-diffusion coefficients of water and six selected molecular liquids for calibration in accurate 1h nmr pfg measurements,” *Physical Chemistry Chemical Physics*, vol. 2, pp. 470–474, 2000.
- [37] K. Kuroda, T. Iwabuchi, M. Obara, M. Honda, K. Saito, and Y. Imai, “Temperature dependence of relaxation times in proton components of fatty acids,” *Magnetic Resonance in Medicine*, vol. 10(3), pp. 177–183, 2011.
- [38] T. R. Nelson and S. M. Tung, “Temperature dependence of proton relaxation times in vitro,” *Magnetic Resonance in Medicine*, vol. 5, pp. 189–199, 1987.
- [39] P. E. Thelwall, T. M. Shepherd, G. J. Stanisz, and S. J. Blackband, “Effects of temperature and aldehyde fixation on tissue water diffusion properties, studied in an erythrocyte ghost tissue model,” *Magnetic Resonance in Medicine*, vol. 56(2), pp. 282–289, 2006.
- [40] G. J. Stanisz, E. E. Odrobina, J. Pun, M. Escaravage, S. J. Graham, M. J. Bronskill, , and R. M. Henkelman, “T1, t2 relaxation and magnetization transfer in tissue at 3t,” *Magnetic Resonance in Medicine*, vol. 53(3), pp. 507–215, 2005.
- [41] E. Alonso-Ortiz, I. R. Levesque, and G. B. Pike, “Mri-based myelin water imaging: A technical review,” *Magnetic Resonance in Medicine*, vol. 73, pp. 70–81, 2015.

- [42] S. M. Meyers, I. M. Vavasour, B. Madler, T. Harris, E. Fu, D. K. Li, A. L. Traboulsee, A. L. MacKay, and C. Laule, “Multicenter measurements of myelin water fraction and geometric mean  $t_2$ : Intra- and intersite reproducibility,” *Journal of Magnetic Resonance Imaging*, vol. 38, pp. 70–81, 2013.
- [43] C. Laule, P. Kozlowski, E. Leung, D. K. Li, A. L. MacKay, and G. W. Moore, “Myelin water imaging of multiple sclerosis at 7 t: Correlations with histopathology,” *NeuroImage*, vol. 40, pp. 1575–1580, 2008.
- [44] S. Tejedor, V. Gudi, V. Kucman, R. Pul, S. Gingele, K. Suhs, M. Stangel, and T. Skripuletz, “Oligodendroglial markers in the cuprizone model of cns de- and remyelination,” *Histology and Histopathology*, vol. 12, pp. 1455–1464, 2015.
- [45] T. Skripuletz, V. Gudi, D. Hackstette, and M. Stangel, “De- and remyelination in the cns white and grey matter induced by cuprizone: The old, the new, and the unexpected,” *Histology and Histopathology*, vol. 26, pp. 1585–1597, 2011.
- [46] D. Norris, “The effects of microscopic tissue parameters on the diffusion weighted magnetic resonance imaging experiment,” *NMR in Biomedicine*, vol. 14, pp. 77–93, 2001.
- [47] A. Szafer, J. Zhong, and J. Gore, “Theoretical model for water diffusion in tissues,” *Magnetic Resonance in Medicine*, vol. 33(5), pp. 697–712, 1995.
- [48] S.-W. Sun, H.-F. Liang, K. Trinkaus, A. H. Cross, R. C. Armstrong, and S.-K. Song, “Noninvasive detection of cuprizone induced axonal damage and demyelination in the mouse corpus callosum,” *Magnetic Resonance in Medicine*, vol. 55, pp. 302–308, 2006.
- [49] A. N. Dula, D. F. Gochberg, H. L. Valentine, W. M. Valentine, and M. D. Does, “Multiexponential  $t_2$ , magnetization transfer, and quantitative histology in white matter tracts of rat spinal cord,” *Magnetic Resonance in Medicine*, vol. 63, pp. 902–909, 2010.
- [50] K. Schmierer, D. J. Tozer, F. Scaravilli, D. R. Altmann, G. J. Barker, P. S. Tofts, and

- D. H. Miller, "Quantitative magnetization transfer imaging in postmortem multiple sclerosis brain," *Journal of Magnetic Resonance Imaging*, vol. 26(1), pp. 41–51, 2007.
- [51] S. Portnoy and G. J. Stanisz, "Modeling pulsed magnetization transfer," *Magnetic Resonance in Medicine*, vol. 58, pp. 144–155, 2007.
- [52] G. J. Stanisz, S. Webb, C. A. Munro, T. Pun, and R. Midha, "Mr properties of excised neural tissue following experimentally induced inflammation," *Magnetic Resonance in Medicine*, vol. 51, pp. 473–479, 2004.
- [53] M. F. Stidworthy, S. Genoud, U. Suter, N. Mantei, and R. J. M. Franklin, "Quantifying the early stages of remyelination following cuprizone-induced demyelination," *Brain Pathology*, vol. 13, pp. 329–339, 2003.
- [54] M. Kipp, T. Clarner, J. Dang, S. Copray, and C. Beyer, "The cuprizone animal model: new insights into an old story," *Acta Neuropathologica*, vol. 118, pp. 723–736, 2009.
- [55] S.-W. Sun, H.-F. Liang, M. Xie, U. Oyoyo, and A. Lee, "Fixation, not death, reduces sensitivity of dti in detecting optic nerve damage," *NeuroImage*, vol. 44(3), pp. 611–619, 2009.
- [56] S.-W. Sun, H.-F. Liang, T. Le, R. C. Armstrong, A. H. Cross, and S.-K. Song, "Differential sensitivity of in vivo and ex vivo diffusion tensor imaging to evolving optic nerve injury in mice with retinal ischemia," *NeuroImage*, vol. 32(3), pp. 1195–1204, 2006.
- [57] D. Wu, J. Xu, M. T. McMahon, P. C. M. van Zijl, S. Mori, F. J. Northington, and J. Zhang, "In vivo high-resolution diffusion tensor imaging of the mouse brain," *NeuroImage*, vol. 83, pp. 18–26, 2013.
- [58] S. W. Sun, J. J. Neil, and S. K. Song, "Relative indices of water diffusion anisotropy are equivalent in live and formalin-fixed mouse brains," *Magnetic Resonance in Medicine*, vol. 50, pp. 743–748, 2003.

- [59] J. Zhang, “Diffusion tensor imaging of white matter pathology in the mouse brain,” *Imaging in Medicine*, vol. 2(6), pp. 623–632, 2010.
- [60] N. Nathoo, V. W. Yong, and J. F. Dunn, “Understanding disease processes in multiple sclerosis through magnetic resonance imaging studies in animal models,” *NeuroImage: Clinical*, vol. 4, pp. 743–756, 2014.